UNIVERSIDAD DE CHILE
FACULTAD DE CIENCIAS FÍSICAS Y MATEMÁTICAS
DEPARTAMENTO DE ASTRONOMÍA

HYDRODYNAMICAL SIMULATIONS OF DUST TRAPS IN PROTOPLANETARY DISKS

TESIS PARA OPTAR AL GRADO DE
MAGÍSTER EN CIENCIAS, MENCIÓN ASTRONOMÍA

MARCELO FERNANDO BARRAZA ALFARO

PROFESOR GUÍA:
SIMON CASASSUS MONTERO

PROFESOR CO-GUÍA:
SEBASTIÁN PÉREZ MÁRQUEZ

PROFESOR CO-GUÍA 2:
CLÉMENT BARUTEAU

MIEMBROS DE LA COMISIÓN:
CESAR FUENTES GONZÁLEZ
MARIO FLOCK

Este trabajo ha sido parcialmente financiado por Millennium Nucleus "Protoplanetary Disks in ALMA Early Science", Beca CONICYT-PFCHA/Magíster Nacional/2017-22171601, FONDECYT Regular 1171624 y Departamento de Postgrado y Postítulo de la Vicerrectoría de Asuntos Académicos de la Universidad de Chile. Powered@NLHPC: Esta investigación fue parcialmente apoyada por la infraestructura de supercómputo del NLHPC (ECM-02)

SANTIAGO DE CHILE
2018

RESUMEN DE LA MEMORIA PARA OPTAR
AL TÍTULO DE MAGÍSTER EN CIENCIAS, MENCIÓN ASTRONOMÍA
POR: MARCELO FERNANDO BARRAZA ALFARO
FECHA: 2018
PROF. GUÍA: SIMON CASASSUS MONTERO

HYDRODYNAMICAL SIMULATIONS OF DUST TRAPS
IN PROTOPLANETARY DISKS

Resumen

Las teorías actuales de formación planetaria concuerdan que los planetas se forman dentro de discos de gas y polvo alrededor de una estrella jóven. Sin embargo, no es claro cuál es el mecanismo detrás de la formación planetaria. Entre los mecanismos propuestos podemos encontrar que se podrían formar debido al colapso gravitacional, y de un núcleo masivo el cual acreta material. En el escenario de acreción de núcleo el polvo debe crecer varios ordenes de magnitud de manera eficiente. Un lugar en el disco en que el polvo logra concentrarse por un largo tiempo y crecer rápidamente son las llamadas 'trampas de polvo'. De manera interesante, los planetas podrían interactuar con el disco generando cavidades en él, la cual da el paso a la formación de una trampa de polvo debido a un máximo local de presión. Esto abre la posibilidad a la creación de una nueva generación de planetas. En el presente trabajo se estudia el escenario de formación de trampas de polvo debido a interacciones entre el disco y planetas para el disco protoplanetario alrededor de la estrella jóven MWC 758, el cual presenta indicios de la presencia de trampas de polvo.

Nuevas observaciones realizadas con los radiotelescopios ALMA y VLA apoyan la existencia de dos 'trampas de polvo' en MWC 758. Por medio de simulaciones hidrodinámicas en dos dimensiones, las cuales incluyen el gas y polvo del disco, post-procesadas con cálculos de transferencia radiativa, se demuestra que las espirales observadas en luz de scattering y las dos concentraciones de emisión observadas en el rango (sub)milimétrico pueden ser causadas por dos planetas gigantes: un planeta de la masa de Júpiter a $\sim 33\,\mathrm{au}$ (interior a las espirales) y un planeta de 5 masas de Júpiter a $\sim 33\,\mathrm{au}$ de la estrella central (exterior a las espirales). El planeta externo desencadena la formación de varios brazos espirales que logran dar cuenta de algunas de las espirales observadas. Además forma un vórtice al borde interior de la cavidad que genera en la densidad del gas (a $\sim 80\,\mathrm{au}$), cuya emisión en el continuo termal encaja con las observaciones previas de ALMA y VLA, esto si se asume que el polvo está compuesto por granos porosos (con una densidad interna de $\sim 0.1\,\mathrm{g\,cm^{-3}}$) y de tamaños de hasta $1\,\mathrm{cm}$. El planeta interno menos masivo forma un vórtice al borde externo de la cavidad que genera en el gas (a $\sim 47\,\mathrm{au}$), el que decae más rápido que el vórtice inducido por el planeta externo, como resultado de la viscosidad turbulenta del disco. La pérdida de eficiencia en atrapar el polvo de manera azimutal que se produce en el vórtice decayendo puede reproducir la baja señal y mayor extensión observadas en las imágenes VLA de esta trampa de polvo. Para poder confirmar el escenario propuesto en el presente trabajo aún es necesario encontrar de manera directa los posibles planetas, por ejemplo, encontrando su emisión termal o efectos en la cinemática del gas.

Abstract

The current theories for planetary formation concur that planets form embedded in disks of gas and dust around a young star. However, the mechanism behind planet formation is unclear. Between the proposed mechanisms are gravitational instability and core accretion. In the core accretion scenario, the dust must grow efficiently several orders of magnitude. A place where the dust can concentrate for a long time and grow fast are the so-called 'dust-traps'. Interestingly, planets could interact with the disk, carving gaps which leads to the formation of a dust trap due to a local maximum in the pressure of the disk. This opens the possibility for the formation of a new generation of planets. In the present work, we study the scenario of the formation of dust traps via planet-disk interactions for the protoplanetary disk around the young star MWC 758. The system presents two compact concentrations of emission observed in radio wavelengths, previously interpreted as dust traps.

Resolved ALMA and VLA observations support the existence of two dust traps in the spiral-bearing protoplanetary disk around MWC 758. By means of 2D gas+dust hydrodynamical simulations post-processed with 3D radiative transfer calculations, we show that the spirals in scattered light, the asymmetric ring and the crescent-shaped structure in the (sub)mm can be caused by two giant planets: a Jupiter-mass planet at ~ 33 au (inside the spirals) and a 5-Jupiter mass planet at ~ 132 au (outside the spirals). The outer planet triggers several spiral arms that can account for some of the observed spirals. The disk hosts a vortex at the inner edge of its gap (at ~ 80 au), where the compact continuum emission reproduces previous ALMA and VLA observations quite well, if assuming moderately fluffy dust particles (with an internal density $\sim$0.1 g cm^{-3}) up to a cm in size. The inner planet also forms a vortex at the outer edge of its gap (at ~ 47 au) that decays faster than the vortex induced by the outer, more massive planet as a result of the disk's turbulent viscosity. The loss of azimuthal trapping due to the vortex decay can reproduce the low signal and larger spread observed in VLA observations of this dust trap. Finding the thermal and kinematic signatures of both planets could verify the proposed scenario.

A mi madre

Agradecimientos

En primer lugar agradecer a mi profesor guía Simon Casassus por brindarme la oportunidad de realizar esta investigación y por su constante apoyo en el desarrollo de esta. A Sebastián Pérez por sus enseñanzas y motivación, sin duda un ejemplo a seguir. A Clément Baruteau por su confianza, ayuda, conocimientos y herramientas que me entregó, las cuales fueron fundamentales para este proyecto. A los profesores que conforman la comisión por su ayuda, gran disponibilidad y el tiempo invertido. Además agracedecer a cada uno de los profesores y funcionarios del departamento de Astronomía. También quiero agradecer mi familia, en especial a mis padres por su apoyo incondicional. Finalmente, agradecer a mis compañeros, amigas y amigos, los cuales han hecho de estos años un tiempo memorable.

Contents

List of Tables

Chapter 1

Introduction

How our Solar System was born has been a long-standing question in human history. This question becomes even more pressing with the recent discovery of hundreds of 'solar systems' around other stars. The matter has been focused on the search for understanding how planets were born. Scientists have been looking at young stars and their surrounding material using observations at different wavelengths, while working on theories and numerical simulations, with the aim to discover signposts of forming planets that would shed light on their formation process.

Early in the scientific revolution, scientists and philosophers addressed the question of the origins of the Solar System and some of those ideas remain today, for example, that the solar system was born out of a 'circumstellar disk'. The conception of this idea goes back to famous philosophers Immanuel Kant and Pierre-Simon Laplace, who independently realized that all the planets in our solar system rotate around the Sun in approximately the same plane, and in the same direction. Based on these facts, they proposed that all the planets could share the same origin, in a rotating flattened and cold cloud or 'solar nebula', that rotates around the Sun (Kant, 1755; de Laplace, 1796). Introducing this concept, they suggested that planets were a byproduct of the star and 'solar nebula' formation.

These ideas persist and set the ground of the current models of stellar, disk and planet formation. In the last decade, observations of young stars have unveiled disks of gas and dust around them. These disks are expected to survive for millions of years, given enough time for planets to form inside, the so-called 'protoplanetary disks'. The discovery of thousands of extrasolar planets has changed the direction of the field, where theories of planet formation before the 20th century were thought to reproduce the Solar system architecture. Now we know that our Solar System is a single case of a planetary system, which opens the doors of new ways of approaching how planets could form.

Recent multi-wavelength observations have revealed stunning and diverse sub-structures in protoplanetary disks, such as cavities, rings, crescents and spiral arms. Most of the disks that display these incredible asymmetries are so-called transition disks, which are protoplanetary disks with a cavity close to the central star. Moreover, protoplanetary disks can have different structures when observed at different wavelengths. Observations at different wavelengths

trace different regions and compositions of the protoplanetary disk. Thus, multi-wavelength observations allow us to obtain information about the different components of the disk and draw a clearer picture of what is going on in the disk. The difference in the structures observed at different wavelengths has been studied intensively via numerical simulations of protoplanetary disks. In particular, observations in the (sub)millimeter and infrared reveal how the dust evolves into a variety of structures. Differences appear because dust evolves differently in the disk depending on its degree of coupling with the gas. One of several explanations for the sub-structures observed in a protoplanetary disk is the interaction between one or multiple planets and the circumstellar disk. Despite the proto-planets embedded in these disks are elusive to a robust direct detection, a few proto-planet candidates have been reported via direct imaging (e.g. Reggiani et al., 2017; Keppler et al., 2018). This breakthrough opens the possibility for the first confirmation of the planet-disk interaction scenario as the origin of cavities or/and asymmetries in a transition disk. Furthermore, increases the interest in unveiling the links between the planet's properties and the structures of the disk.

This work

In the present work we study the link between asymmetries and planet-disk interactions. This study supports the planetary origin scenario of the structures in the MWC 758 transition disk. It contributes to a better understanding of dust traps produced by planets. We study the dynamical evolution of dust particles in a gaseous protoplanetary disk interacting with planets. Specifically, the process of dust trapping by vortices produced by multiple planets. We reproduce multi-wavelength observations via numerical simulations coupled to radiative transfer calculations, with the aim to test the planet-disk interaction scenario.

We carried out two-dimensional hydrodynamical simulations using the bi-fluid hydrodynamical code Dusty FARGO ADSG (Fast Advection in Rotating Gaseous Object Masset, 2000; Baruteau, 2008), which solves the Navier-Stokes equations for the gas and which models dust as Lagrangian particles. The outputs of the dust distribution obtained with the hydro-simulations are then post-processed with a radiative transfer code to produce synthetic observations of the thermal emission of dust grains. We carried out the computation of the dust temperature and ray-tracing with the radiative transfer code RADMC3D (Dullemond et al., 2015).

The direct comparison between our set of simulations and predictions with the observations of MWC 758 allows for further interpretation of the data. It helps to disclose the physical effects that influence the dynamical evolution of the gas and dust in the disk. Also, it gives information about which factors affect the emergent emission of the dust traps. Moreover, provide constraints for the mass and location of the putative planets. The main results of this work are part of the paper Baruteau and Barraza et al. 2018 (recommended for publication to Monthly Notices of the Royal Astronomical Society) and will feed future observing proposals.

1.1 Protoplanetary disks

Protoplanetary disks are a by-product of the star formation process. The star forms due to gravitational collapse of a massive, dense and cold rotating molecular cloud (see e.g. Woodward, 1978). The newborn stars are thus surrounded by rotating material of the primordial molecular cloud. Due to the conservation of angular momentum, the material is progressively flattened becoming a rotating circumstellar accretion disk, composed of gas and dust. It is in these disks where planets are thought to be born, hence planets can also be considered a byproduct of the star formation process.

The major part of the mass of the protoplanetary disk is in the gas component (hydrogen and helium) typically 10^{-1} to 10^{-3} times the mass of the central star, which corresponds to a pre-main sequence star (T Tauri star). And the dust only represents a small fraction of the total mass (typical dust-to-gas mass ratio is about $10^{-2} - 10^{-3}$). The disk radial extent can reach a few hundreds of au, the vertical extent is much smaller. The thickness of the disk is characterized by the pressure scale height to radius ratio (or disk aspect ratio, H/r) which has typical values in the range of $0.03 - 0.1$. The lifetime of a protoplanetary disk, which is the reference timescale for every process in the disk is approximately between 10^6 and 10^7 years, but the precise number is still under intense debate.

Protoplanetary disks and protostars are classified in classes of Young Stellar Objects (YSOs) based on the slope of its observed spectral energy distribution in the infrared (SED, see Figure 1.1). This classification is interpreted as an evolutionary sequence (Adams and Shu, 1986, see Fig. 1.2). The study of the SED has been crucial to infer the general physical properties of pre-main sequence stars and circumstellar disks. In Figure 1.3 a schematic edge-on view of a protoplanetary disk is displayed. In the upper layers, the disk is directly irradiated, the light from the star is scattered off the surface and reddened into (near)infrared wavelengths. The disk midplane (in dark-brown) emits at (sub)millimeter wavelengths, as is the region where (sub)millimeter-sized dust is settled. Therefore, the planets are expected to form in the midplane. The regions close to the midplane are usually assumed to be locally isothermal (the temperature is constant in time). The classification of YSOs is the following:

1. **Class 0:** The SED peaks in the far infrared with no flux in the near-IR. It represents a protostar completely embedded in a cloud of material.
2. **Class I:** The SED is approximately flat or increases towards the mid-IR. It represents a recently formed gas-rich circumstellar disk.
3. **Class II:** The SED decreases towards the mid-IR. Also known as Classical T Tauri stars. It is believed to be an intermediate stage between a gas-rich young circumstellar disk (or primordial disk) and a gas-poor disk, i.e. when most of the surrounding material has been dissipated. Transition disks are a sub-group of Class II objects, which have a characteristic deficit of infrared excess in its SED (Strom et al., 1989; Skrutskie et al., 1990). The observed dip in the SED reflects a lack hot dust in the disk, which is attributed to the presence of a dust-depleted cavity close to the central star. Such cavities have been observed to be present in several circumstellar disks in the last few years, mainly in the sub-millimeter (e.g. Andrews et al., 2011; Espaillat et al., 2014; van der Marel et al., 2016b; Pinilla et al., 2018),

4. **Class III:** Pre-main-sequence stars with little excess in the IR. It represents gas-poor disks of debris. The circumstellar gas has been dissipated, and the dynamics of the solid bodies is dominated by gravitational interactions only.

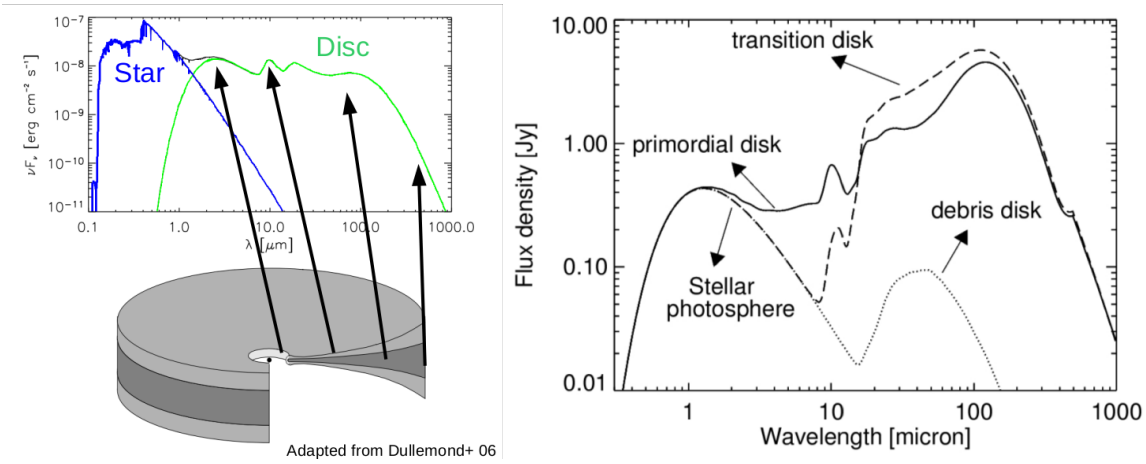

Figure 1.1: **Left:** A schematic image that shows that the different parts of a protoplanetary disk contribute in different sections of the observed spectral energy distribution (SED), image adapted from Dullemond et al. (2007). **Right:** Schematic example of the different disk SED's depending on its classification, image adapted from Pascucci and Tachibana (2010).

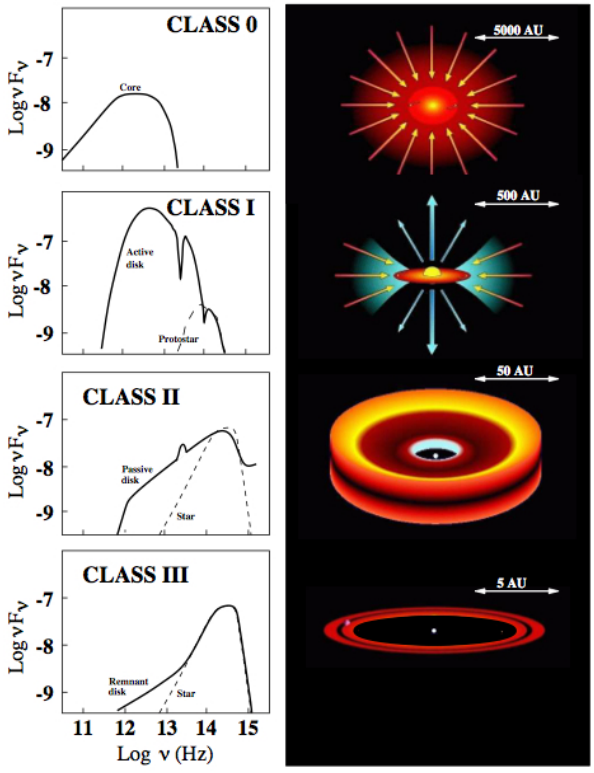

Figure 1.2: A schematic image that shows the classification of Young Stellar objects (YSOs). A characteristic SED of each class is shown on the left-hand side, and an illustration of the corresponding object is at the right. Image adapted from Andrea Isella's thesis (2006).

1.1.1 Protoplanetary disk structure

Several physical processes dictate the structure of a protoplanetary disk. However, they are usually described as axisymmetric, whose physical properties are defined with dependence only on the radius (r) and the vertical coordinate (z). Commonly, disks profiles are parametrized with a power law:

$$\Sigma(r) = \Sigma_c \left(\frac{r}{r_c}\right)^{\gamma} , \tag{1.1}$$

where γ defines how steep the surface density distribution's decreases with radius. The radial density distribution of the disk is set by an equilibrium between the gravity of the central star, the centrifugal force, viscous evolution and the radial pressure gradient.

In a similar way, the z-dependence of the gas density is set by hydrostatic equilibrium. If self-gravity of the disk is neglected, vertically, the disk is in a balance between the vertical component of the stellar gravity and the disk vertical pressure gradient. If the disk is assumed to be vertically isothermal, the pressure follows $P = \rho c_s^2$, with c_s the sound speed and ρ the gas density. Therefore, the equilibrium equation yields,

$$c_s^2 \frac{\mathrm{d}\rho}{\mathrm{d}z} = -\frac{GM_\star z}{(r^2 + z^2)^{3/2}}\rho \,, \tag{1.2}$$

that leads to the solution:

$$\rho = \mathrm{C}exp\left(\frac{GM_\star}{c_s^2(r^2+z^2)^{1/2}}\right) . \tag{1.3}$$

We can define the scale height of the disk $H \equiv c_s/\Omega_k$, with Ω_k the orbital angular frequency, and assume the disk to be thin i.e. $H/r << 1$. This yields the equation that expresses the vertical mass distribution of a thin disk as function of radius:

$$\rho(r,z) = \Sigma(r)\frac{\mathrm{e}xp(-z^2/2H^2)}{\sqrt{2\pi}H} . \tag{1.4}$$

However, the radial structure of the disk is expected to be perturbed by, for example, viscous evolution, accretion, photoevaporation and magneto-hydrodynamic effects. Also the gravitational influence of companions such as planets, substellar objects or flybys.

1.1.2 Transition disks: Asymmetries

Circumstellar disks may present large cavities in their (sub)mm emission (see e.g. Andrews et al., 2011; van der Marel et al., 2016b; Pinilla et al., 2018). The disks that have large cavities of tens of astronomical units (au) are typically classified as transition disks. Protoplanetary disks may also present symmetric features, for example, gaps and rings (e.g. Quanz et al., 2013), and also asymmetries such as crescent-shaped structures in their radio emission (e.g. van der Marel et al., 2013), and spiral arms (e.g. Avenhaus et al., 2017). Disks with large cavities and rings/asymmetries have received special interest, as these structures are often linked to planet-disk interactions. Therefore, these disks have more information about indirect evidence of planets in the disk to constraint their location and masses, that supports a dedicated follow up for direct detection of these companions. This general scenario offers new insights into the relation between the initial stages of the protoplanetary disk, the process of planet formation and its final outcomes. Moreover, new facilities such as the Atacama Large Millimeter/submillimeter Array (ALMA) have been able to resolve the sub-structures in transition disks. In the last decade, sub-mm observations of transition disks revealed horseshoe-like asymmetries in the brightness distribution of several transition disks. A few examples are LkHα 330 (Brown et al., 2008; Isella et al., 2013), HD142527 (Casassus et al., 2013, 2015; Fukagawa et al., 2013), Oph IRS 48 (van der Marel et al., 2013), MWC 758 (Isella et al., 2010; Marino et al., 2015), AB Aurigae (Tang et al., 2012), PDS 70 (Hashimoto et al., 2015), HD 100546 (Wright et al., 2015), SAO 206462 and SR 21 (Pérez et al., 2014). As the emission in the (sub)mm wavelengths is, in some disks, optically thin, the observed asymmetries can be interpreted as a perturbation in the density or/and temperature structure of the disk. But usually, they are interpreted as a reflection of asymmetries in the spatial distribution of (sub)mm-sized dust grains in the disk midplane.

The morphology of the observed asymmetries in the radio wavelengths are in agreement with dust accumulations or 'traps' formed inside a large-scale anticyclonic vortex, predicted via numerical simulations (e.g. Regály et al., 2012). The importance of the study of asymmetries in transition disks and its relation with the 'dust trap' scenario is that it could be inside these structures where dust grains could grow and coagulate with ease from micron to km-sized bodies, thereby allowing the formation of a planetary embryo that could later become a protoplanet (e.g. via core accretion).

1.2 Planet formation

1.2.1 Theories of protoplanet formation

Theories of the formation of planets in a protoplanetary disk can be summarized in the two most relevant scenarios: planetary formation via core accretion and via gravitation instabilities. The main differences are the physical mechanism and the timescale in which they act. Both mechanisms are not exclusive to perform on the same disk but may act on different periods of the disk lifetime.

For planetary formation via 'Gravitation Instability' (GI), a massive and young circumstellar disk is needed, under these conditions self-gravity becomes important. If radiative cooling is efficient, gravity can defeat the pressure support of the disk and disk rotation, leading to the fragmentation of the disk into clumps. It is inside these clumps where a gas giant could form (Boss, 1997), akin to the formation of a proto-star. The stability of the disk is often studied via the so-called Toomre parameter (Q, Toomre, 1964). It sets the critical condition in which the disk becomes gravitationally unstable, which reads:

$$Q \equiv \frac{c_s \kappa}{\pi G \Sigma} \lesssim 1\,, \tag{1.5}$$

where c_s is the sound speed, κ is the epicyclic frequency, and Σ is the disk surface density. The disk becomes unstable when $Q \lesssim 1$, which could happen in young and massive disks. The parts where the disk becomes gravitationally unstable lead to rapid clump formation. This is thought to occur beyond $30 - 50\,\mathrm{au}$ typically (Rafikov, 2005).

The second mechanism of planetary formation is the so-called 'core accretion'. The process of planet formation via core accretion consists in the formation of a solid massive core via accretion of km-sized planetesimals, that later may accrete gas (Pollack et al., 1996), and form a gas giant planet. The final planet mass depends on the critical mass that could trigger runaway accretion of planetesimals into the solid core (typically a few Earth masses), the number of planetesimals in the planet's feeding zone, and mass in gas that can be supplied by the circumplanetary disk. The formation of such massive core needs the dust to grow several orders of magnitudes, from the interstellar medium submicron-sized dust to km-sized planetesimals, which are the foundations of the planet cores. The main problem of the core-accretion scenario is that it is only plausible if the population of planetesimals is large enough, so the growth of the planetary core is sufficiently rapid. However, the fast growth of planetesimals seems to be inefficient. Different mechanisms have been proposed to solve this problem, for example, pebble accretion (Johansen and Lacerda, 2010; Ormel and Klahr, 2010; Lambrechts and Johansen, 2012; Morbidelli and Nesvorny, 2012). By contrast, gravitational instabilities seem not to face a timescale problem for planet formation, as they occur in short timescales compared to the lifetime of the protoplanetary disk.

1.2.2 Dynamics of dust grains: Coupling between gas and dust

As previously mentioned, the observations of a protoplanetary disk are very different depending on the wavelength of the observed radiation. This makes necessary to observe a disk at a wide range of wavelengths to completely understand its structure. Small dust is well coupled to the gas. The emission of these small grains dominates in near-infrared and optical wavelengths. Consequently, the observations of polarized scattered light at near-infrared wavelengths trace the warm small dust particles in the surface of the disk and can be used as a tracer of the gas surface density distribution. Large grains are weakly coupled to the gas, so the spatial distribution of large dust grains is different from that the gas. The photons emitted by thermal emission of dust have a wavelength comparable to the grain's size, if dust is treated as compact spheres. Therefore, large grains are traced by observations at radio wavelengths. Dust of (sub)mm size sediments toward the midplane, thus, it is mostly located in the regions close to the mid-plane of the disk.

The dynamics of dust grains depends on the gravitational forces exerted by the star, the companions and the self-gravity of the disk. Also, it is affected by the aerodynamic drag that is driven by the gas, which is sensitive to the level of turbulence in the gas. A summary of the different mechanisms that affect the dust in a protoplanetary disk is displayed in Fig. 1.3. Let us define the friction time scale for a particle of mass m with the following equation:

$$t_{fric} = \frac{m\, v}{F_D}\,, \tag{1.6}$$

where v denotes the velocity of the dust particle relative to the gas, and F_D represents the drag force exerted by the gas onto the dust particle. The friction time-scale is the time in which drag force will change the particle's velocity v. The drag force F_D depends on the grain size, for the particles that are in the Epstein drag regime (Whipple, 1972; Weidenschilling, 1977), i.e. particles with sizes smaller than the mean free path of the molecules in the gas, and considering that the dust grains have velocities considerably lower than the mean thermal speed (typically of cm size or less), the drag force follows:

$$F_D = -\frac{4\pi}{3}\rho a_s^2 v_{th} v\,, \tag{1.7}$$

where ρ is the gas density, a_s is the radius of the particle, and v_{th} is the mean thermal speed. Assuming that the particle is spherical and has a constant internal density ρ_s, the mass of the dust particle is then $m = (4/3)\pi a_s^3 \rho_s$. The frictional time-scale can then be written in a different form:

$$t_{fric} = \frac{\rho_s}{\rho}\frac{a_s}{v_{th}}\,. \tag{1.8}$$

We can then define a ratio between the friction time-scale and the dynamical timescale, the commonly called Stokes number (St):

$$St = \sqrt{\frac{\pi}{8}} \frac{a_s}{H} \frac{\rho_s}{\rho}\,; \qquad v_{th} = c_s \frac{8}{\pi};\; H = \frac{c_s}{\Omega_k}\,. \tag{1.9}$$

The Stokes number tells us the degree of coupling between the gas and the dust particle. If $St << 1$ the particle is well coupled to the gas and both have about the same spatial distribution in the disk. Nonetheless, if $St \sim 1$ the particles are weakly coupled to the gas, so the gradients of pressure in the disk influence significantly the dynamics of these dust grains, and also the vertical structure of the disk, as particles less coupled will move to the mid-plane (dust settling). It is for these particles that trapping inside a pressure maxima becomes important. The dust grains with large Stokes number ($St >> 1$), however, are decoupled from the gas, and will try to follow Keplerian orbital velocity.

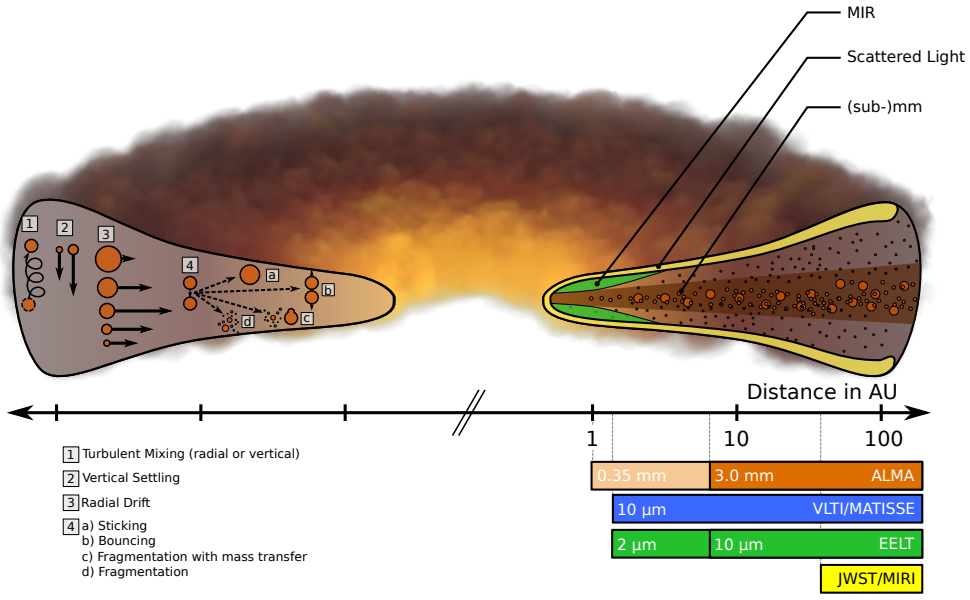

Figure 1.3: Illustration of a protoplanetary disk, with is structure, grain evolution processes and observational constraints from Testi et al. (2014). On the left are listed the main grain evolution mechanisms for its transport (1,2,3) and growth (4). The arrows show the different velocity magnitudes of the grains. On the right, it is illustrated the different areas of the disk that can be traced by the different wavelengths and techniques. The horizontal axis shows the stellocentric distance in logarithmic scale. The horizontal colored bars illustrate the angular resolution that the different instruments achieve for a typical distance of the nearest star-forming regions.

1.2.3 The meter-size barrier problem

The core-accretion scenario for planet formation requires hierarchical growth of solids from micron-sized interstellar dust to km-sized planetary cores, i.e. several orders of magnitude in size. The growth of solid from micron to a meter in size seems not have problems in the theory. The contrary happens in the case of meter-sized boulders to a planetary embryo. Here, aerodynamic drag makes the particle have a slower velocity than the gas where it is embedded, i.e. the particles lose angular momentum. The resulting gas-dust interaction makes the particle move radially to the central star, extremely fast (about a hundred years at 1 au for meter-sized bodies). This effect is usually called radial drift. As a particle grows the aerodynamic drag is stronger, and then its radial drift is faster, producing a 'barrier' for large particles to grow inside the disk without falling onto the central star. This predicts that boulders would fall into the star before larger bodies can form, this problem is known as the 'radial drift barrier' (Whipple, 1972; Weidenschilling, 1977). To overcome the radial drift problem, it is necessary to have a location where the large dust particles have the ideal conditions that allow them to stay at the same radial location for a timescale large enough to form a planetary core. These locations are known as 'dust traps'. The physical conditions in the disk that compose a dust trap and its formation mechanisms have been intensively studied in the last decade.

A second factor that puts difficulties to dust growth is that, if we assume that dust grains grow and coagulate via collisions, the bigger the dust grain, the lower probability for the collision to end up in a larger dust grain, so the large particles are likely to fragment instead of sticking and forming a bigger size solid. This problem is usually called the bouncing-barrier (e.g. Blum and Wurm, 2008). The growth of dust has also been studied via numerical simulations, radial dust traps have been also proposed to be a possible solution for the dust to grow beyond the limits of the bouncing-barrier (e.g. Pinilla et al., 2012).

Both impediments to dust growth described above are at play at the same time. And the range of sizes where they act tells us that it is incredibly difficult for dust grains to grow beyond the meter-size via collisions (see e.g. Brauer et al., 2008). So, both effects together could also be referred to as the meter-size barrier. Given this, we could observe how important it might be to have a region in the disk where the solids could evolve and overcome the different impediments for the dust to grow. In particular, we studied the so-called dust traps, that as previously quoted, may be a good place where the dust grains grow beyond the meter-size.

1.3 Dust traps

As mentioned in the previous section, a proposed solution to the problem of dust grains radially drifting into the central star is known as dust traps. A well-studied dust trap is the product of a local maximum in the pressure of the disk. The particles follow the pressure gradient and get trapped in the pressure maxima, allowing the dust to grow beyond the radial drift barrier that exists if the disk has a smooth radial pressure. A schematic image of how a pressure bump works is shown in Fig. 1.4. In the inner parts of the pressure maximum, the positive pressure gradient speeds up the gas, while in the outer parts the pressure gradient slows down the gas. As a result, the particles feel a tailwind in the inner parts of the pressure maximum, and a headwind in the outer parts. Then, the particles drift toward the pressure maximum.

The solid particles (in a range of sizes) can be efficiently maintained in the radial location where the pressure maximum is located (Pinilla et al., 2012). The effective concentration of particles provides an ideal condition for the growth of solid bodies. The mechanisms of growth inside the dust trap include coagulation between solid particles, gravitational collapse (Youdin and Shu, 2002; Johansen et al., 2007), the streaming instability (Youdin and Goodman, 2005), and rapid planetesimal accretion such as pebble accretion (Johansen and Lacerda, 2010; Ormel and Klahr, 2010; Lambrechts and Johansen, 2012; Morbidelli and Nesvorny, 2012).

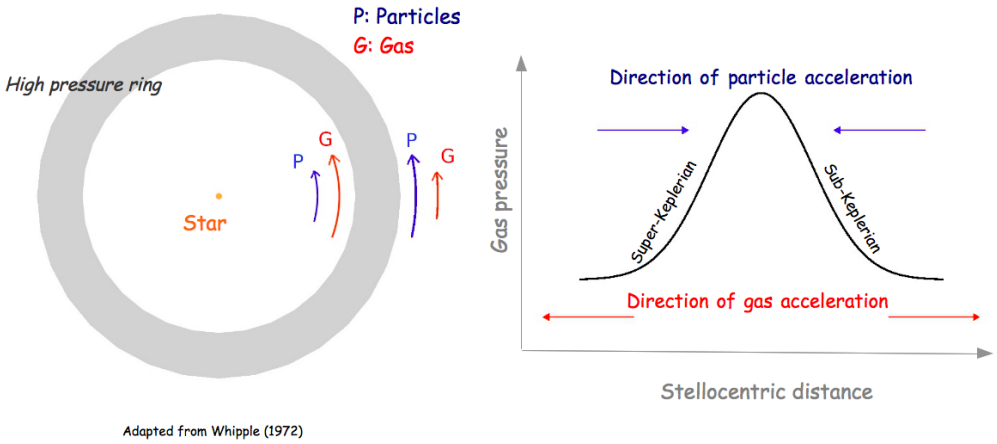

Figure 1.4: Schematic image of a dust trap produced by a pressure bump. **Left:** Face-on schematic image of a ring of high pressure in the disk, the arrows show the relative magnitude of the azimuthal velocity between particles (in blue) and gas (in red). **Right:** Radial cut of the high-pressure ring, the arrows show the radial direction in which the particles (in blue) and gas (in red) move radially through the disk. Image adapted from Wladimir Lyra.

1.3.1 Vortices in protoplanetary disk

There are several proposed formation mechanisms for a large-scale vortex. For example, a vortex can be triggered due to the baroclinic instability (Klahr and Bodenheimer, 2003; Lyra and Klahr, 2011; Raettig et al., 2013; Lyra, 2014), or due to the Rossby wave instability (RWI) (Lovelace et al., 1999; Li et al., 2000, 2001; Lyra et al., 2009b; Meheut et al., 2010, 2012a,b,c, 2013; Richard et al., 2013; Flock et al., 2015). Anticyclonic vortices in protoplanetary disks efficiently trap dust particles (Barge and Sommeria, 1995; Klahr and Henning, 1997). The mm to meter-sized particles move through the vortex following the pressure gradient to the maxima of the pressure field of the disk i.e. the vortex center (Lyra et al., 2009b; Baruteau and Zhu, 2016). Moreover, aerodynamic drag makes the accumulation of dust grains inside the vortex more effective. In the vortex core, the particles may form planetary embryos via the coagulation of clumps of solids. The coalescence of several planetary embryos could grow further via collisions, forming a core massive enough to evolve into a proto-planetary core (e.g. Sándor et al., 2011). Furthermore, the vortex can expedite core formation (Klahr and Bodenheimer, 2006), giving a possible solution to the time-scale problem of oligarchic growth (Thommes et al., 2003).

However, vortex formation can be inhibited due to the disk self-gravity when the disk has a large disk-to-star mass ratio (e.g. Lin and Papaloizou, 2011). Large turbulent viscosity can also shorten the vortex's lifetime (Ataiee et al., 2013; Fu et al., 2014a; Regály et al., 2017). Furthermore, if dust feedback into the gas becomes relevant inside the vortex (local dust-to-gas mass ratio ~ 1), it could destroy the vortex (e.g. Inaba and Barge, 2006; Fu et al., 2014b).

In a dust trap produced by a vortex, aerodynamic drag would act differently depending on the size of the grain (or grain Stokes number). The consequence is a different spatial distribution of dust with different sizes inside the vortex. Larger dust grains will be concentrated at the center of the vortex while small grains will be more spreadly distributed (see e.g. Lyra and Lin, 2013). The implication is that dust continuum emission of a dust trap inside a vortex will depend on the observed wavelength, as this emission traces grains with sizes similar to the wavelength of the observation. Thus, at longer wavelengths, the dust trap emission should be more concentrated than at shorter wavelengths.

The Rossby wave instability

In the present work, we focus our study on anticyclonic vortices generated by the Rossby-Wave Instability, their formation and evolution in the gas, and their influence in dust dynamical evolution. The Rossby-wave instability is analogous to the Kelvin-Helmholtz instability acting in differentially rotating disks. The The saturation of the Rossby-wave instability induces the formation of one or several small vortices at about the same radius, which tend to merge and form a single large-scale anti-cyclonic vortex.

The Rossby-wave instability can set in when there is an extremum in the gas potential vorticity[2], which in practice may occur where there is a radial steep pressure gradient. Such pressure gradients can be formed, for example, at the edges of a gap carved by a planet embedded in the disk (Li et al., 2005; Lyra et al., 2009a; Lin, 2012), at the transition between magnetically active and inactive regions in protoplanetary disks, where a sharp transition in the effective viscosity occurs (Lovelace et al., 1999; Li et al., 2000; Varnière and Tagger, 2006; Regály et al., 2012; Lyra et al., 2015; Faure et al., 2015; Flock et al., 2015), or in the protostellar infall from the disk's former molecular cloud about the centrifugal radius (Bae et al., 2015).

Chapter 2

The case of the MWC 758 protoplanetary disk

2.1 Observational background

Recent high angular resolution observations have revealed stunning non-axisymmetric emission features in the transition disk around the Herbig Ae/Be star MWC 758. These asymmetries consist of multiple spiral arms and arcs in near-infrared observations (Grady et al., 2013; Benisty et al., 2015; Reggiani et al., 2017; Ren et al., 2018), an assymmetric ring of emission at $\sim 0''.3$ as well as a compact crescent-shaped stucture at $\sim 0''.52$ in the (sub)mm emission (Marino et al., 2015; Boehler et al., 2017; Casassus et al., 2018; Dong et al., 2018). The asymmetries in the (sub)mm emission, which we will refer to as Clump 1 (outer crescent at $\approx 0''.52$) and Clump 2 (inner asymmetric ring at $\approx 0''.30$) following the terminology used in Casassus et al. (2018), have been interpreted as dust traps at local pressure maxima arising from two large-scale anticyclonic vortices (Marino et al., 2015). The recent cm-wavelength VLA observations of Casassus et al. (2018) support the dust trapping scenario for Clump 1, and suggest marginal trapping for Clump 2. Still, the mechanism behind the formation of the possible dust-trapping vortices in the MWC 758 disk remains elusive and is the subject of this work.

This work is organized as the following. In Section 2.1 of the present chapter we introduce the current observations and its proposed explanations of the MWC 758 disk. In Chapter 3 we describe the physical model and numerical setup of the hydrodynamical simulations, and the radiative transfer calculations are depicted in Chapter 4. Their results are then presented in Chapter 5. Discussion of the results and its implication follow in Chapter 6. Finally, a summary of the results is given in Chapter 7.

2.1.1 The MWC 758 star

Our study is focused on the structures around the MWC 758 star. MWC 758 is classified as a Hebig Ae star (A5) with an age of 3.5 ± 2 Myr (Meeus et al., 2012). The distance at which the star is located has recently been updated from 270^{+94}_{-57} pc as measured with HIPPARCOS (van Leeuwen, 2007) to 160 ± 2 pc (Gaia Collaboration et al., 2018a, Data Release 2). However, in the course of this work, we assumed the Gaia Data Release 1 reported distance of 151 ± 9 pc (Gaia Collaboration et al., 2016, difference of about 6% from the recent DR2 distance). Given the distance and location, we could tell that MWC 758 is close to the edge of the Taurus star-forming region. The results presented could be re-scaled to the new distance and its implications are addressed in Section 5. The MWC 758 star is surrounded by an accretion disk. The circumstellar disk around MWC 758 is one of the most observed in the last decade, whose complex morphology shows intriguing asymmetries and a cavity of tens of au, features that have been intensely studied in the last years. Resolved CO observations of the disk determined a stellar mass of $\sim 1.5 \pm 0.2 M_{\odot}$ (scaled for the assumed Gaia DR1 distance), and obtained an inclination of ~ 21 deg and a position angle of the semi-major axis[1] of 62 deg (Isella et al., 2010; Boehler et al., 2017).

Despite the disk displaying a large cavity observed in the mm wavelength ($\sim$ 55 au), MWC 578's SED is classified as pre-transitional (Grady et al., 2013). The disks classified as pre-transitional show a depleted cavity in (sub)mm wavelengths but no evidence of a cavity in the NIR observations (Grady et al., 2013; Benisty et al., 2015; Reggiani et al., 2017).

Table 2.1: Main parameters of the MWC 758 star.

Parameter	Value	Reference [2]
RA (J2000)	$05^h\ 30^m\ 27.528^s$	(5)
DEC (J2000)	$+25^\circ\ 19'\ 57.082''$	(5)
Age	3.7 ± 2.0 Myr	(2)
Stellar Mass	$1.5 \pm 0.2 M_{\odot}$	(3)
Distance	151^{+8}_{-9} pc	(4)
Disk inclination	21°	(3)
Disk PA	62°	(3)

[1] Angle east of north i,e towards the left.

[2] (1) van Leeuwen 2007; (2) Meeus et al. 2012; (3) Isella et al. 2010; Boehler et al. 2017; (4) Gaia Collaboration et al. 2016; (5) Gaia Collaboration 2018

2.1.2 Infrared observations

Near-infrared observations have revealed multiple large-scale spiral arms in the MWC 758 disk (Grady et al., 2013; Benisty et al., 2015; Reggiani et al., 2017; Ren et al., 2018). In particular, Y-band ($\lambda = 1.04\,\mu$m) polarized scattered light observations obtained with VLT/SPHERE show two symmetric spiral arms ($m = 2$) at the Nort-West (S1) and South-West (S2) parts of the disk (Benisty et al., 2015). These two spirals are in agreement with the previous HiCIAO H-band ($\lambda = 1.6\,\mu$m) image of Grady et al. (2013). No fully depleted cavity was detected down to the inner working angle $\sim 0\farcs1$, while distinct non-asymmetric features were observed near this location. More recently, L-band ($\lambda = 3.8\,\mu$m) high-contrast data was obtained with the NIRC2 instrument at the Keck II telescope. The observations have recovered the S1 and S2 spiral arms and a less bright third spiral arm at the South-West part of the disk (S3) was observed (Reggiani et al., 2017). In addition, the North-West part of the disk has two features about the location of S1 (S1r and S1b). The pitch angle suggests that S1r is more likely an arc, while S1b a section of a spiral. The location and label of each spiral arm are shown in Fig. 2.1. Also, a bright point-like of emission is seen at the south of the star ($r \sim 0\farcs1$).

Among the possible origins for the spiral arms, Gravitational Instability (GI) has been discarded due the relatively low mass of the MWC 758 disk obtained both via gas and dust thermal emission (Isella et al., 2010; Boehler et al., 2017). Another proposed option for the origin of such symmetric spiral arms is shadowing effects by an inner warped disk (Montesinos et al., 2016; Montesinos and Cuello, 2018). Such inner disk has been reported in MWC 758 near-infrared observations (Isella et al., 2013), and as a non-resolved source of continuum emission in radio (Boehler et al., 2017; Dong et al., 2018). A warped nature of the inner disk in the gas has also been observed as a twist of the iso-velocity curves close to the star (Boehler et al., 2017). However, no strong shadowing effects are observed in NIR observations, making this scenario unlikely for the origin of the spirals.

The most supported scenario, including the present work, is that the multiple spiral arms are triggered by planets. The structure and high contrast of the spiral arms have been qualitatively reproduced using global hydrodynamical simulations of one massive planet exciting non-linear spiral waves inside its orbit (Dong et al., 2015; Zhu et al., 2015). The large pitch angle of the spirals and its symmetry suggest that the planet that would trigger the spiral arms should be fairly massive. For example, the presence of a ~ 4.5 Jupiter-mass planet at $\approx 0\farcs66$ from the star, which excites strong shock waves inside its orbit (Dong et al., 2018, see Figure 2.2). Moreover, the third spiral arm observed in L-band could also be produced by the planet outside the spiral (responsible for the two most prominent spirals) if constructive interference is playing a role in the formation of the spiral density waves (Bae and Zhu, 2017) or by an (unseen) planet inner to S3 (see Chapter 6). Finally, an examination of the rotation of the spiral arms was done using a combination of data from Hubble Space Telescope (HST)/NICMOS, Keck/NICR2 L-band observations and VLT/SPHERE data, which found a pattern speed of $\sim 0.6\mathrm{deg/yr}^{-1}$ for the two major spiral arms. Also, they derive that the best location for a planet triggering spirals with such pattern speed is ~ 90 au. This location for the planet is consistent with the results of planet-driven spiral arms of Dong (2015a); Bae and Zhu (2017); Dong et al. (2018), previously applied to the MWC 758 disk.

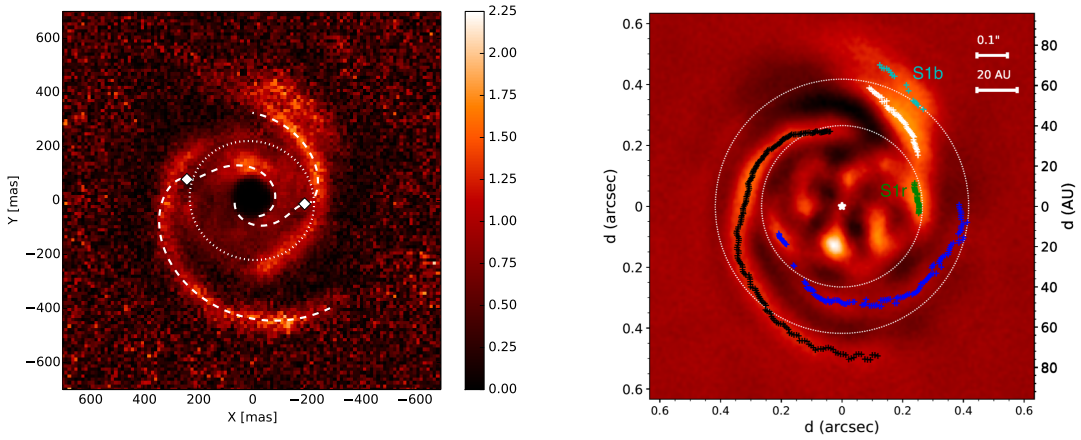

Figure 2.1: Near-infrared observations of the MWC 758 disk. **Left:** Deprojected polarized intensity image (Q_ϕ) from Benisty et al. (2015, 2015 data set). **Right:** Deprojected image of the L-band observations of (Reggiani et al., 2017, 2015 data set). Overlaid are the spiral arm traces of S1 (white), S2 (black) and S3 (blue), and two distinct features close to S1, labeled S1r (green) and S1b (cyan). The dotted lines denote circles at 40 and 63 au (for an assumed distance to MWC 758 of 151 au). East is toward the left and North is up. The color scales in the panels are arbitrary.

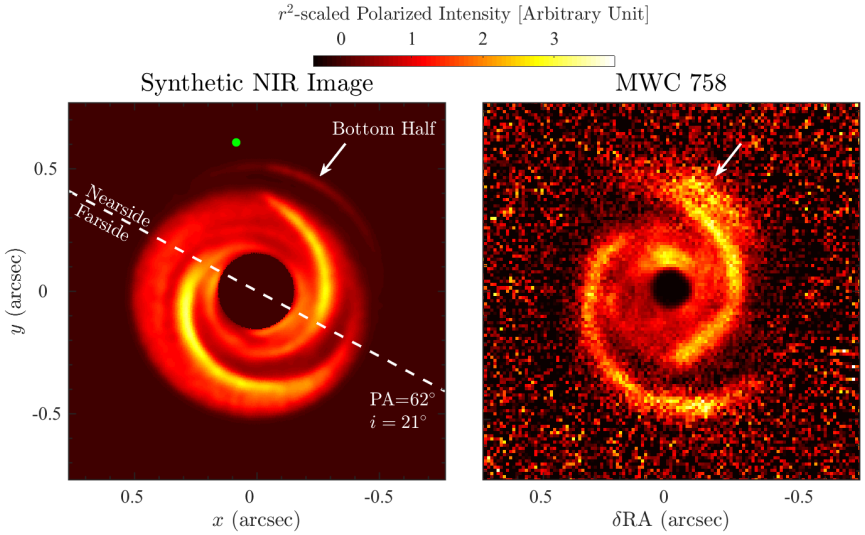

Figure 2.2: Comparison between synthetic NIR image result of planet-driven spiral arms from 3D simulation and scattered light observations presented in Dong et al. (2018). **Left:** A simulated NIR polarized light image of a disk perturbed by a planet. **Right:** The Y-band polarized light image of MWC 758 (Benisty et al., 2015). The simulation is based on the model previously presented in Dong et al. (2015), in which the planet has $M_{\rm planet} = 6 \times 10^{-3}\,M_\star$ and is located at 100 AU. The green dot marks the projected location of the planet.

2.1.3 Radio observations

The high-resolution achieved by the radio telescopes Atacama Large Millimeter Array (ALMA) and Very Large Array (VLA) has been able to resolve the sub-structures of MWC 758 (sub)mm disk. A large inner cavity with a radial width of tens of au (~ 55 au) observed by Isella et al. (2010) has been intensively studied from infrared to radio wavelengths (Andrews et al., 2011; Marino et al., 2015; Boehler et al., 2017; Dong et al., 2018; Casassus et al., 2018). The cavity has been found to be eccentric (e ~ 0.1 Dong et al., 2018). Current explanations for the origin of the cavity are photoevaporation and planet-disk interactions. Photoevaporation has been discarded as it predicts completely cleared inner cavities (Isella et al., 2010; Alexander and Armitage, 2007), while extended emission is present inside the MWC 758 cavity (Boehler et al., 2017). The presence of a planet(s) inside the cavity clearing is orbit is currently the most accepted explanation. Furthermore, the non-zero eccentricity of the cavity is expected if it is produced by one or several planets for both eccentric and circular orbits (e.g. Kley and Dirksen, 2006; Dunhill et al., 2013).

Radio observations have shown two compact concentrations both in (sub)millimeter (ALMA) and cm-wavelength (VLA) (Marino et al., 2015; Boehler et al., 2017; Casassus et al., 2018; Dong et al., 2018). The two asymmetries have been well reproduced via parametric modeling (Marino et al., 2015), with a model with two vortices that follows an extended version of the steady-state vortex prescription described in Lyra and Lin (2013), with a realistic dust's size distribution. In particular, the greater compactness of the clumps of emission at VLA wavelength than at ALMA wavelength (see Fig. 2.3). The radial location of the compact concentrations is about $0\farcs3$ and $0\farcs53$ from the central star (Clump 1 and Clump 2, respectively). More recent (sub)millimeter observations have recovered both clumps and resolved two rings of emission that underlie the clumps, at $\sim 0\farcs32$ and $0\farcs54$ for Clump 1 and 2, plus a third less bright ring in between ($\sim 0\farcs43$, Boehler et al., 2017; Dong et al., 2018). The rings have the same eccentricity as the inner cavity (e ~ 0.1 Dong et al., 2018). The three rings are absent from VLA observations of Casassus et al. (2018) which also show an incredible compactness for Clump 1. Nevertheless, Clump 2 brightness is low relative to Clump 1, and shows a large azimuthal spread for a typical dust concentration produced by a vortex. Suggesting that the trapping of cm-sized grains could be less efficient as for mm-size dust. The morphology of Clump 1 observed in the cm-wavelength images of (Casassus et al., 2018) has also been reproduced using extended Lyra-Lin prescriptions, however, requires an extension if the vortex sonic radius due to the large vortex's aspect ratio ($\chi \sim 16$ Casassus et al., 2018).

The dust continuum ALMA observations of the MWC 758 disk only recovered the south-east spiral arm (S2), while no clear evidence of S2 and S3 spiral arms are obtained (Dong et al., 2018). The gas observations, on the other side, disclose the two most prominent spiral arms in the maps of ^{13}CO and ^{18}CO $= 3 - 2$ peak of emission. The emission of the spiral arms at radio wavelengths still missing an explanation for its origin, as could be as a result of to optical depth effects due to density enhancements, or be related to a higher temperature in the spiral locations, consistent with heating due to the shocks propagating in the disk.

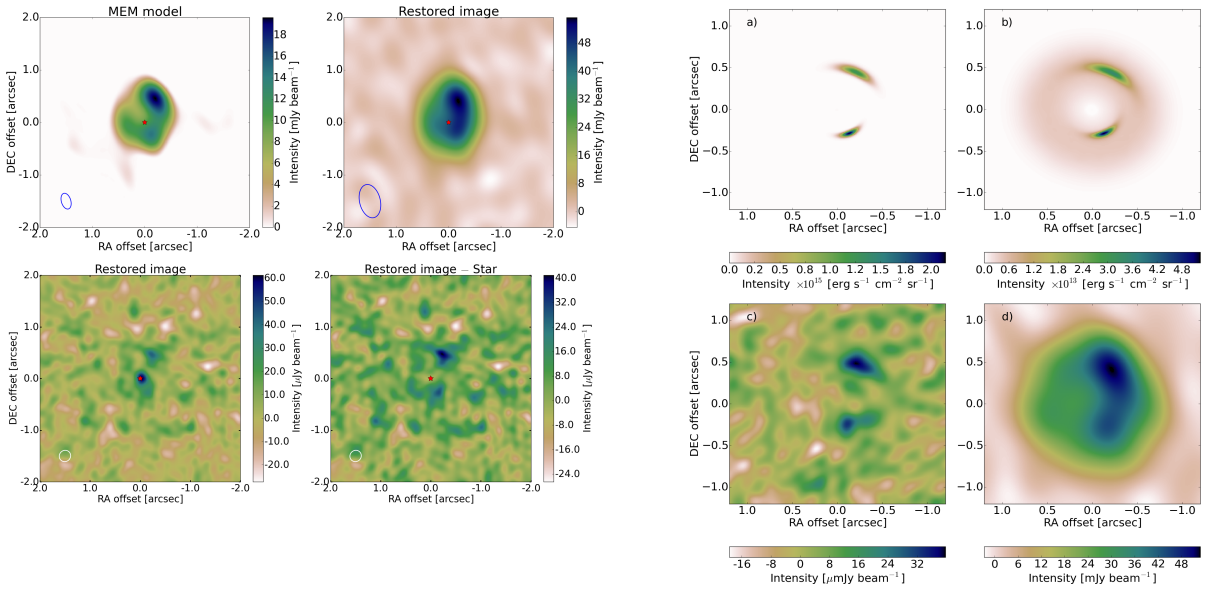

Figure 2.3: Comparison between ALMA and VLA observations of MWC 758, and a parametric model with 2 vortices presented in Marino et al. (2015). **Left panel:** *Upper row:* ALMA observation maps at 337 GHz (Band 7) using MEM non-parametric model (left) and CASA Clean (right). *Lower row:* VLA Ka ($\sim$ 33 GHz) observation images, with the emission at the star location removed in the right image. **Right panel:** *Upper row:* Raw synthetic predictions for a parametric model with two vortices at 33 GHz (left) and 337 GHz (right). *Lower row:* Simulated observations using the model images for VLA Ka (left) and ALMA B7 (right). The axes indicate the offset from the stellar position in R.A and decl. in arcsec. North is up and west is to the right.

2.2 Motivation of the work carried out in the present MSc thesis

As reviewed in Section 1.3.1, one way to form a large-scale vortex in a protoplanetary disk is through the Rossby wave instability at the edges of the gap that a massive planet carves in its disk (e.g. Lyra et al., 2009a; Lin, 2012). More often, it is the gap's outer edge that develops a pressure maximum, but a very massive planet of typically a few Jupiter masses may also form and maintain a pressure maximum at the inner edge of its gap (Bae et al., 2016). Since an anticyclonic vortex is a local pressure maximum, gas drag causes dust particles to concentrate near the vortex's center (e.g. Barge and Sommeria, 1995; Zhu et al., 2014; Ruge et al., 2016, see Section 1.3.1), while the vortex's self-gravity causes dust particles to describe horseshoe U-turns relative to the vortex's center, much like in the circular restricted three-body problem (Baruteau and Zhu, 2016). The competition between gas drag and the vortex's self-gravity leads to size-dependent trapping azimuths for the dust particles located about the vortex's orbital radius (Baruteau and Zhu, 2016). Vortices triggered by the RWI could play a key role in planet formation by slowing down or stalling the dust's inward drift due to gas drag, while allowing dust to grow to planetesimal sizes or even planetary sizes (Lyra et al., 2009a;

Sándor et al., 2011). This could represent the first stage of the formation of a protoplanet via the core-accretion scenario.

A planetary origin for the two possible vortices in the MWC 758 disk is appealing as it could also account for the submillimetre cavity (Isella et al., 2010; Andrews et al., 2011) and the multiple spirals in near-infrared scattered light (Benisty et al., 2015). The presence of protoplanets in MWC 758 is also consistent with the detection of a point-like source inside the submillimetre cavity, which has been detected via high-contrast imaging (Reggiani et al., 2017). Moreover, the structure and high contrast of the spiral arms have been qualitatively reproduced using global hydrodynamical simulations of one massive planet exciting strong shock waves inside its orbit (Dong et al., 2015; Zhu et al., 2015). The morphology of the grand-design spiral arms of MWC 758 suggests that the planet that would trigger the spiral arms should be fairly massive (Dong et al., 2015; Zhu et al., 2015). Such a planet could, therefore, form a persistent pressure maximum at the inner edge of its gap, where the RWI could sustain a large-scale vortex (Bae et al., 2016).

This work aims at bringing further theoretical support for the scenario where the asymmetric structures in the (sub)mm and the spirals in near-infrared could be due to the presence of two massive planets in the MWC 758 disk. For this purpose, we have carried out two-dimensional (2D) gas+dust hydrodynamical simulations of the protoplanetary disk around MWC 758, and used radiative transfer calculations to compare synthetic maps of the continuum and scattered light emission with observations. We present the results of our best match simulations, which correspond to a configuration with a Jupiter-mass planet at ~ 33 au ($0\farcs22$ if the disk is located at 151 parsecs) and a 5 Jupiter-mass planet at ~ 132 au ($0\farcs88$). The outer more massive planet triggers several spiral arms that can account for some of the spirals seen in the scattered light. It also forms a vortex at the inner edge of its gap (at $\sim$ 80 au), where the dust concentration produces a lopsided ring of continuum emission that matches quite well previous ALMA and VLA observations of Clump 1 if assuming moderately fluffy (or porous) dust particles (with an internal density ~ 0.1 g cm^{-3}) up to a centimeter in size. The inner planet trigger one spiral outside its radial location and forms a vortex at the outer edge of its gap (at $\sim$ 47 au) that decays faster than the one induced by the outer planet. A decaying vortex is the only way we can reconcile previous ALMA and VLA observations, in particular, the low signal obtained with the VLA for Clump 2 relative to Clump 1. This scenario of a decaying vortex has been recently proposed by Fuente et al. (2017) to explain multi-wavelength NOEMA observations of the lopsided emission ring in the AB Aurigae transition disk.

Chapter 3

Hydrodynamical Simulations

We carried out 2D gas + dust hydrodynamical simulations using the numerical code Dusty FARGO-ADSG, an extended version of the code FARGO-ADSG (Masset, 2000; Baruteau and Masset, 2008a,b; Baruteau, 2008). The code solves the fluid Navier-Stokes and continuity equations for the gas including a distribution of Lagrangian test particles as the dust component (Baruteau and Zhu, 2016; Fuente et al., 2017). Here we describe our simulation setup specific to MWC 758.

3.1 Gas setup

We have assumed a locally isothermal equation of state:

$$P = \Sigma c_s^2 \,;\; c_s^2 = \frac{k_b T}{\mu m_H} \,;\; \mu = 2.4 \,, \tag{3.1}$$

where the quantities are P the local pressure, Σ the local surface density, c_s the sound speed, T the local temperature, and k_b and μ represents the Boltzmann constant and the mean molecular weight. The temperature remains fixed in time through the simulations. Based on previous radiative transfer calculations of the thermal emission in the MWC 758 disk (see Figure 9 in Boehler et al., 2017), we take the midplane temperature to decrease as r^{-1} and equal to 90 K at 33 au (r denotes the radial cylindrical coordinate measured from the central star). The disk's aspect ratio, which is the ratio of the midplane isothermal sound speed to the Keplerian velocity (i.e. $h = c_s/\Omega_k$), is therefore uniform and equal to 0.088. The gas surface density of the disk gas Σ is initially assumed to proportional to r^{-1}, axisymmetric and equal to $\sim 2\,\mathrm{g\,cm^{-2}}$ at 30 au, specifically:

$$\Sigma(r) = \Sigma_0 \left(\frac{r}{r_0}\right)^{-1} \;; \quad \Sigma_0 = 1.6 \times 10^{-4} \frac{M_\star}{r_0^2} \,, \tag{3.2}$$

where Σ_0 is the surface density at r_0, which denotes the code unit of length. We set r_0 to be

equal to the inner planet's orbital radius (33 au). $M_\star$ is the mass of the central star, which we take as a $1.5\,M_\odot$ star (Reggiani et al., 2017).

In a quasi-steady state, when the planets have carved a gap about their orbit, the azimuthally averaged gas surface density varies from 1 to $2\,\mathrm{g\,cm^{-2}}$ between 40 and 90 au, which is consistent with the analysis carried out by Boehler et al. (2017, see their figure 8). The Toomre Q-parameter, presented in Section 1.2, gives the critical condition that, if reached, the disk becomes unstable to the growth of surface density perturbations ($Q \lesssim 1$). The value of this parameter is important in our work as we are including the effects of the gravitational force between different fluid elements in the disk (gas disk's self-gravity). In our simulations, the value of the Q-parameter is rather large (it is ≈ 30 at 80 au, the radial location of Clump 1), so the disk is gravitationally stable. Despite the large value of Q in our simulations, gas self-gravity is still included, as it is found to impact both the vortex lifetime (Zhu and Baruteau, 2016; Regály et al., 2017) and the dust dynamics (Baruteau and Zhu, 2016) given our range of disk parameters. The importance of self-gravity will be further emphasized in Section 6.1. A softening length of $0.3H(r)$ is applied in the calculation of the self-gravitating acceleration, with $H(r) = h \times r$ the disk's pressure scale height, this value is used to mimic the effect of a finite disk thickness. Likewise, a softening length of $0.6H(r)$ is used in the calculation of the acceleration of the planets on the gas, needed to avoid numerical divergence close to the planet's location. Moreover, this softening parameter is about the recommended softening factor for the planet gravitational potential to correctly recover the 3D effects of vertical stratification ($0.6H(r) - 0.7H(r)$, see e.g. Kley and Nelson, 2012).

Turbulent transport of angular momentum is modeled by a constant alpha turbulent viscosity $\alpha = 10^{-4}$. Following the α prescription of Shakura and Sunyaev (1973):

$$\nu = \alpha c_s h\,, \tag{3.3}$$

this rather low level of turbulence, which is consistent with the results of 3D, non-ideal, local magnetohydrodynamic (MHD) simulations at few tens of au (see e.g. Simon et al., 2015), is required to avoid a fast decay of the vortices. The vortices in our simulations survive more than 2000 orbits at the inner planet's position (33 au) that is, for more than 0.3 Myr.

The continuity and momentum equations for the gas are solved on a polar grid centered on the star, and the indirect acceleration terms due to the acceleration of the star by the disk and the planets are taken into account. In a frame which is centered on the star and rotates at the angular frequency $\mathbf{\Omega}_f$, the momentum equation for the disk becomes:

$$\begin{aligned}\frac{\partial \mathbf{v}}{\partial t} + (\mathbf{v}\cdot\nabla)\mathbf{v} &= -\frac{1}{\rho}\nabla P - \nabla\Phi_* - \nabla\Phi_{ind} - \nabla\Phi_{sg} \\ &\quad -\mathbf{\Omega}_f \times (\mathbf{\Omega}_f \times \mathbf{r}) - 2\mathbf{\Omega}_f \times \mathbf{v}\,,\end{aligned} \tag{3.4}$$

where Φ_*, Φ_{ind} and Φ_{sg} are the potentials due to the direct gravitational force from the star, the indirect force due to the acceleration of the reference frame (or the star), and due to the disk's and planet's self-gravity. The last two terms in Equation 3.4 are the centrifugal force and the Coriolis force. The pressure term, indirect force term and self-gravity term are

all related to the disk density distribution (ρ) which has to be solved with the continuity equation. Since the numerical grid is centered at the central star, the velocity equations in a rotating frame are

$$\frac{\partial v_r}{\partial t} + v_r \frac{\partial v_r}{\partial r} + v_\phi \frac{\partial v_r}{r \partial \phi} - \frac{v_\phi^2}{r} =$$
$$-\frac{\partial P}{\rho \partial r} - \frac{\partial \Phi_*}{\partial r} - \frac{\partial \Phi_{\rm ind}}{\partial r} - \frac{\partial \Phi_{sg}}{\partial r} + \Omega_f^2 r + 2\Omega_f v_\phi \tag{3.5}$$
$$\frac{\partial v_\phi}{\partial t} + v_r \frac{\partial v_\phi}{\partial r} + v_\phi \frac{\partial v_\phi}{r \partial \phi} - \frac{v_\phi v_r}{r} =$$
$$-\frac{1}{\rho r}\frac{\partial P}{\partial \phi} - \frac{1}{r}\frac{\partial \Phi_*}{\partial \phi} - \frac{1}{r}\frac{\partial \Phi_{\rm ind}}{\partial \phi} - \frac{\partial \Phi_{sg}}{\partial \phi} - 2\Omega_f v_r \,, \tag{3.6}$$

where the indirect potential follows $\Phi_{\rm ind} = -\mathbf{a_c} \cdot \mathbf{r}$, and $\mathbf{a_c}$ is the acceleration of the central star due to the disk's gravity. It is calculated by integrating the gravitational acceleration from each grid cell onto the central star. Indirect forces are calculated at each time step and added to the equation of motion. The simulations are done in the rotating frame with Ω_f equal to the pattern speed of the inner planet.

The grid extends from $0.3r_0$ to $10r_0$ in the radial direction (that is 9.9 to 330 au in physical units), and from 0 to 2π in the azimuthal direction. We use 600 cells in the radial direction with a logarithmic spacing (required for the gas self-gravitating acceleration to be computed via Fast-Fourier Transforms; see Baruteau and Masset, 2008b). We use 900 cells evenly spaced in azimuth. Given our initial surface density profile, the initial mass of the disk amounts to $\sim 0.01 M_\star$. We use wave killing zones as boundary conditions at both inner and outer radial edges of the grid, where the disk fields are damped towards their initial value to minimize the reflection of the wakes produced by the planets. We have checked that a different choice of boundary condition does not affect our results.

3.2 Dust setup

Dust is modeled as Lagrangian test particles that feel the gravity of the star (direct and indirect terms), of the planets, of the gaseous disk (since gas self-gravity is included) and gas drag. However, the dust self-gravity, dust drag onto the gas (or dust feedback), growth and fragmentation are not taken into account in the simulations. Dust turbulent diffusion is also included as stochastic kicks on the particle's position (orbital radius and azimuth) at each timestep following the method presented in Charnoz et al. (2011), where the kicks follow Gaussian distributions with mean and standard deviations (see Ataiee et al. (2018) for more details). The coefficient of dust's turbulent diffusion (D) is taken to be:

$$D = \frac{\nu(1 + 4\mathrm{St}^2)}{(1 + \mathrm{St}^2)^2}\,, \tag{3.7}$$

with ν the local kinematic viscosity of the gas, and St the local Stokes number of the dust (Youdin and Lithwick, 2007).

We use a total number of 10^5 particles with a size distribution $n_{simu}(s) \propto s^{-1}$ for the particles size s ranging from 10 μm to 10 cm (the quantity $n_{simu}(s)\mathrm{d}s$ represents the number of super-particles in the size interval $[s, s + \mathrm{d}s]$ in the simulation). This particular scaling of the dust's size distribution $n(s)$ is chosen for computational reasons, as it implies that there is approximately the same number of particles per decade of sizes. It is important to note that the radiative transfer calculations need a realistic size distribution for the dust, but the only input that they need from the hydrodynamical simulations is the spatial distribution of the dust particles (the method is described in Chapter 4). Given this, we can choose any size distribution in the simulations, as long as there are enough particles per bin size to properly resolve their dynamics.

The dust particles are introduced into the disk gas at 300 orbits after the beginning of the simulation (computed at 33 au), when the planets have already started to open a gap about their orbit, and are located in a ring between 50 au and 96 au, so that they approximately all remain between the gaps. This is meant to maximize the particles resolution at the location of the two dust traps that we propose to account for the asymmetries in the (sub)mm emission of MWC 758. The initial azimuth of the dust particles is sorted out randomly between 0 and 2π. Their initial radial velocity is set to be zero, and their initial azimuthal velocity accounts for the star's gravity and disk's self-gravity. This ensures that the only difference in initial azimuthal velocities between gas and dust is due to the gas pressure gradient. Furthermore, preliminary simulations inspired by the dust trapping predictions of Casassus et al. (2018, see their Section 4.3) have shown that a better agreement between our predicted flux maps in the (sub-)mm and the observed ones could be attained by assuming a particles with internal density of 0.1 $\mathrm{g cm}^{-3}$, independent of the particle's size. All the results presented in Section 5 were obtained with this internal density for both the simulations and radiative transfer. The dust particles used in our calculations can, therefore, be considered as moderately porous particles. A brief discussion on how the particles internal density impacts our results is given in Section 6.3.3.

Table 3.1: Simulations parameters

Parameter	Value
Star mass	1.5 $M_\odot$
Disk gas mass	0.015 $M_\odot$
Inner planet's mass	1 M_{Jup}
Inner planet's location	33 au
Outer planet's mass	5 M_{Jup}
Outer planet's location	132 au
Disk aspect ratio	0.08
Alpha turbulent viscosity	10^{-4}
Dust's initial location	$\in [50 - 96]$ au
Dust size range	$\in [10\,\mu\text{m} - 10\,\text{cm}]$
Dust's internal density	0.1 g cm^{-3}

The dust particles that we simulate are much smaller than the mean free path in our disk model, and the Epstein regime of drag is therefore relevant (see 1.2.2). In this regime, the particle's Stokes number (St), which is the ratio of the particle's stopping time to the dynamical time, can be expressed as:

$$\text{St} \approx 0.15 \times \left(\frac{\text{s}}{1\,\text{cm}}\right) \left(\frac{\rho_{\text{int}}}{0.1\,\text{g}\,\text{cm}^{-3}}\right) \left(\frac{1\,\text{g}\,\text{cm}^{-2}}{\Sigma}\right) , \tag{3.8}$$

where ρ_{int} denotes the particle's internal density, and Σ the vertically integrated gas surface density to the midplane, interpolated at the particle's location (bilinear interpolation). When our simulations reach a quasi-steady state, St varies from $\sim 3\times10^{-5}$ to ~ 2. Note that the so-called short-friction time approximation is used in the simulations for the smallest grains for which the local stopping time is shorter than the hydrodynamical timestep (see e.g. Johansen and Klahr, 2005). A summary of the parameters of the simulation is presented in Table 3.1.

3.3 Planets setup

We explore the mass and position of the planets based on our hypothesis that MWC 758 has two planetary companions. One inside the inner cavity observed at radio wavelengths (see Section 2.1.3), and one external to the spiral arms (see Section 2.1.2). We use as a first constraint the radial positions of the clumps of emission observed with ALMA and VLA, which have to be in agreement with the location of the planet-induced dust traps in our simulation. The mass of the inner planet is chosen such that it opens a mild gap in the gas around its orbit (see more details in Section 5.1), to be consistent with the non-detection of a gap in the near-infrared observations of the MWC 758 disk (Benisty et al., 2015; Reggiani et al., 2017). The mass of the outer planet is taken as the upper mass limit for a companion outside the spirals ($r_P \gtrsim 100\,\mathrm{au}$), as constrained by the L-band observations of Reggiani et al. (2017) adopting hot start evolutionary model for planetary luminosities at near-infrared wavelengths. Our best configuration consists of a Jupiter-mass planet located at 33 au from the central star, and a 5 Jupiter-mass planet at 132 au from the star. Section 6.4 contains a discussion on the location and mass of the possible (proto)planets in the MWC 758 disk. In our simulations, the planet does not migrate in the disk (they remain on quasi-circular orbits). The planet is set up as a point mass which mass is gradually increased over 20 orbits of the inner planet, in order to avoid sudden disturbances on the initial state of the disk. The mass of the planet M_p increases following:

$$M_p^{'} = M_p \left[sin\left(\frac{\pi}{2}\frac{t}{P}\right)\right]^2 , \tag{3.9}$$

where M_p denotes the final mass of the planet and P the planet's orbital period. In the following sections of this work, whenever the time is expressed in orbits, it usually refers to the orbital period at the inner planet's location ($\sim 33\,\mathrm{au}$), which is about 150 yr. The planet's initial velocity is strictly Keplerian, therefore, its angular frecuency Ω_p follows:

$$\Omega_p = \Omega_K(r_p) = \sqrt{\frac{GM_\star}{r_p^3}} , \tag{3.10}$$

where Ω_K denotes the Keplerian angular velocity, and G the gravitational constant, $M_\star$ is the mass of the central star and r_p the planet's orbital radius.

Chapter 4

Radiative Transfer

The outputs of our hydro dust+gas simulation were post-processed with the 3D radiative transfer code RADMC3D [1] (version 0.41, Dullemond et al., 2015). The obtained dust's spatial distribution is used as input to compute the dust's thermal emission at ALMA Band 7 ($\lambda = 0.87\,\mathrm{mm}$) and VLA ($\lambda = 9.0\,\mathrm{mm}$) wavelengths. The gas surface density output is used as input to compute the polarized scattered light in Y-band ($\lambda = 1.04\,\mu\mathrm{m}$). We use 2×10^8 photon packages for the thermal Monte-Carlo calculation of the dust temperature, and photon ray-tracing. The central star is treated as a sphere that emits as a black body, with a radius of $2\,R_\odot$ and an effective temperature of 8130 K (van den Ancker et al., 1998). We assume the disk to be located at 151 pc (Gaia Collaboration et al., 2016), with an inclination of 21° and a position angle of 62° (Isella et al., 2010; Boehler et al., 2017). The scale of our simulations and the assumed distance to the object in our radiative transfer calculations is about 6% smaller than the reported in the latest Gaia data release, which corresponds to $160 \pm 2\,\mathrm{pc}$ (Gaia Collaboration et al., 2018b). However, this small difference has little impact on our results.

4.1 Thermal emission

From the spatial distribution of the dust particles obtained from our 2D simulations we compute the synthetic predictions of the dust's thermal emission. The calculation requires to specify a realistic size distribution $n(s)$ and the total mass that the dust which we simulate would have in the model of MWC 758, the vertical distribution of dust's mass volume density, and the opacities of the dust grains. These quantities are set to better reproduce the observed fluxes of the ALMA and VLA observations of the MWC 758 disk.

[1] `http://www.ita.uni-heidelberg.de/~dullemond/software/radmc-3d/`

4.1.1 Computation of the dust's surface density from dust's spatial distribution

For the calculation of the disk's surface density from the dust particles distribution three quantities must be specified: the power index of the dust's size distribution (p), where $n(s) \propto s^{-p}$, the dust-to-gas mass ratio (χ) and dust maximum size (a_{max}). These values, as quoted above, are set to obtain an accurate reproduction of the observations of the MWC 758 disk in the radio. The dust's size distribution and its total mass are treated as free parameters[2] which we have explored to best reproduce the current ALMA and VLA observations of the MWC 758 disk. As will be shown in Chapter 5, good results are obtained for $n(s) \propto s^{-3}$, a minimum particle size of $10\,\mu$m (same as in the simulations), a maximum particle size of 1 cm, and a dust-to-gas mass ratio (χ) of 3×10^{-2} (3% of the disk gas mass). This corresponds to a total dust mass of $\sim 2.4\times10^{-4}\,M_\star$ (or $\sim 120\,\mathcal{M}_\oplus$) between ~ 40 au and ~ 85 au, which is about $8-10$ times larger than the mass in dust reported in Boehler et al. (2017). The mass difference likely points to optical depth effects (see Section 6.3.2). The impact of the assumed dust's size distribution in the total mass will be discussed in Section 6.3.1. The dust's size range is decomposed into 90 logarithmically spaced size bins between $10\,\mu$m and 1 cm. The procedure is the following: First, we compute the fraction of dust mass in the ith dust size bin:

$$M_{\rm i,d} = \chi M_{gas} \times \frac{a_{inmax}^{4-p} - a_{inmin}^{4-p}}{a_{max}^{4-p} - a_{min}^{4-p}}\,, \tag{4.1}$$

where χ is the assumed dust-to-gas mass ratio and M_{gas} the gas mass of the disk. p is the power index assumed for the dust's size distribution, a_{max} and a_{min} are the maximum and minimum dust size considered in the calculation of the total mass. While $a_{\rm i}nmax$ and $a_{\rm i}nmin$ are the dust sizes in the ith bin and i + 1th bin. Then, the surface density of the particles in the ith bin at every grid cell, including mass normalization, is given by:

$$\Sigma_{\rm i,d}(r,\varphi) = \frac{N_{\rm i,d}(r,\varphi)}{\mathcal{A}(r)} \times \frac{M_{\rm i,d}}{\sum_{r,\varphi} N_{\rm i,d}(r,\varphi)}\,, \tag{4.2}$$

where $M_{\rm i,d}$ is the fraction of dust mass in the ith size bin computed using equation 4.1, $\rm N_{i,d}$ is the number of dust particles in the ith size bin and in each grid cell, while $\mathcal{A}$ is the surface area covered by the grid cell.

[2]Note that the parameters that define the dust distribution and mass can be treated as free parameters because effects of dust drag (or dust feedback to the gas) are neglected in the simulations.

4.1.2 Vertical expansion of the 2D dust's surface density field

To obtain a 3D volume from the 2D dust's surface density, we assume hydrostatic equilibrium for the vertical distribution of the dust's mass volume density. For each size bin a Gaussian profile is adopted in which the dust's scale height $H_{\mathrm{d,i}}$ of the ith size bin is given by:

$$H_{\mathrm{d,i}} = 0.7H \times \left(\frac{\mathrm{St_i} + \mathrm{St_i^{-1}}}{10^3} \right)^{0.2} . \tag{4.3}$$

These equations correspond to a simple extrapolation to large Stokes numbers of the equation (25) in Fromang and Nelson (2009). In equation 4.3 $\mathrm{St_i}$ denotes the average Stokes number of the dust particles in the i$^{\mathrm{th}}$ size bin, and H the gas pressure scale height. H is obtained $H = h_{sim} \times R$ with h_{sim} the initial disk aspect ratio (H/R) from the simulation. Note that as we are assuming a 'flat disk' i.e. zero flaring index (h_{sim} is the same for every R). Then, to obtain the density volume we assume the classic equation used for the vertical hydrostatic equilibrium for isothermal disks (e.g equations (14) and (15) from Armitage, 2015). This equation assumes that the disk is geometrically thin ($H_{\mathrm{d}}(r)/r << r$) and the vertical sound crossing time is shorter than the radial drift timescale of the dust. For every dust size bin i, the equation is the following:

$$\rho_{\mathrm{d,i}}(z) = \rho_{0,\mathrm{i}} exp \left(-\frac{1}{2} \frac{z^2}{H_{\mathrm{d,i}}^2} \right) ; \rho_{0,\mathrm{i}} = \frac{\Sigma_{\mathrm{d,i}}}{\sqrt{2\pi} H_{\mathrm{d,i}}} , \tag{4.4}$$

where $\Sigma_{\mathrm{d,i}}$ is dust's surface density and $H_{\mathrm{d,i}}$ is the pressure scale height of the ith dust size bin (obtained with Eq. 4.3). For spherical coordinates $z = Rcos(\theta)$, with θ the angle in colatitude relative to the disk midplane.

4.1.3 Computation of the dust opacities

To compute opacities for the dust particles, we assume that the dust is a mixture of a silicate matrix (internal density of 3.2 g cm^{-3}), an amorphous carbon inclusion (internal density of 2.3 g cm^{-3}), and a vacuum inclusion. Assuming that the mixed aggregate has 60% of its solids being silicates and 40% carbons. The level of porosity (or volume fraction of vacuum) needed is $\sim 96\%$ for the porous grains (internal density of $0.1\,g\,cm^{-3}$) and $\sim 64\%$ for compact grains (internal density of $1.0\,g\,cm^{-3}$) . We apply the Bruggeman's model rule for spherical inclusions to compute the optical constant of the mix. The optical constants for amorphous carbon and astronomical silicates are taken from Li and Greenberg (1997) and Draine and Lee (1984), respectively. We use the Mie theory to compute the absorption opacities, the scattering opacities, and the mean scattering angle Bohren and Huffman (1983). The scattering assumed in the calculation is the Henyey-Greenstein scattering with its approximate formula, with g the parameter of anisotropy $g =< cos\theta >$, where θ the deflection angle assumed to be equal to the mean scattering angle. The same procedure is used to obtain the opacities for 'compact grains', which have internal densities of $1\,g\,cm^{-3}$. The opacity used for the synthetic maps of the dust's thermal emission is the total (absorption+scattering) opacity. In Fig. 4.1 we show the opacity as a function of dust grain size used in the thermal emission maps for both compact and porous grains. We have checked that both the scattering and absorption opacities are in accordance with the results obtained by Kataoka et al. (2014). The results presented in Section 5.1.2 have been computed adopting anisotropic scattering (Henyey and Greenstein, 1941). A different treatment of scattering in the calculation of the synthetic flux maps could produce substantial changes in the results (e.g. Sierra et al., 2017). These changes include variations in the observed level of emission and morphology, especially at ALMA wavelengths.

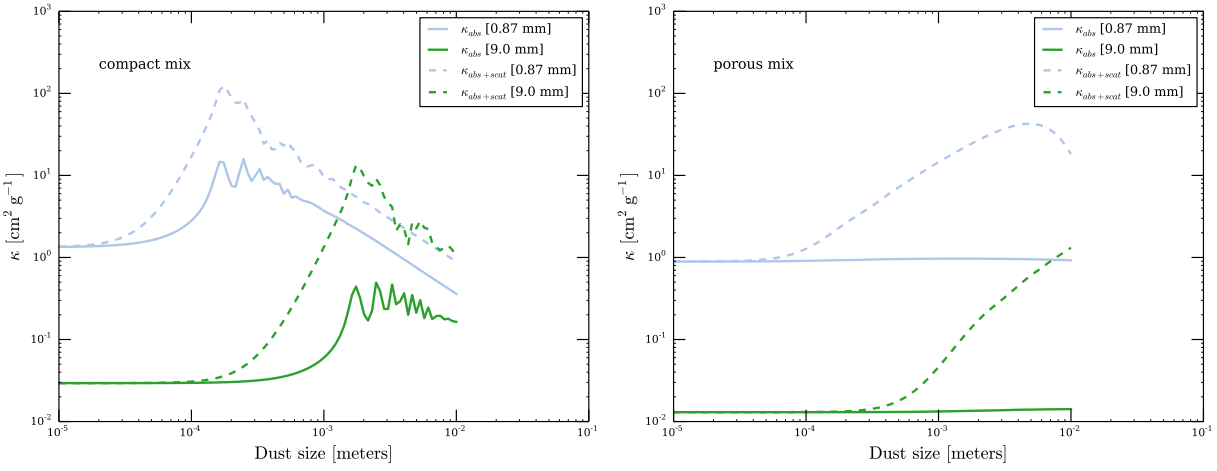

Figure 4.1: Opacities used for the radiative transfer calculations at 0.87 mm and 9 mm, in blue and green, respectively. The solid line represents the values considering absorption opacities only, while the dashed lines consider the sum of the scattering and absorption opacities. **Left:** Results for the compact grains mixture. **Right:** Results for the porous (or fluffy) grains mixture. Note that the opacities are displayed up to 1 cm in size, but for the compact case the calculation only takes into account grains up to 1 mm.

4.2 Polarized scattered light

The observations of the polarized scattered light traces (sub)micron-sized dust grains at the surface of the disk. These particles are not included in our simulations (the minimum size for particles in the simulation is 10μm). To produce scattered light predictions, we add 10 bins of small grains with sizes ranging from 0.01μm to 1μm. We assume that the small dust grains are well coupled to the gas (see Section 1.2.2). Then, to obtain a density volume for these small grains we use the output of the gas surface density and vertically expanded using a Gaussian distribution function assuming hydrostatic equilibrium (Eq. 4.4). Therefore, we set the dust's scale height and surface density at the midplane to be equal that of the gas, H_{gas} and Σ_{gas}, respectively, for every size bin, i.e.:

$$\rho_{\rm d,i}(z) = \rho_{0,\rm i} exp\left(-\frac{1}{2}\frac{z^2}{H_{gas}^2}\right); \rho_{0,\rm i} = \frac{\Sigma_{gas}}{\sqrt{2\pi}H_{gas}}\,. \tag{4.5}$$

The small particles are set to have a size distribution $n(s) = s^{-3.5}$, an internal density of $2.9\,\mathrm{g\,cm^{-3}}$, and are composed of a mixture of 70% silicates and 30% amorphous carbons. The total mass of small dust assumed in our model is $1.7 \times 10^{-4} M_{\odot}$. We use the same method to compute the opacities for small grains as that described in Section 4.1.3 for the large grains. Note that a much higher internal density is adopted for the small dust grains in the calculation of the polarized scattered light than for the large dust particles in the calculation of the dust's thermal emission. This point is probably not crucial, however, since we will not compare absolute intensities of polarized scattered light between the model and the observations.

We artificially reduce the gas pressure scale height beyond the stellocentric distance of 65 au to decrease the photons received (and therefore scattered) by the disk at and beyond the outer tip of the spiral arms structure. We reduce the scale height by a factor proportional to r^2 in order to mimic the shadowing effects due to the spirals propagating between the two planets. If the artificial reduction is not applied the outer horse-shoe shaped gas structure that corresponds to the outermost vortex appears strong in the synthetic predictions of the polarized scattered light, which is not present in Benisty et al. (2015) nor in Reggiani et al. (2017) observations. Therefore, we suggest that this structure may be in the midplane of the disk or shadowed by the large-scale spirals.

To obtain the synthetic maps of polarized scattered light, we compute the emergent Stokes maps Q and U at Y-band ($\lambda = 1.04\,\mu$m) which represents linear polarized intensities. These parameters were calculated following the double-ratio method used for high-contrast imaging (see e.g. Avenhaus et al., 2014). Scattering is assumed to be anisotropic, and a full treatment of polarization is adopted using the scattering matrix as implemented in RADMC3D. Instead of computing the polarized intensity via sum of squares, i.e.,

$$PI = \sqrt{Q^2 + U^2}\,, \tag{4.6}$$

we post-process the Stokes maps to obtain the local Stokes[3] Q_ϕ and U_ϕ following the procedure described in, e.g., Avenhaus et al. (2017):

$$Q_\phi = +Qcos(2\phi) + Usin(2\phi)\,, \tag{4.7}$$

$$U_\phi = -Qsin(2\phi) + Ucos(2\phi)\,, \tag{4.8}$$

$$\phi = \arctan\frac{x - x_0}{y - y_0} + \theta\,, \tag{4.9}$$

where ϕ refers to the azimuth in polar coordinates and is the position angle of the location of interest (x, y) with respect to the position of the central star, located at (x_0, y_0). θ is a free parameter that accounts for corrections due to instrumental effects, assumed to be zero in our case. Q_ϕ contains all the azimuthally polarized flux as a positive signal, whereas U_ϕ contains all polarized flux with a 45° offset from the azimuthal direction (i.e. polarization signal perpendicular to the incident light). Thus, the U_ϕ image remains free of disk signal, so it shows very little signal and should be zero on average. In the observations U_ϕ could also be used as an estimate of the noise levels in the Q_ϕ image. The same procedure was used by Benisty et al. (2015) to obtain the observed Q_ϕ maps of MWC 758. A circular mask of $0\farcs2$ in radius is applied to the predictions so as to enhance the brightness of the spirals. Each pixel of the Q_ϕ synthetic image is scaled with the square of the deprojected distance from the central star, in order to compensate for the radial dependence of the stellar radiation field and highlight the structures at large radius. Finally, the image is convolved by a circular beam of FWHM $0\farcs026$ to reach the same resolution of the Y-band polarized scattered light observations images presented in Benisty et al. (2015).

[3]This procedure is convenient since, if the disk is nearly face on, the polarized scattered light from a circumstellar disk is expected to be linearly polarized in the azimuthal direction, assuming single scattering events. Thus, we can assume that the angle of linear polarization shows an azimuthal alignment with respect to the central star, making it useful to describe the polarization vector field in polar coordinates.

Chapter 5

Results

We present in this section the results of our hydrodynamical simulations and radiative transfer calculations, starting in Section 5.1 with the time evolution of the gas surface density and of the dust's spatial distribution in response to the two planets. As we will show, the planets trigger the formation of vortices at the edges of their gap as result of the Rossby-wave instability (RWI), and dust particles become progressively trapped within the vortices. Vortices are not long-lived structures, and when the vortex latter decays the dust particles can successively lose their azimuthal trapping. Based on the ALMA and VLA continuum emissions predictions in comparison with the current ALMA and VLA observations of MWC 758, we argue that Clump 1 is consistent with azimuthal trapping in a vortex, while clump 2 is more consistent with dust trapped in a decaying vortex, where the vortex is in a stage where the dust particles have already lost, in a certain degree, its azimuthal trapping. This is what we show in Section 5.1.2 and 5.1.3 , where we compare our predicted maps of the continuum and polarized scattered light with the observations.

5.1 Gas and dust evolution

The planets in our disk model progressively carve a gap in the gas about their orbit. This is illustrated in the left panel of Fig. 5.1, which displays the perturbed gas density relative to its initial radial profile:

$$\Sigma_{\rm perturbed} = \frac{\Sigma - \Sigma_0}{\Sigma_0}\,, \tag{5.1}$$

computed at 1323 orbits after the beginning of the simulation (which corresponds to $\sim$ 0.2 Myr after the planets have reached their final mass). The white circles spot the position of the planets. On azimuthal average, the gas surface density has decreased by about 60% of its initial value at the bottom of the inner planet's gap, and by about 90% at the bottom of the outer planet's gap. These values are consistent with the gap-opening criterion of Crida et al. (2006), according to which the minimum planet-to-star mass ratio for a planet to open

a gap with a gas density drop of about 90% is $q_{gap} \approx 9.7 \times 10^{-4}$ for our disk model, where both the alpha turbulent viscosity and the disk's aspect ratio are uniforms (the above value is obtained via Eq. 10 in Baruteau et al., 2014). This mass ratio is larger indeed than that of the inner planet ($q_{in} = 7 \times 10^{-4}$) and smaller than the outer planet's ($q_{out} = 3.3 \times 10^{-4}$). We point out that the inner edge of the gap carved by the outer planet in the disk gas, which is about 85 au, is consistent with the truncation radius of the disk ring observed in $C^{18}O$ presented in Boehler et al. (2017, see their Figure 4).

The left panel in Fig. 5.1 also shows multiple spiral arms in the disk gas, with some spirals more prominent than others. It is actually not straightforward to tell from the image where each spiral originates since spirals are triggered by the planets and by the gas vortices that form in the disk. A large-scale vortex can be seen at the inner edge of the outer planet's gap, although its structure is not smooth because of one or several spirals passing through the vortex. The fact that the outer planet forms a vortex at the inner edge of its gap via the Rossby-Wave Instability is the consequence of the rather large planet's mass, which allows the persistence of a radial pressure bump at this location given the local turbulent viscosity (Bae et al., 2016). We have checked with a dedicated simulation that a very similar vortex structure forms in the absence of the inner planet as observed in the upper panels of Fig. 5.3 were we show the perturbed density and vortensity maps that result from the interaction between the gas disk and the single planet at 132 au only. This indicates that the wakes induced by the inner planet have no significant impact on the growth and evolution of the vortex produced by the outer planet. A large-scale vortex also forms at the outer edge of the outer planet's gap, located at about 220 au as shown in Figure. 5.5. There is no indication of emission at that distance in the (sub)mm observations of MWC 758 that could trace a dust trapping vortex outside the outer planet's putative location. A possible explanation for the lack of radio emission could be that the vortex exists in the gas but is inefficient at trapping dust, or that the amount of dust trapped inside the vortex at this location is too small to have a measurable effect on the thermal emission. A second explanation is the tidal truncation of the outer parts of the gas disk. However, this scenario is unlikely for our model as a more massive companion at the outer regions is needed. The possibility of such a massive companion is addressed in Section 6.4. In any case, a detailed study of this issue is beyond the scope of our work and need further theoretical study.

The right panel in Fig. 5.1 shows again the perturbed gas surface density, but now with the location of the dust particles up to 1 cm in size overlaid with colored dots (color varies with particles size, see the color bar on the right-hand side). These particles have a Stokes number ranging from about 3×10^{-5} to 0.15. We see that nearly all dust particles are confined between the planets, and more particularly along two rings. This is because the particles are inserted between the planets at 300 orbits after the beginning of the simulation when the planets have already started to carve their gap. Particles thus drift towards the inner edge of the outer planet's gap, or towards the outer edge of the inner planet's gap, since both locations are pressure maxima in the radial direction[1]. We see that a few (mostly small) particles can cross the inner planet's gap, which is due to the effect of dust turbulent diffusion kicking particles away from (and inside of) the gap's edge.

The presence of a vortex at the inner edge of the outer planet's gap can be clearly inferred from the asymmetry in the dust's spatial distribution at this radial location, in particular with the azimuthal width of the dust distribution decreasing with increasing particles size, which is due to larger particles drifting more rapidly towards their trapping location. We see that the azimuth at which particles are trapped in the vortex varies continuously with increasing particles size. For instance,the smallest particles i.e. particles between $10\,\mu$m and $100\,\mu$m, which have $\mathrm{St} \in [5 \times 10^{-5} - 3 \times 10^{-3}]$ and which therefore trace the vortex centre, have a peak distribution located about 35 deg to 45 deg ahead of the inner planet (counterclockwise in Fig. 5.1). On the other end of the size distribution, i.e. large particles that are between 0.8 cm and 1 cm in size, which have $\mathrm{St} \in [0.06 - 0.1]$, peak at about 125 deg ahead of the inner planet. Said differently, the largest particles are trapped 80 deg to 90 deg ahead of the vortex center. This azimuthal distribution stems from the competition between gas drag and the vortex self-gravity acting together on the dust particles (Baruteau and Zhu, 2016).

[1]If particles are included at the beginning of the simulation, when there are no pressure bumps in the disk, the particles radially drift towards the star and most of them end up trapped in the inner planet's outer edge. Therefore, the dust's spatial distribution at later stages, and consequently the synthetic thermal emission maps, are sensitive to the initial location and gas evolutionary stage in which the particles are introduced in the simulation.

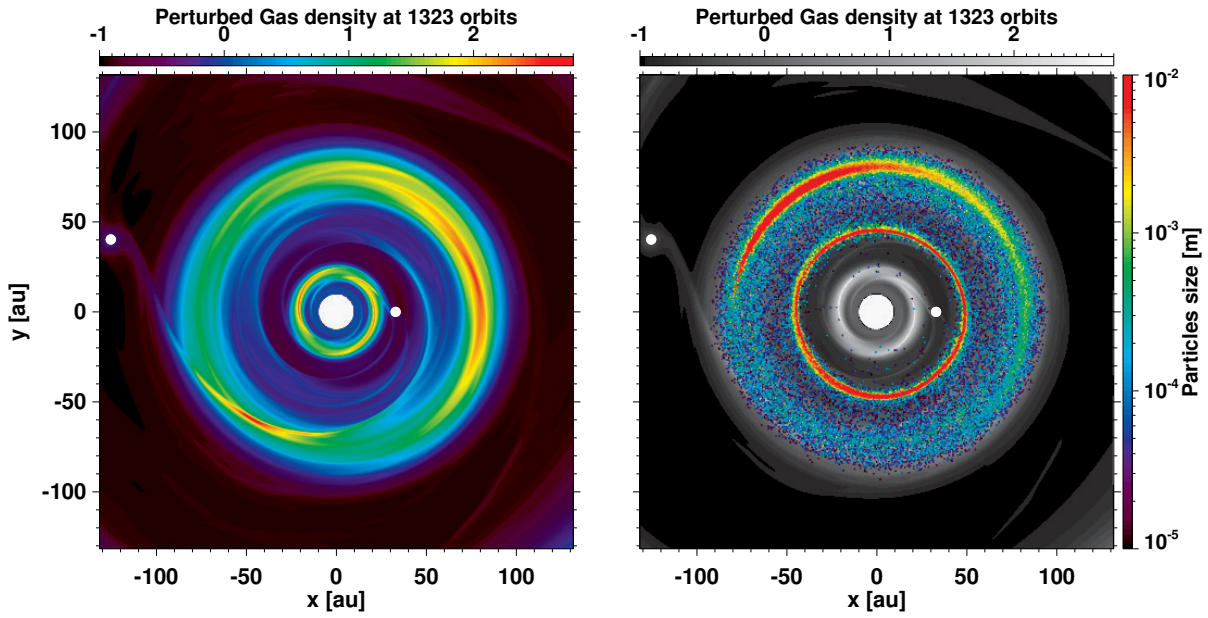

Figure 5.1: Results of our best-case hydrodynamical simulation after 1323 orbits of the inner planet. **Left:** perturbed gas surface density relative to its initial profile. **Right:** same as the left panel, but with the spatial distribution of the dust particles overlaid (colored dots). The color bar indicates the dust size in meters. In both panels, the position of the planets is marked by white circles.

In comparison, the distribution of the dust particles along the ring that is located at the outer edge of the inner planet's gap looks much more axisymmetric and is not really indicative of azimuthal trapping in a vortex. More insight into the dust distribution along both rings can be gained by inspection at Fig. 5.2. The figure shows the gas surface density (left panels), the perturbation of gas vortensity [2] relative to its initial profile (middle panels, $\omega/\omega_0 - 1$), and the spatial distribution of the dust particles (right panels). Results are displayed in polar coordinates with the radius range ($x-$axis) narrowed to highlight the gas and dust distributions between the planets. Also, note that the non-linear color maps and different limits of the color bar are set to distinguish the asymmetric features. The lower panels are at 1323 orbits, the same time as the results shown in Fig. 5.1. The anticyclonic vortex at the inner edge of the outer planet's gap (near 80 au) is clearly visible in the bottom middle panel in Fig. 5.2 as a local minimum in the gas vortensity (it is a local minimum both in the radial and azimuthal directions). Comparison with the upper-left panel underlines that it is not easy to distinguish the presence of the vortex solely based on the gas surface density, as we clearly see 2 to 3 spiral arms going through the vortex. The top right panel makes it clear that dust trapping does not correlate with maxima in the gas surface density, but rather with minima in the gas vortensity. Therefore, the vortensity minimum coincides with the location where most dust particles concentrate. Interestingly, we see that the dust particles along the inner ring do not share the same orbital radius, as if they had a little bit of eccentricity. The

[2] In 2D, the vortensity (or potential vorticity), which we denote by ω, is the ratio of the z-component of the curl of the (2D) velocity to the gas surface density. We denote ω_0 the initial radial profile of the gas vortensity. Vortensity tends to be conserved along streamlines, diffused by the action of turbulent viscosity, and created at shocks or at locations where surfaces of constant density and pressure are not aligned (baroclinic source term).

largest, cm-sized particles along the inner ring have orbital radii ranging from about 44 to 50 au at this time in the simulation, which is equivalent to a local eccentricity of about 0.06.

If we look at an early stage of evolution, for example, the upper panels in Fig. 5.2, which are at an earlier time in the simulation (600 orbits), we see that the two vortices are more prominent than at later in the simulation. The perturbed vortensity and dust distribution highlight the presence of two dust trapping vortices: one at a stellocentric distance of ~ 80 au, which is still active at 1323 orbits, and a secondary one at ~ 47 au from the star, which is no longer active at 1323 orbits. The comparison between the different evolutionary stages in Fig. 5.2 shows that the dust particles which are located along the inner ring are initially trapped in a vortex, but this vortex later decays. We can deduce this by looking at the perturbed gas vortensity. While we observe a clear local minimum at 600 orbits in the azimuthal and radial directions, only a radial minimum is observed at the outer edge of the inner planet's gap at 1323 orbits, which means that the vortex it is no longer active in the velocity field. On the other hand, the spatial distribution of particles along the ring reflects that the particles have lost memory on their former azimuthal trapping, which happens at different timescales depending on the size of the particle, where the larger particles lost its trapping faster. A similar mechanism was studied in similar dust+gas simulations to explain the recent (sub)mm observations of the AB Aurigae disk (Fuente et al., 2017). The comparison between the vortensity fields also suggests that the outer vortex is probably decaying, as its corresponding local vortensity minima is broader azimuthally at 1323 orbits than at 600 orbits. We have checked that the outer vortex is still active at the end of our simulation at 1500 orbits.

From the density and vortensity fields, we can analyze the aspect ratio χ of the vortices, which measures their elongation. Rough estimates of this value could be obtained for the different quantities, using contours of constant value. For the vortensity map at 600 orbits (see middle panel of 5.2), for example, the aspect ratio of the outer vortex at ~ 80 au can be estimated using the light blue contour which marks a relative perturbation of vortensity of about -0.74. In doing so, the vortex can be approximated as an ellipse that extends from about -2 to 2 rad in azimuth, and from about 75 to 85 au in the radial direction, which correspond to $\chi \sim 17$. Interestingly, a similar aspect ratio can be estimated using the iso-contours for the inner vortex at ~ 47 au, and for the outer vortex at 1323 orbits. In the same line, we have recovered similar values of χ based on the reconstructed dust's surface density and measuring their aspect ratio. Also, the aforementioned χ value for the outer vortex is coincident with the one obtained from the raw thermal emission maps at $\lambda \sim 0.9$ mm and $\lambda \sim 9$ mm, via Gaussian fitting (see also 5.1.2).

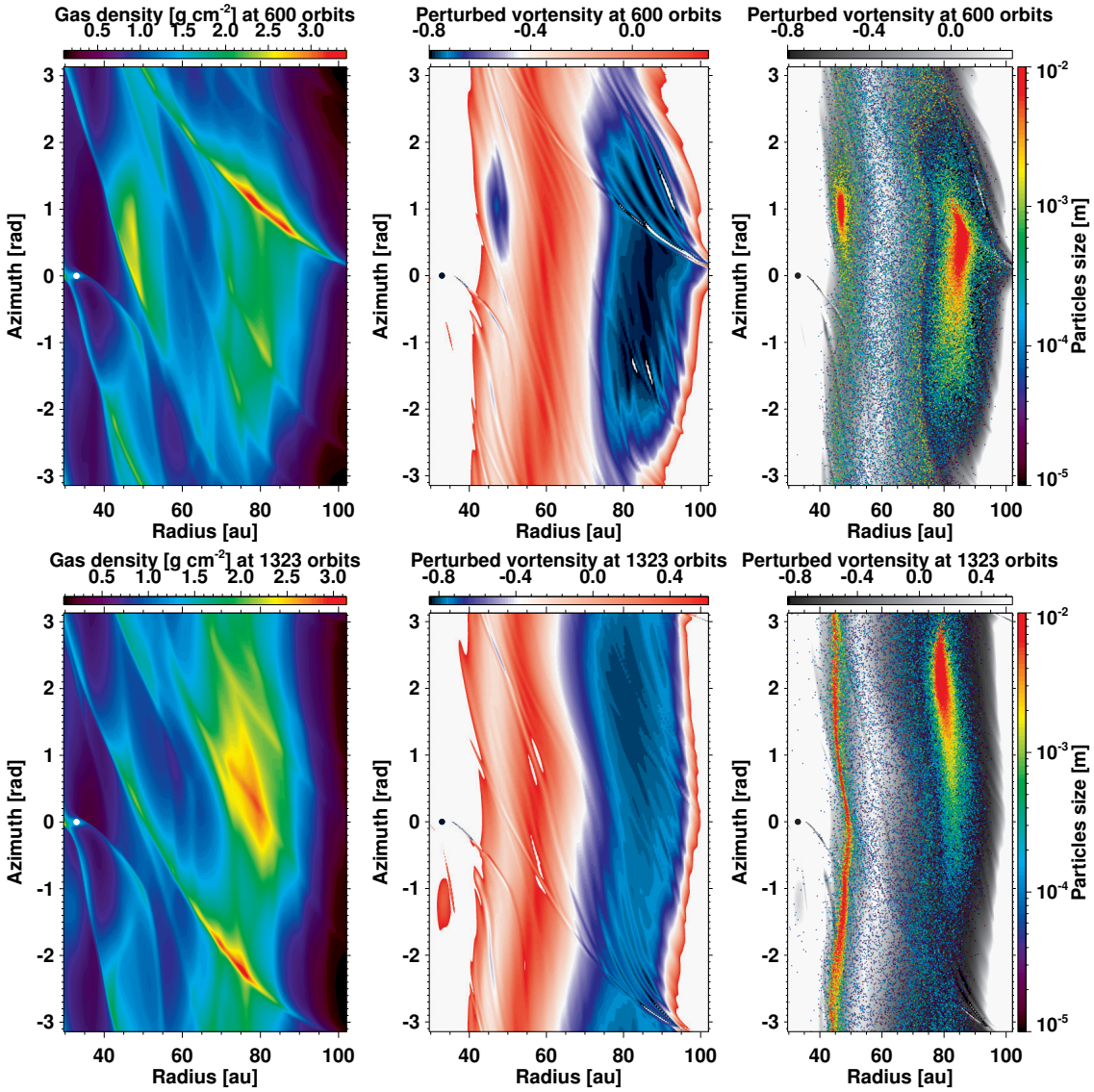

Figure 5.2: Results of the gas physical properties and dust spatial distribution of the hydrodynamical simulation for MWC 758, after 1323 orbital periods (lower panels, same time as 5.1), and 600 orbital periods (upper panels). **Left:** Gas surface density.**Middle:** Perturbed gas vortensity relative to its initial profile $(\omega - \omega_0)/\omega_0$). An aggressive color scale has been set to highlight the local minimum of vortensity, which traces the location of the gas vortices. **Right:** Same as the middle images, but with a linear grayscale for the perturbed vortensity, and the dust particles location overplotted. The color bar on the right shows the dust size in meters. All images are in polar cylindrical coordinates with the x-axis in radians and the y-axis in astronomical units. The position of the planet is shown by a black circle at zero azimuth. The outer planet is outside the image domain (at $r = 132\,\mathrm{au}$).

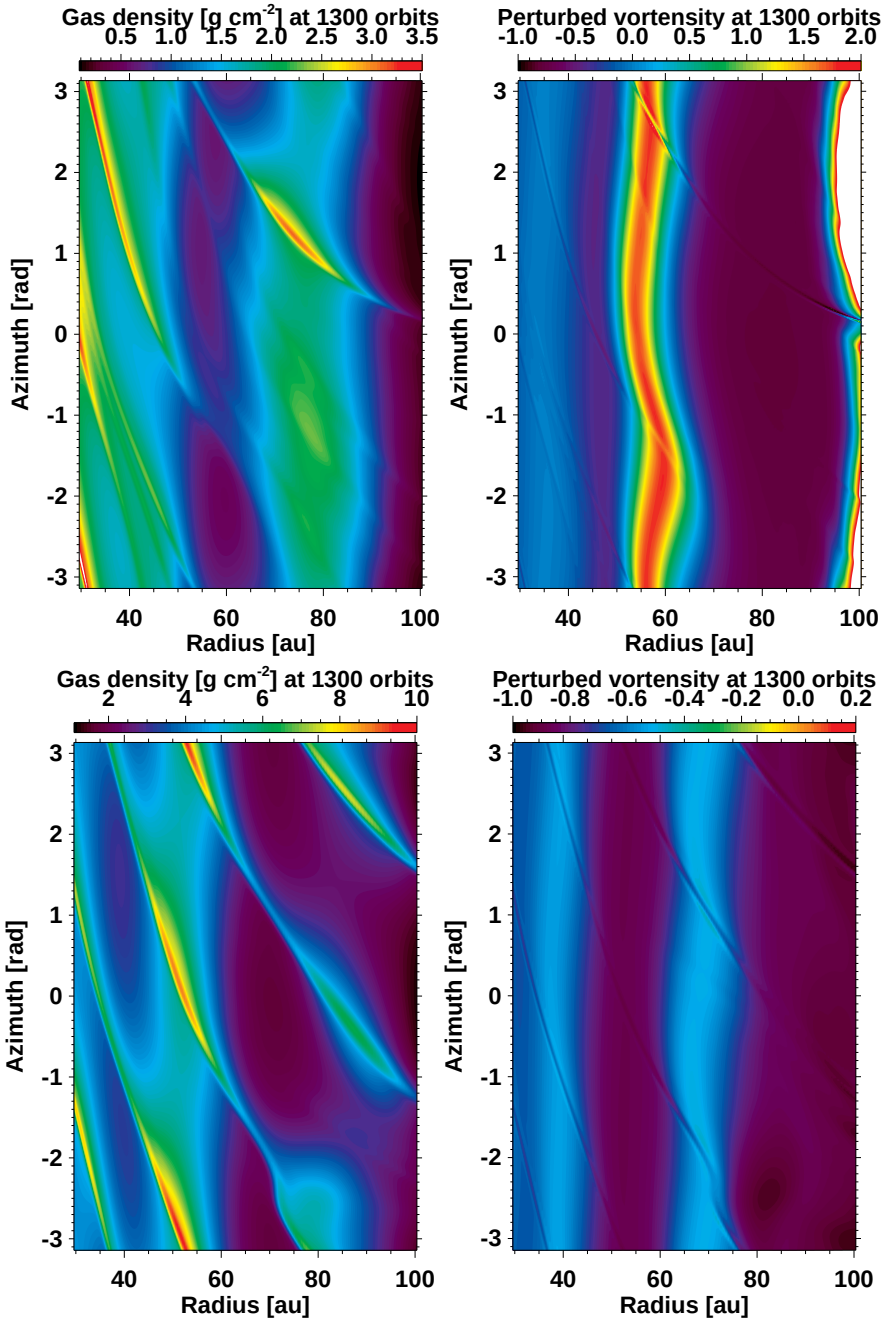

Figure 5.3: Results of hydrodynamical simulations with an outer companion only, after 1300 orbital periods computed at 33 au. **Upper row:** Gas surface density (left) and perturbed vortensity (right) for a simulation with a planet of 5 M_{Jup} at 132 au. **Right:** Same as upper row, but for a simulation with a substellar companion of 0.1 $M_\star$ at 300 au. All images are in cylindrical polar coordinates with the y-axis in radians and x-axis in astronomical units.

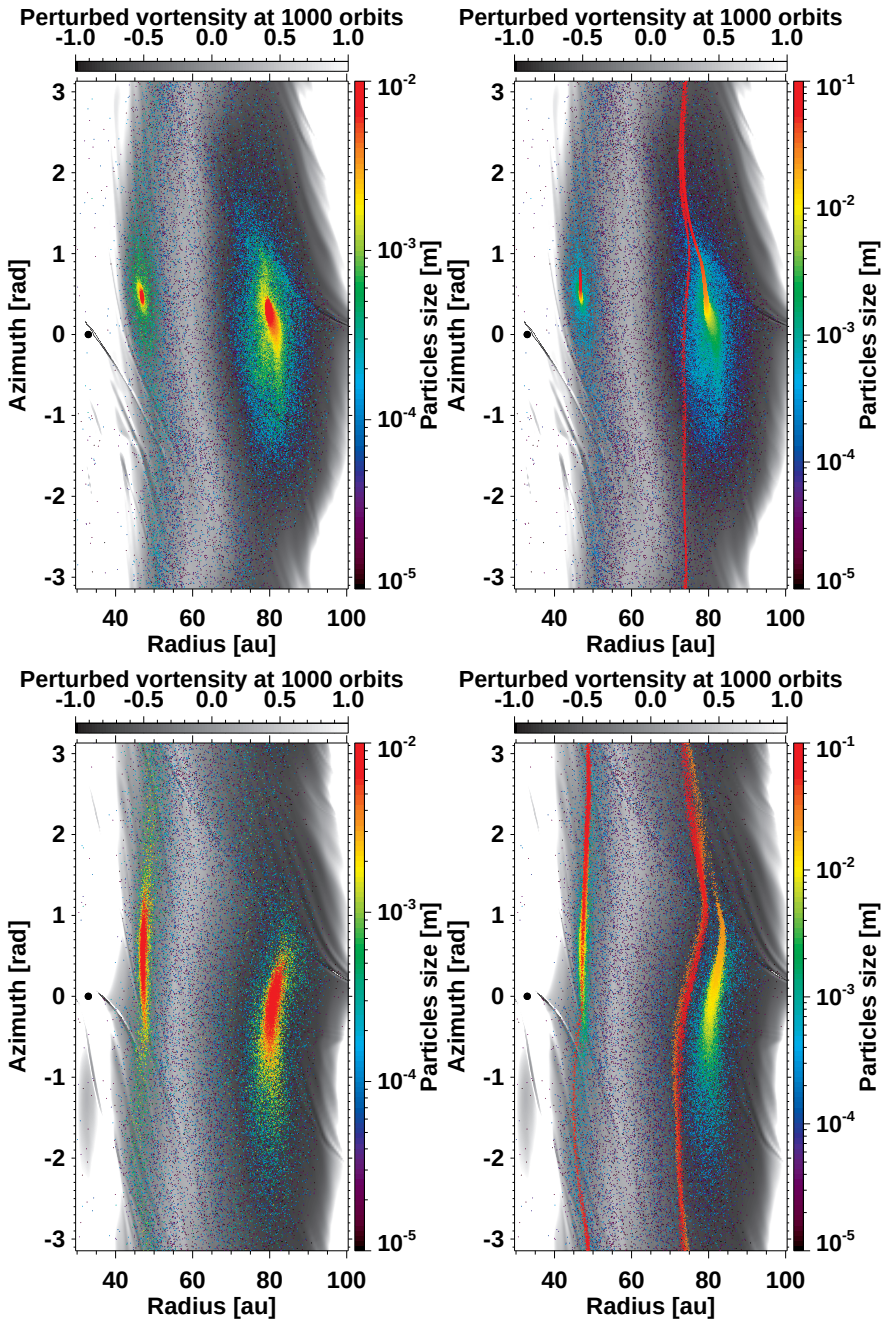

Figure 5.4: Results of hydrodynamical simulations for the two planets configuration displayed in Fig. 5.2, but different alpha turbulent viscosity values are set for the simulations (difference of one order of magnitude). The images are computed after 1000 orbital periods at the position of the inner planet (33 au). **Upper row:** Results of a simulation with an alpha viscosity value of $\alpha = 10^{-5}$. At the left is the perturbed vortensity in grayscale, with dust particles up to 1 cm in size overplotted. At the right panel is the same perturbed vortensity field displayed in the left-hand side panel, but including particles up to 10 cm. **Lower row:** Same as the upper row, but for a simulation with an alpha viscosity value of $\alpha = 10^{-4}$, the value used for our best match with the observations. The color bar indicates the dust size in meters. All images are in cylindrical polar coordinates with the y-axis in radians and x-axis in astronomical units.

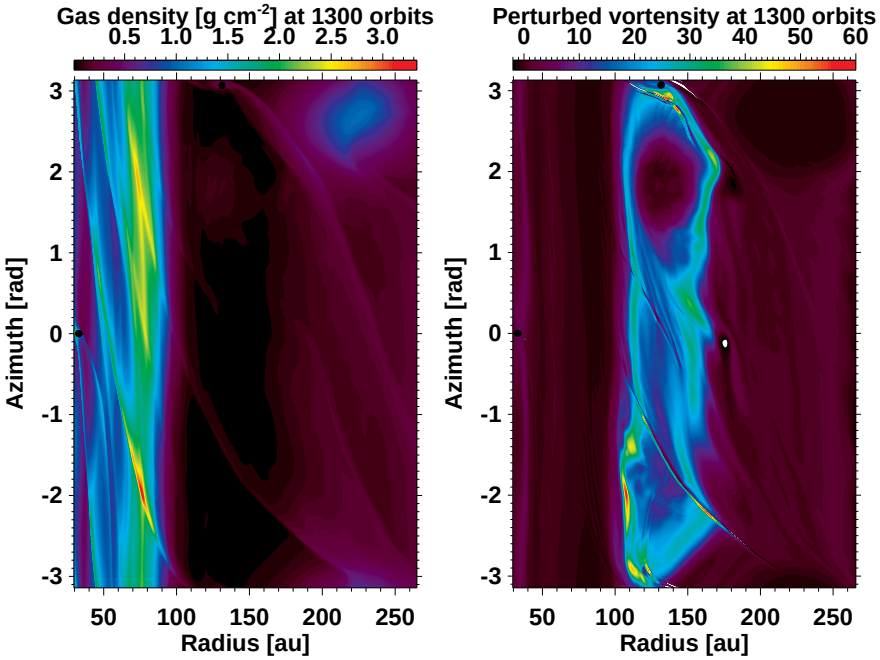

Figure 5.5: Results of hydrodynamical simulations for the two planets configuration displayed in Fig. 5.2, but for a larger domain in radius ($r_{max} \approx 300$ au), after 1300 orbital periods computed at 33 au. **Left:** Gas surface density. **Right:** Perturbed vortensity. The images are in polar cylindrical coordinates with the y-axis in radians and the x-axis in astronomical units.

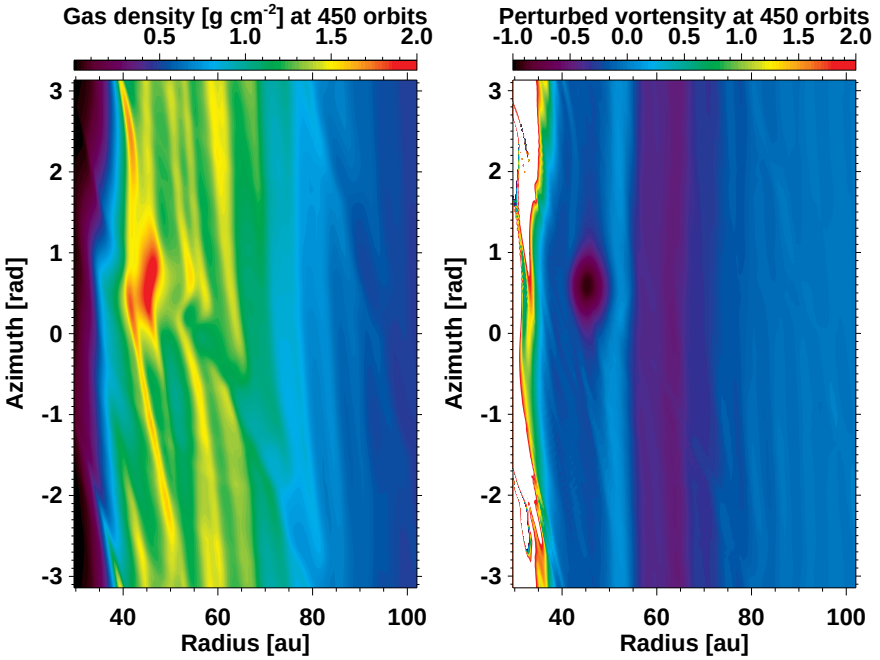

Figure 5.6: Results of hydrodynamical simulation for a planet of 30 M_{Jup} at 20 au from the star, which is about the stellocentric distance of the point-like source reported by Reggiani et al. (2017). The outputs are computed after 450 orbital periods at 33 au. **Left:** Gas surface density. **Right:** Perturbed vortensity. The images are in polar cylindrical coordinates with the y-axis in radians and the x-axis in astronomical units.

5.1.1 Temperature profile

For the dust model used in the hydrodynamical simulation we compute the dust temperature via a Thermal Monte Carlo calculation. The profile of the temperature does not match perfectly the temperature assumed in the simulation shown in Fig. 5.7, which displays the azimuthal average of the dust temperature as function of radius, for different colatitude angles quoted in degrees (angle between the midplane and the specific location measured from the center of the model). Overlaid, with a black dashed line, is the temperature profile set in the hydrodynamical simulation, which corresponds to a power law $T \propto r^{-1}$ taken as an approximation of the reported temperatures obtained from ALMA observations of MWC 758 (Boehler et al., 2017). Close to the disk's surface the temperature profile is consistent with a passively irradiated disk ($T \propto r^{-1/2}$), values that decrease closer to the midplane. A break at $\sim$ 45 au is consistent with the beginning of the outer edge of the inner dust cavity. The difference between the midplane temperature reported in Boehler et al. (2017) for MWC 758, and the obtained in the radiative transfer calculation is negligible at Clump 1 and Clump 2 radial positions, which are about $\sim$ 80 au and $\sim$ 50 au, respectively. This allows us to use the ratio of the peaks of emission between Clump 1 and Clump 2 as a constraint for the model. This because the differences of between the aspect ratio computed from the model and from the observations will not result from differences in the local temperature at the clumps positions, but from the selection of different sets of dust's parameters for the model and dust dynamical evolution. The results of the calculation of the emission peak ratio between the Clumps are presented in the following Section 5.1.2, and a discussion of the factors that affect this ratio are discussed in Chapter 6.

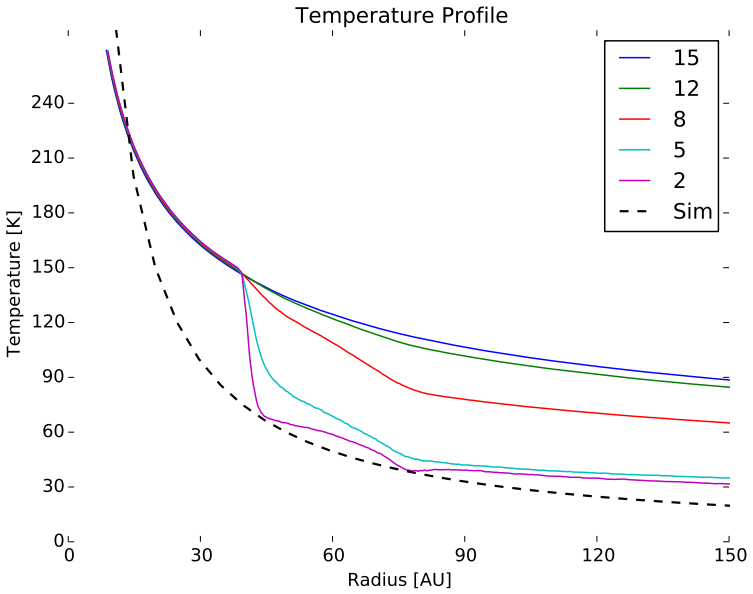

Figure 5.7: Temperature profile obtained via radiative transfer Thermal Monte Carlo of the simulation model. The different colored lines represent the values of the angle in colatitude from the midplane in degrees. The black dashed line denotes the temperature profile adopted in the simulation, which approximately matches the values reported in Boehler et al. (2017) for MWC 758.

5.1.2 Thermal emission in the (sub)mm

A side-by-side comparison of the synthetic maps of thermal emission obtained from our simulations, with the ALMA B7 ($\lambda \sim 0.9$ mm) and VLA Ka ($\lambda \sim 9$ mm) observations reported in Casassus et al. (2018) is displayed in Cartesian and polar coordinates in Figures 5.8 and 5.9, respectively. The synthetic maps were convolved with the same beam as in the observation, to reach a comparable angular resolution ($0\farcs11 \times 0\farcs08$ PA 30 deg for the 0.9 mm prediction, and $0\farcs12 \times 0\farcs10$ PA 65 deg at 9.0 mm). Since the ALMA observation does not show emission at the star's position, the center of the image was shifted by $0\farcs06$ in the direction of PA 28 deg (from north pole counterclockwise), following the procedure of centering optimization used in Casassus et al. (2018). With this method, the inner ring of emission matches approximately a circle centered on the center of the image. In addition, the aforementioned centering of the image allows a more accurate comparison of the ALMA observation with the radiative transfer predictions. The VLA observation shows emission about the position of the star, however, for a proper comparison with our synthetic map, the emission at the star location has been subtracted from the VLA observation images, displayed in the bottom right panels of Figures 5.8 and 5.9. Additionally, the synthetic maps have been slightly rotated so that the position angle of Clump 1 approximately coincides with that of the observations. In the polar maps shown in Fig. 5.9, position angles (x-axis) are relative to that of Clump 1 in the VLA images.

Overall, for the assumed dust properties, our two-vortex model captures the main features of the two clumps of emission observed in the ALMA and VLA images. The dust trapping vortex at the inner edge of the outer planet's gap can reproduce the compact emission associated with Clump 1 (at ~ 1 o'clock in both the ALMA and VLA images). In particular, we recover the fact that Clump 1 is broader at 0.9 than at 9 mm, as expected with azimuthal dust trapping. The decaying vortex at the outer edge of the inner planet's gap can explain why Clump 2 (at ~ 5 o'clock in the ALMA image) has a much larger azimuthal extent than Clump 1 at 0.9 mm. Clump 2 is actually more like a lopsided ring than a compact clump of emission. And importantly, we recover the more diffuse and low level of emission seen in the VLA image for Clump 2. The comparison between the synthetic and observed maps of emission suggest that Clump 1 and Clump 2 lie on top of a fainter ring of background emission, which is corroborated by the recent, high angular resolution ALMA observations of (Boehler et al., 2017; Dong et al., 2018).

Recall that nearly all dust particles in the simulation remain confined between the planets, which is why our synthetic maps have a lack of emission inside $\sim 0\farcs25$ (the sub-mm cavity) and beyond $\sim 0\farcs6$. Lastly, we have checked that the location of the maximum of emission in both synthetic flux maps corresponds to that of the largest dust particles in the results of the dust's spatial distribution of the simulation (those with sizes ranging from a few mm to a cm in size). As highlighted in section 5.1, these largest particles are not located where the gas surface density (or pressure) has its azimuthal maximum, therefore neither do the peaks of thermal emission.

In the following, we provide a more quantitative comparison between our predictions and the observations, in terms of the peak intensities, the widths and aspect ratio of Clump 1, and the eccentricity and contrast ratio of the emission ring along Clump 2. We also quote the peak optical depths that we obtained in the synthetic maps.

Peak intensities

At 0.9 mm, the predicted peak intensities are about 11.7 mJy/beam for Clump 1 and 7.3 mJy/beam for Clump 2. These values agree very well with the observed peaks, with only a $5-10\%$ relative difference. The level of agreement is not as good at 9 mm, with a predicted peak intensity at Clump 1 ($\sim 14\,\mu$Jy/beam) which is about half the observed value, and a predicted peak intensity at Clump 2 ($\sim 3.4\,\mu$Jy/beam) which is about 3 times smaller than the observed value in the VLA image. Still, the predicted peak intensity ratio between Clump 1 and Clump 2 at 9 mm, which is ~ 4.1, remains in moderately good agreement with the observed value (2.7 ± 0.3 Casassus et al., 2018). The same ratio a 0.9 mm is about 1.6, which matches the observed value (1.5 ± 0.1 Casassus et al., 2018). We interpret the much larger peak of intensity ratio at 9 mm than at 0.9 mm as a consequence of the inner vortex decay in our model (see Section 5.1). We have checked this by computing the synthetic flux maps at 600 orbits, when the inner vortex is still active (see upper panel in Fig. 5.2), which show that the peak intensity ratio ranges from about ~ 0.7 to ~ 0.8 at both wavelengths (see Section 5.1.2). Lastly, we measure a very small azimuthal shift in the position of the predicted peak intensities for Clump 1 between 0.9 and 9 mm. We cannot reliably estimate this azimuthal shift in the ALMA and VLA observations, since the center of the images are not perfectly coincident since the star does not show up in the ALMA image.

Widths and aspect ratio of Clump 1

Form the polar maps displayed in Fig. 5.9, which shows the deprojected morphology of the disk, we see that Clump 1 tends to have a slightly larger azimuthal width and smaller radial width in the synthetic maps than in the observations. In the azimuthal direction, the predicted full width half maximum (FWHM) of the convolved intensity across the peak is about 55 deg and 32 deg at 0.9 mm and 0.9 mm, respectively, while the observed values are about 45 deg and 22 deg. Similarly, in the radial direction, the predicted FWHM of the convolved intensity across the peak is about $0\farcs08$ at both wavelengths, while the observed values are about $0\farcs13$ and $0\farcs10$ at 0.9 mm and 9 mm, respectively. Fine tuning of the disk gas parameters (surface density, temperature, alpha viscosity) and the dust parameters (size distribution, internal density) could potentially reconcile our predictions with the data.

Moreover, from the radial and azimuthal widths of Clump 1 in the emission maps, and the radial location of the peak intensity, we can estimate the aspect ratio χ for Clump 1, in a similar manner as presented in Section 5.1. We find that the predicted χ values amount to ~ 6 and ~ 3.3 at 0.9 mm and 9 mm, respectively. On the other hand, the observed values are ~ 3.4 and ~ 2 (with about 10% relative uncertainties). These values are significantly smaller than the obtained via the gas perturbed vortensity for the vortex from which Clump

1 originates (see the last paragraph of Section 5.1). We have checked that this discrepancy comes about because of the beam convolution. Upon calculating the synthetic maps of raw intensity (intensity of thermal emission prior to beam convolution), we obtain $\chi 15\pm$ at both wavelengths, which agrees with the vortex's aspect ratio measured via the gas vortensity, and also with the value reported in Casassus et al. (2018) where steady-state dust trapping predictions based on Lyra and Lin (2013) are used to model the raw intensity for Clump 1 at 0.9 and 0 mm.

Eccentricity and azimuthal contrast ratio of the emission ring along Clump 2

The synthetic polar map at 0.9 mm in the top-left panel of Fig. 5.9 shows that the emission ring that passes through the radial position of Clump 2 it is not circular. This is consistent with the spatial distribution of the largest dust particles along this ring, displayed on the top-right panel in Fig. 5.2, for which we have seen in Section 5.1 that their range of orbital radii corresponds to an equivalent eccentricity of about 0.06. The ALMA polar maps is suggestive that the ring is slightly eccentric (see also Boehler et al., 2017), a result recently confirmed by the higher angular resolution ALMA images in Dong et al. (2018), who have reported a local eccentricity of ~ 0.1, which is not considerably different from the one obtained from our predictions. We finally point out that the azimuthal contrast ratio of the predicted 0.9 mm flux along the ring is a factor of ~ 2.3, which agrees well with the observed value (~ 2.5, see also Boehler et al., 2017). At 9 mm, the predicted contrast ratio is a factor of ~ 3.8.

Peak optical depths

An interesting information that is accessible with our synthetic maps of thermal emission is the optical depth that our model predicts at the location of the peak intensities. At 0.9 mm, we find a peak optical depths of about 25 and 4 for Clump 1 and Clump 2, respectively. At 9 mm, peak optical depths are about 0.4 and 0.07 for Clump 1 and Clump 2, respectively. The thermal emission at 0.9 mm is therefore optically thick near the center of both clumps. Perhaps even more surprising is the rather large peak optical depth at 9 mm near the center of Clump 1. Interestingly, this peak optical depth agrees well with the value of ~ 0.3 predicted by the steady-state dust trapping predictions used in Casassus et al. (2018), although the gas vortex and dust distribution assumed to give rise to Clump 1 in Casassus et al. (2018) have different different set of parameters for the physical quantities of the disk model than in our simulations (e.g. different alpha turbulent viscosity, temperature, dust's internal density etc.; see Section 4.3.2 in Casassus et al., 2018, for comparison).

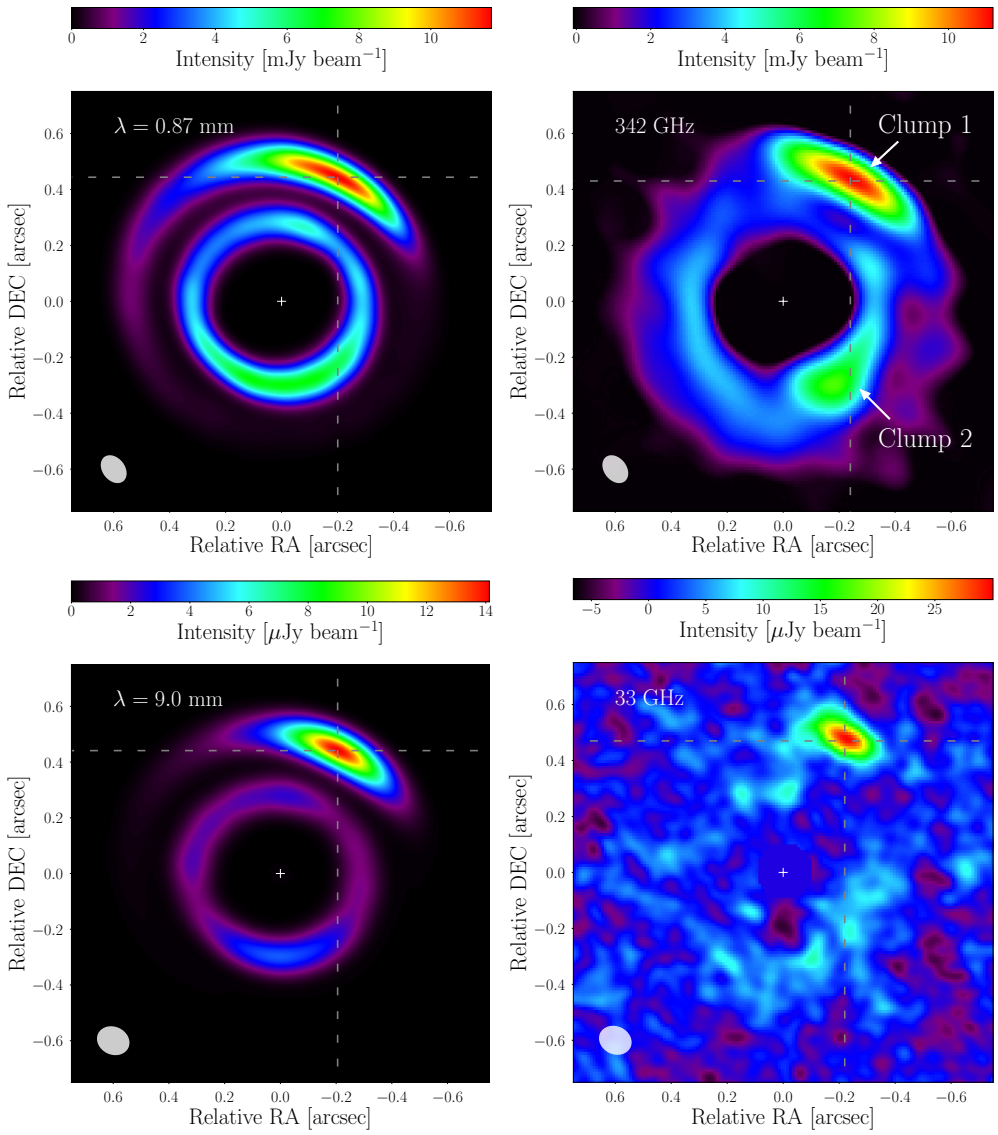

Figure 5.8: Predicted continuum emission at 0.9 mm and 9 mm for fluffy grains (left panels) compared with ALMA Band 7 and VLA observations at the same wavelengths (right panels, Casassus et al., 2018). The star has been subtracted in the VLA image. The synthetic maps were convolved with the same beam as in the observations ($0\farcs11 \times 0\farcs08$ PA 38° at 0.9 mm, $0\farcs12 \times 0\farcs10$ PA 65° at 9 mm). The beam is shown by the grey ellipse in the bottom-left corner in each panel. The x- and y-axes indicate the offset from the stellar position in the RA and DEC in arcseconds, i.e., north is up and west is right. The dashed lines mark the location of Clump 1 in each panel.

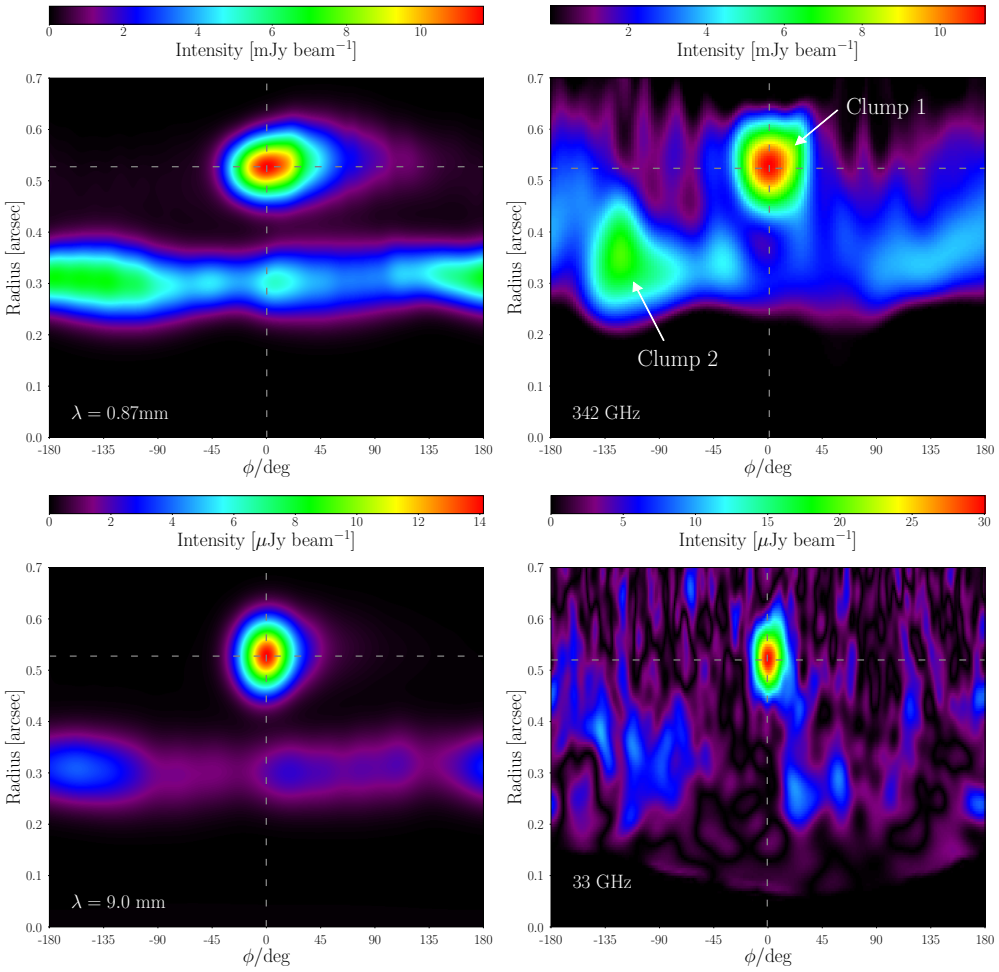

Figure 5.9: Same as Figure 5.8, but in polar coordinates. The y-axis displays orbital radius in arcseconds, the x-axis shows position angle relative to Clump 1, whose position is marked by dashed lines.

Predictions of thermal emission at different evolutionary stage

In Section 5.1, we describe how the evolution of the vortex at the outer edge of the inner planet's gap is relevant to obtain the lower levels of emission at 9 mm, relative to Clump 1. The effect of the decoupling and spread of the dust particles in the vortex decay process is more clearly seen if we compute the predicted thermal emission at both epochs displayed in Fig.5.2, which we display in Fig.5.15. The images were rotated so the position of the outer dust trap, which would correspond to Clump 1 in the MWC 758 disk, are approximately coincident in the flux maps. We observe how in the early stages of the disk, when the inner vortex is still active, most of the dust particles remain azimuthally concentrated at the vortex center, this results in a larger peak of emission from Clump 2 than Clump 1, which is the opposite trend observed in the ALMA and VLA images of MWC 758. Also, there is no clear evidence for the underlying ring of emission at the Clump 2 radial position. This is, again, inconsistent with the prominent ring of emission reported in ALMA observations of this object (Boehler et al., 2017; Dong et al., 2018) . Thus, the decaying inner vortex and subsequent loss of azimuthal trapping are crucial to reproduce accurately the ratio between the peak of emission between the two Clumps.

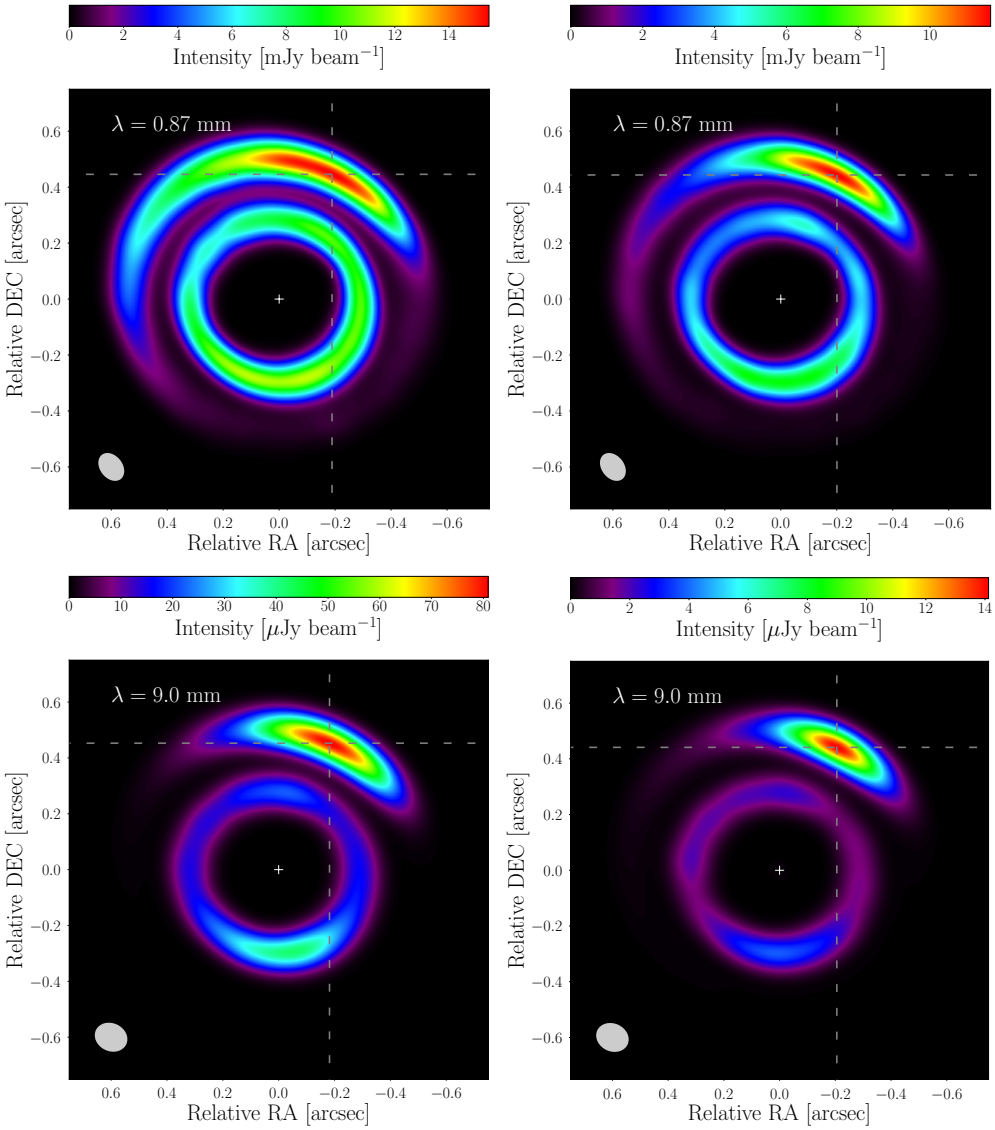

Figure 5.10: Comparison of the predicted continuum thermal emission at 0.9 and 9.0 mm for compact grains (left panels) and fluffy grains (right panels). The synthetic maps were convolved with the same beam as the observations from Casassus et al. (2018) ($0\farcs11 \times 0\farcs08$ PA 38° at 0.9 mm, $0\farcs12 \times 0\farcs10$ PA 65° at 9 mm). The beam is shown by the grey ellipse in the bottom-left corner in each panel. The x- and y-axes indicate the offset from the stellar position in the RA and DEC in arcseconds, i.e., north is up and west is right. The dashed lines mark the location of Clump 1 in each panel.

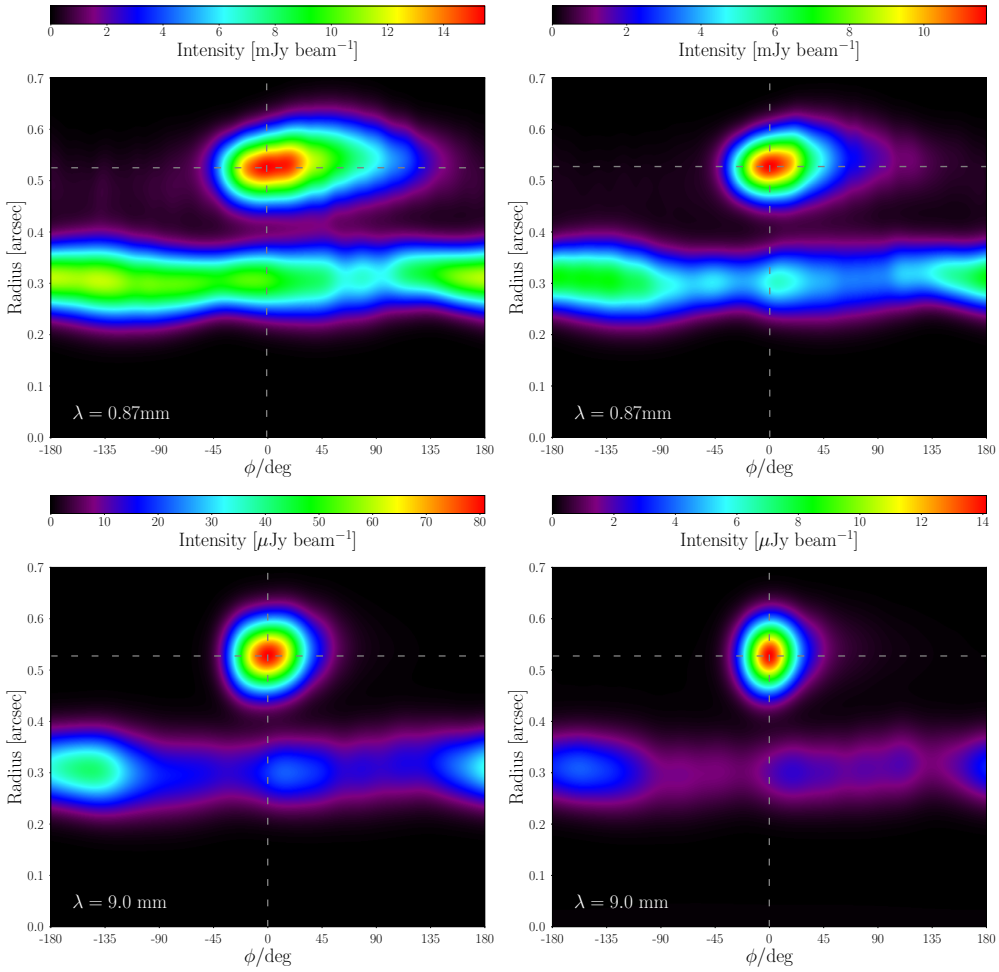

Figure 5.11: Same as Figure 5.10, but in polar coordinates. The y-axis displays orbital radius in arcseconds, the x-axis shows position angle relative to Clump 1, whose position is marked by dashed lines.

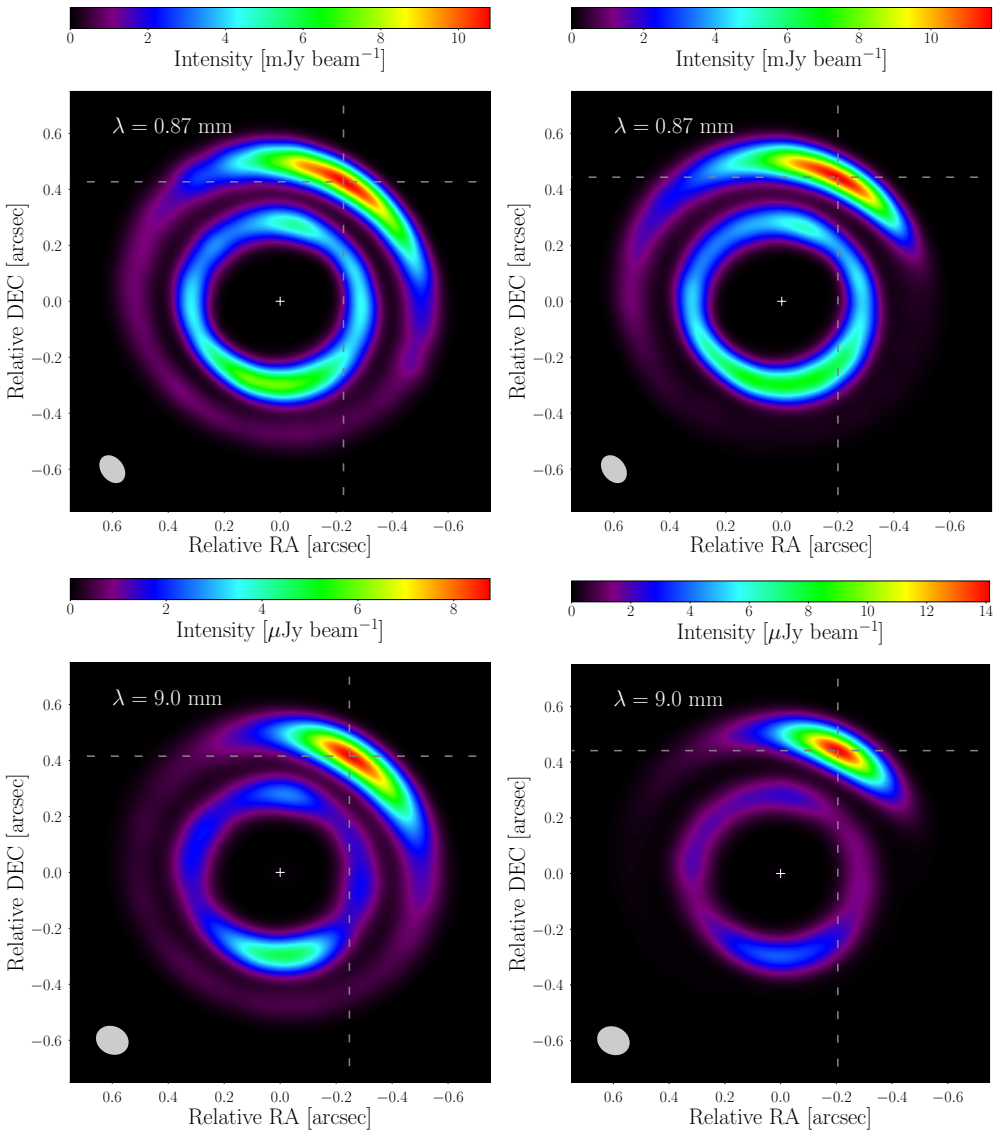

Figure 5.12: Comparison of the predicted continuum thermal emission at 0.9 and 9.0 mm for the fluffy grains model assuming a dust maximum size of 2 cm (left panels) and a dust maximum size of 1 cm (right panels). The synthetic maps were convolved with the same beam as the observations from Casassus et al. (2018) ($0\farcs11 \times 0\farcs08$ PA 38° at 0.9 mm, $0\farcs12 \times 0\farcs10$ PA 65° at 9 mm). The beam is shown by the grey ellipse in the bottom-left corner in each panel. The x- and y-axes indicate the offset from the stellar position in the RA and DEC in arcseconds, i.e., north is up and west is right. The dashed lines mark the location of Clump 1 in each panel.

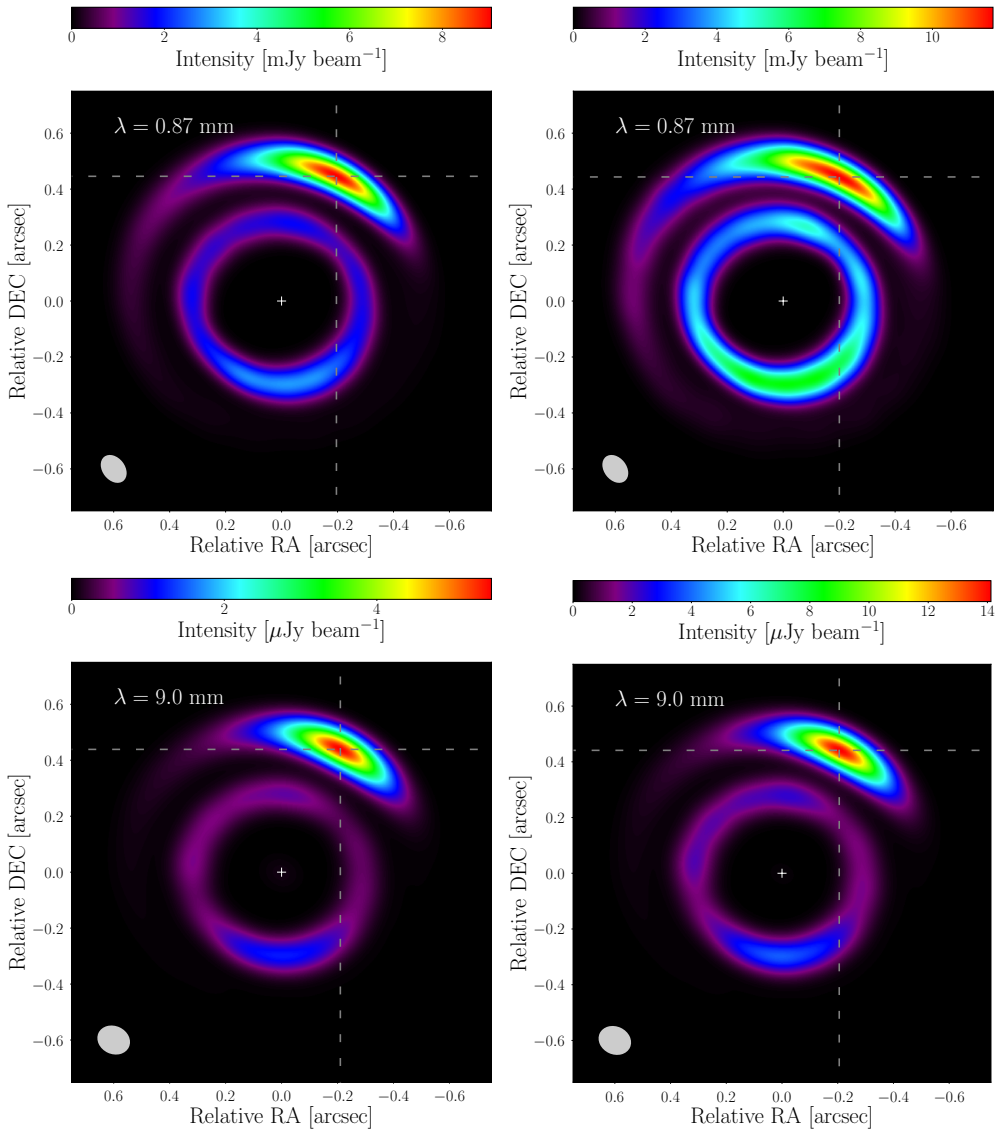

Figure 5.13: Comparison of the predicted continuum thermal emission at 0.9 and 9.0 mm for the porous grain model varying the dust-to-gas mass ratio from $\chi = 10^{-2}$ (left panels) to $\chi = 3 \times 10^{-2}$ (right panels). The other parameters that define the model are the same for both cases, dust slope of the size distribution of 3.0 and maximum dust size of 1 cm. The synthetic maps were convolved with the same beam as the observations from Casassus et al. (2018) ($0\farcs11 \times 0\farcs08$ PA 38° at 0.9 mm, $0\farcs12 \times 0\farcs10$ PA 65° at 9 mm). The beam is shown by the grey ellipse in the bottom-left corner in each panel. The x- and y-axes indicate the offset from the stellar position in the RA and DEC in arcseconds, i.e., north is up and west is right. The dashed lines mark the location of Clump 1 in each panel.

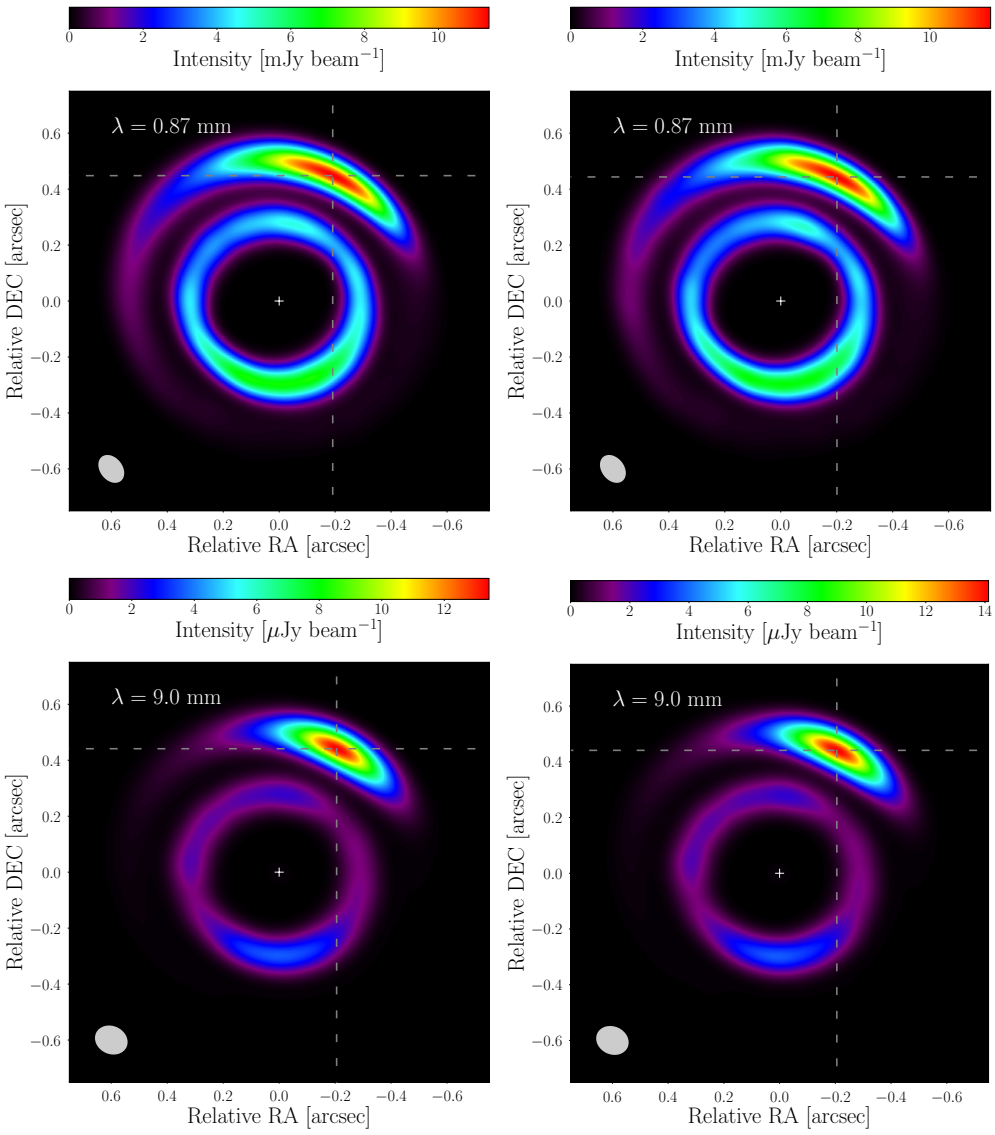

Figure 5.14: Comparison of the predicted continuum thermal emission at 0.9 and 9.0 mm for the porous grains model (dust internal density of $0.1\,\mathrm{g\,cm^{-3}}$) assuming different slopes for the dust size distribution, a value of -2.5 is set for the left panels, while a value of -3.0 is set for the right panels. Similar values for the dust mass and dust maximum size are set for both models. The synthetic maps were convolved with the same beam as the observations from Casassus et al. (2018) ($0\farcs11 \times 0\farcs08$ PA 38° at 0.9 mm, $0\farcs12 \times 0\farcs10$ PA 65° at 9 mm). The beam is shown by the grey ellipse in the bottom-left corner in each panel. The x- and y-axes indicate the offset from the stellar position in the RA and DEC in arcseconds, i.e., north is up and west is right. The dashed lines mark the location of Clump 1 in each panel.

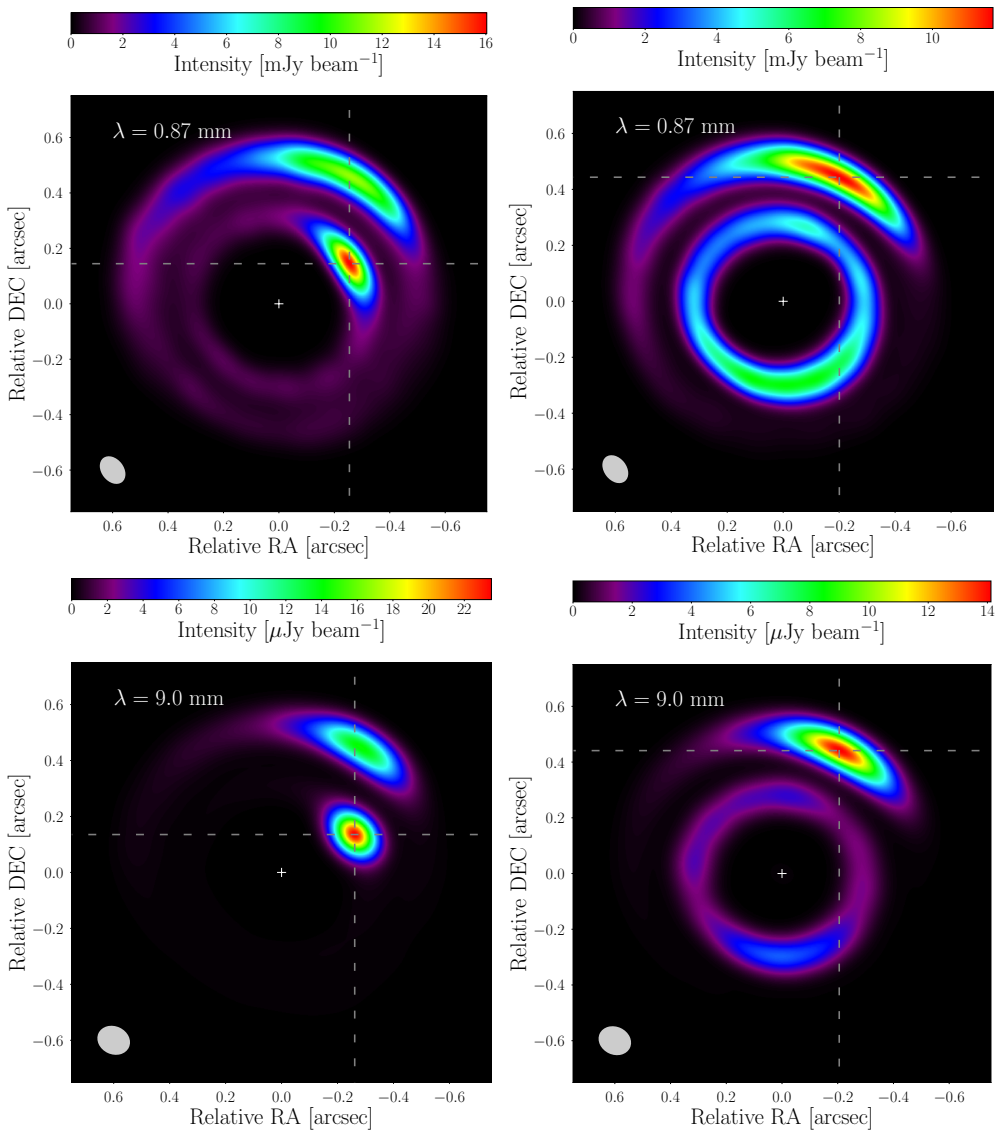

Figure 5.15: Comparison of the predicted continuum thermal emission at 0.9 and 9.0 mm for the porous grains model at two different stages of the simulation, at 600 orbits (left) and at 1323 orbits (right, same as left panels of Fig. 5.8). The synthetic maps were convolved with the same beam as the observations from Casassus et al. (2018) ($0\farcs11 \times 0\farcs08$ PA 38° at 0.9 mm, $0\farcs12 \times 0\farcs10$ PA 65° at 9 mm). The beam is shown by the grey ellipse in the bottom-left corner in each panel. The x- and y-axes indicate the offset from the stellar position in the RA and DEC in arcseconds, i.e., north is up and west is right. The dashed lines mark the location of the peak of emission in each panel.

5.1.3 Y-band polarized scattered light

A side-by-side comparison between our synthetic map of polarized scattered light with the Y-band ($\lambda \sim 1.04\,\mu$m) non-deprojected scattered light image of Benisty et al. (2015) is displayed in Fig. 5.16. Both images are scaled by r^2, with r the deprojected distance to the star. Also, the images are normalized to arbitrary units. To highlight the asymmetric structures in our synthetic map, a mask of $0\farcs2$ radius is applied (similar to the Dong et al. (2015) polarized scattered light predictions applied to the MWC 758 disk), and the scattering of the disk layers beyond ~ 65 au ($0\farcs43$) has been artificially reduced by decreasing the gas pressure scale height (H) beyond that location (see Section 4.2). This is the reason why we see no scattered light inside $0\farcs2$ and beyond $0\farcs43$ in radius, in our synthetic map, despite there being gas (and a priori small dust) at these locations. We rely on the fact that part of the scattered light reduction beyond ~ 65 au could arise from shadowing effects due to the spirals, as in a three-dimensional model the pressure scale height is highly increased at the spiral locations (see e.g. Dong, 2015a). The same dashed curves are superimposed in both panels to compare the morphology of the predicted and observed asymmetries, however, we stress that they are not fits to the observed spiral-like features, but are included as a visual reference to guide the eye. Overall, we see that our model predicts several spiral arms, but two are more prominent. This is expected as they have larger gas surface density relative to the other spirals, as observed in Fig. 5.1. Similarly to the gas surface density of the simulation (see Figs. 5.1 and 5.2), it is hard to disentangle what is triggering the spirals in the synthetic scattered light image. The spirals in scattered light trace the density waves that could be due to either the planets, the vortices, or a combination of both. Interestingly, we see that our synthetic map can reproduce both the location and the winding (traced by the pitch angle) of the observed spiral arm to the south-east accurately (see dashed curves denoted by S2 in Fig. 5.16). According to our model, this spiral arm would be the (primary) inner wake of the outer planet, which propagates from the outer planet's position. Our synthetic image also shows a second prominent spiral to the west, which corresponds to a secondary spiral density wave induced by the outer planet. This spiral is quite localized in our synthetic image, and we note that it nearly coincides with the bright concentric arc to the west of the SPHERE image (see the lower part of the dashed curves denoted by S1 in Fig. 5.16). Nonetheless, the other sub-structures in the observed asymmetry to the west (arc-shaped peak close to the position of Clump 1, concentric arc slightly inside of Clump 1) do not have a clear counterpart in our synthetic map.

We stress that a realistic energy equation and three dimensional effects, which are not taken into account in our hydrodynamical simulations, could strongly affect how the spiral arms would look like in the polarized scattered light images, in particular, the appearance of the secondary wake induced by the outer planet (Zhu et al., 2015; Fung and Dong, 2015; Dong and Fung, 2017). For this reason, we will not press the comparison between our synthetic polarized scattered light image and the observed image too far. It could be that the reproduction of the S2 spiral is coincidental.

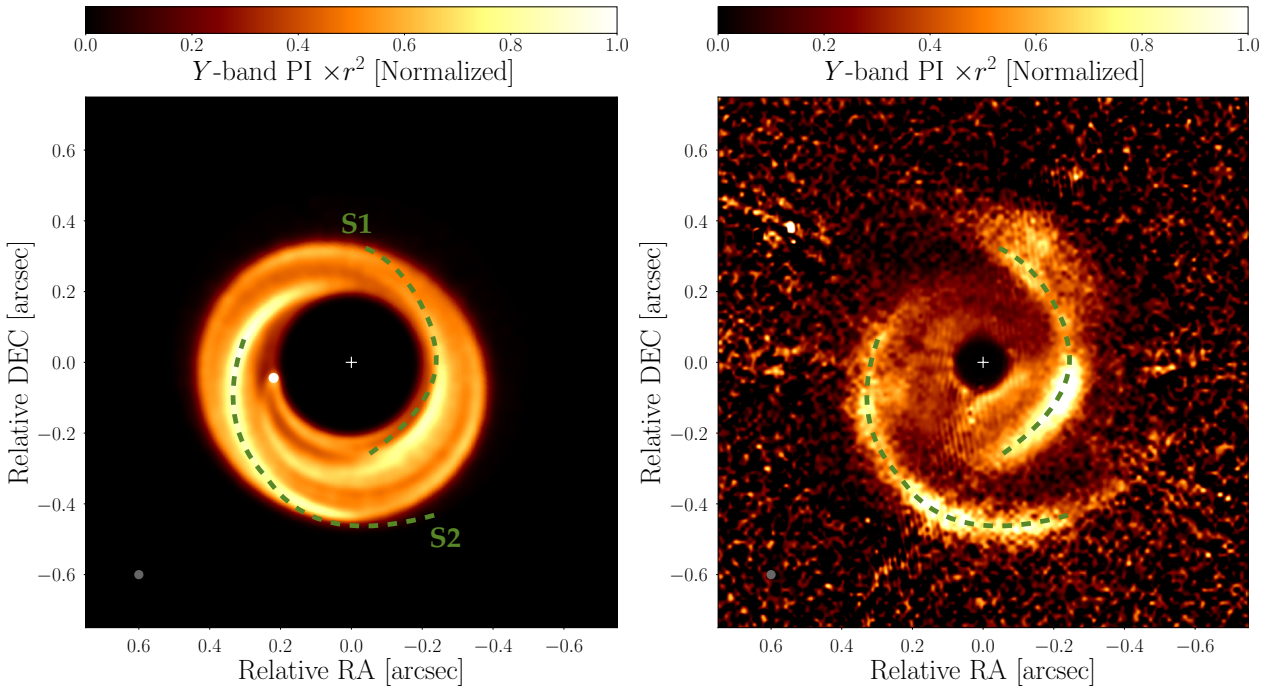

Figure 5.16: **Left panel**: Synthetic map of polarized scattered light at 1.04 μm ,scaled by r^2 (arbitrary units). To highlight the spirals structure, a mask of 0.″2 radius is applied, and the scattering of the disk parts beyond 0.″43 is artificially reduced (see text). The raw intensity map is convolved with a 0.″026 circular beam, shown by a grey circle in the bottom-left corner, which is similar to the resolution achieved in the Y band SPHERE observations of Benisty et al. (2015). The white circle marks the position of the inner planet. The outer planet is outside the image domain (at 0.″81, PA 292°). **Right panel**: Y band non-deprojected SPHERE image of Benisty et al. (2015), also scaled by r^2 and in arbitrary units. The dashed curves in both panels are used to compare the synthetic and observed asymmetries, but they are not fits to the observed spiral traces. As before, the x- and y-axes indicate the offset from the stellar position in RA and DEC in arcseconds (north is up and west is to the right). For comparison purposes, the range of the x- and y-axes is the same as in the thermal emission maps in Fig. 5.8.

In addition to the convolved synthetic predictions of Fig. 5.16, we display the raw Q_ϕ and U_ϕ maps in Fig. 5.17. Overlaid, as a reference, are the non-deprojected spiral traces of the three spiral arms presented in Reggiani et al. (2017). The S2 spiral arm, which is the L-band emission of the South-East spiral observed by Benisty et al. (2015); Grady et al. (2013) at Y and H band, respectively, matches the location and morphology of the planet driven spiral arm of the outer planet in our simulation. A clear difference in pitch angle and radial location is present between the S1 spiral arm trace and the North-East spiral arm in our predictions. But a direct comparison is not accurate as the H-band observations traces disk layers closer to the midplane, where the difference between the spiral location between H and Y-band is maximum at the North-East of the disk (see Dong et al., 2018). Also, we observe that the location of the beginning of the S3 spiral arm matches about the radial location of the inner planet in our simulation, the origin of the S3 spiral arm by a planet inner to the spiral is consistent with its decreasing pitch angle. However, this match could be coincidental (see Section 6.5). Finally, we observe that the U_ϕ map is about zero on average, consistent with the expected values for this Stokes vector (see Section 4.2).

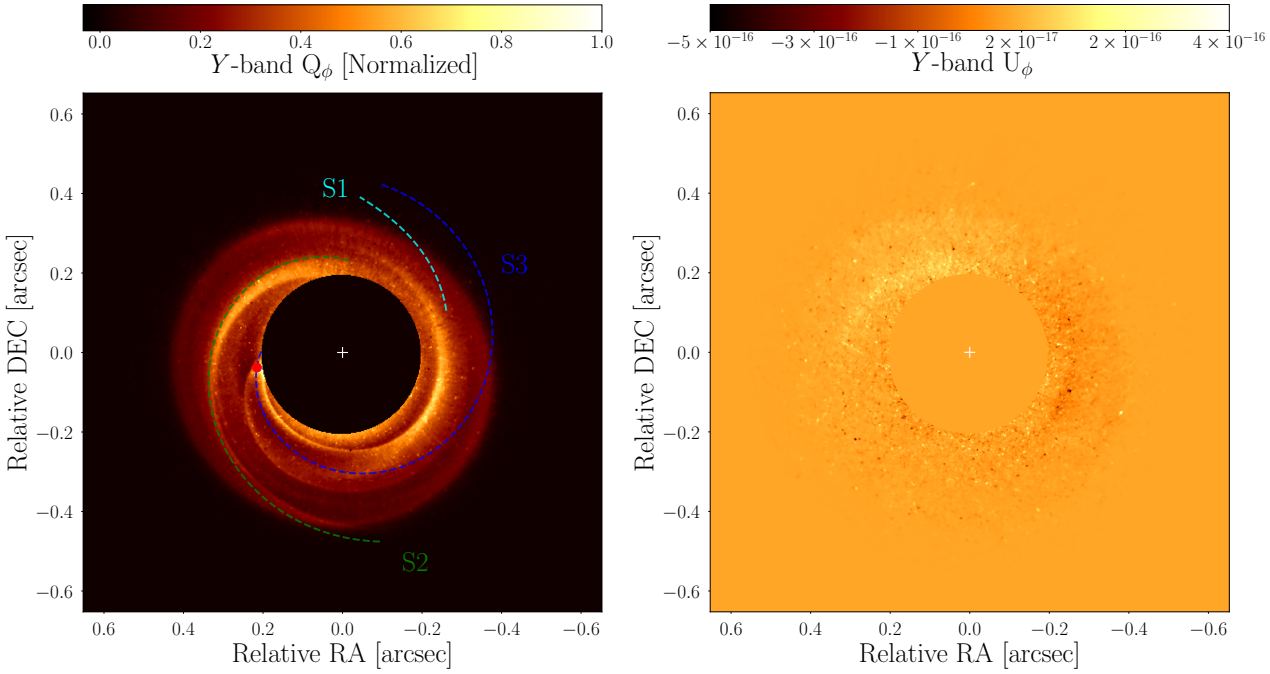

Figure 5.17: **Left panel**: Synthetic raw Q_ϕ image at 1.04 μm at full resolution, a mask of 0.″2 radius is applied, and the scattering of the disk parts beyond 0.″43 is artificially reduced (see text). Overlaid are the spiral traces presented for the L-band observations of Reggiani et al. (2017), where S1 and S2, in cyan and green, respectively, correspond to the North-West and South-East spirals previously observed in Y-band and H-band (Benisty et al., 2015; Grady et al., 2013). In blue is the third spiral revealed by Reggiani et al. (2017) observations. The red circle marks the position of the inner planet. The outer planet is outside the image domain (at 0.″81, PA 292°). **Right panel**: Synthetic raw U_ϕ image. As before, the x- and y-axes indicate the offset from the stellar position in RA and DEC in arcseconds (north is up and west is to the right). For comparison purposes, the range of the x- and y-axes is the same as in the thermal emission maps in Fig. 5.8.

Chapter 6

Discussion

6.1 Importance of gas self-gravity

The simulations carried out in this study include gas self-gravity, which might seem unnecessary since the (azimuthally averaged) Toomre Q-parameter remains much larger than unity in our disk model. Q reaches a local minimum of about 30 at the inner edge of the outer planet's gap, near 80 au from the star (Clump 1's location). However, as shown in previous studies (e.g. Lin and Papaloizou, 2011; Lin, 2012; Lovelace and Hohlfeld, 2013; Zhu and Baruteau, 2016; Regály et al., 2017), gas self-gravity significantly wakens large-scale RWI vortices (with azimuthal wavenumber $m = 1$) when the product of Q and h becomes smaller than $\sim \pi/2$ at the vortex location. Given our uniform aspect ratio $h = 0.088$, vortices become significantly impacted by self-gravity for $Q \lesssim 18$. Therefore, if we had taken a larger initial surface density for the gas in our simulations, the outer vortex, formed at ~ 80 au would have been weaker and would have therefore decayed earlier. Said differently, with gas self-gravity included, a rather low surface density for the gas at the vortex location is necessary for the dust trap to match the high concentration of dust grains inside the vortex core, crucial to reproduce the compactness of Clump 1 seen in the ALMA and VLA observations. This is a consequence of the vortex efficiently trapping dust particles for a longer period of time, thus, reaching a higher level of concentration. This rather low surface density is consistent with that estimated by (Boehler et al., 2017) based on ALMA Band 7 observations of ^{12}CO and C^{18}O.

6.2 Vortex decay

In this work, we present a scenario where the asymmetric ring and the compact crescent observed in the ALMA Band 7 and VLA continuum data of the MWC 758 disk are due to planet-induced vortices. To explain the low and diffuse signal obtained with VLA at the location of the asymmetric ring (Clump's radial location), we propose that this ring could result from a decaying vortex. In our simulations, vortex decay is mediated by viscous diffusion ($\alpha = 10^{-4}$), and the lifetime of the vortex that gives rise to the asymmetric ring, about a thousand orbital timescales, is consistent with previous 2D simulations of planet-induced vortices for similar disk parameters and masses (see e.g. Fu et al., 2014a). A smaller turbulent viscosity would increase the lifetime of the vortices in our simulations. However, as we have checked with preliminary simulations, it would also cause a higher concentration of the large dust particles in the vortices, and would, therefore, increase the compactness of the (sub)mm emission at both dust traps in a way that is not consistent with neither the ALMA nor the VLA observations. For example, in Fig. 5.4 we plot a comparison of a simulation with an alpha turbulent viscosity one order of magnitude lower ($\alpha = 10^{-5}$) at 1000 orbits of the inner planet. From these panels is clear that for the lower viscosity simulation the inner dust trap is still active while in the $\alpha = 10^{-4}$ simulation the inner dust trap is already decaying. Also, the dust is highly concentrated at the vortex center for the low viscosity case, and it is still efficiently trapping large particles, which would results in a vortex aspect ratio too small compared to the observed value. A good agreement for the low viscosity case and the simulation might be possible, however, for a later stage in the simulation. Furthermore, several factors affect the growth and decay timescales of planet-induced vortices in 2D viscous disk models, including the timescale for planetary growth (Hammer et al., 2017), which is taken to be the same for both planets in our model, a non-isothermal energy equation (Les and Lin, 2015), gas self-gravity (Lin and Papaloizou, 2011), or dust feedback on the gas (Fu et al., 2014b).

The level of viscosity adopted in our simulations is meant to model the effects of MHD turbulence in the outer regions of a protoplanetary disk, where non-ideal MHD effects, in particular, ambipolar diffusion should play an important role. Modeling turbulence as a diffusion process is uncertain when the typical length scale of interest (here, that of the gas vortex) is of the order of the pressure scale height. Zhu et al. (2014) have investigated the growth of and dust trapping in planet-induced vortices via global 3D MHD simulations. One of their simulations including ambipolar diffusion shows that the vortex formed at the outer edge of the gap carved by a 9 Jupiter-mass planet decays in about 1000 orbital timescales, with a similar lifetime found in a 2D hydrodynamical simulation using an equivalent turbulent viscosity. This result gives credit to the vortex's decay timescale obtained in 2D viscous disk simulations. Decaying vortices have been also been reported at the edges of the active and dead zone of a protoplanetary disk (Flock et al., 2015). However, in their simulations, the vortices reform again and decay in a certain cycle. In our simulations, the vortices do not reform, at least until 1500 orbital periods of the inner planet (at 33 au).

One last thing that the reader should bear in mind is that the vortex's decay scenario that we propose in this study may not be a transient phenomenon. Given our planet's mass and disk parameters, it takes about a thousand planet orbits before the gas vortex at the outer edge of the inner planet's gap has fully decayed ($\sim 0.15\,\mathrm{Myr}$). This timescale might look short in comparison to the estimated age of the disk-bearing stars, but it also takes time to grow the planet(s) in the first place, and it is not clear how long it should be expected to form a Jupiter-mass planet at 33 au around an A5-type star. And when the gas vortex is gone, it still takes a fair amount of time (a few more hundred orbits, typically) for dust particles to lose memory of their azimuthal trapping. Said differently, despite the gas vortex being already gone, dust particles keep forming a lopsided ring of emission over a few hundred planet orbits. Moreover, these results could imply the non-detection of vortices in the gas kinematics in a protoplanetary disk. Despite this, it could still be a dust trap in the dust distribution of a disk, the former dust trapping vortex may be already weakened by disk's self-gravity, which puts strong difficulties in its detection via gas observations.

6.3 Impact of dust parameters

We discuss in this section how the size distribution, total mass and internal density of the dust particles affect our results of simulations. Their impact on the synthetic continuum emission maps is also addressed.

6.3.1 Dust's size distribution

Throughout this work, we assume that the size of the dust particles follows a power-law distribution, with thus three parameters: the minimum and maximum sizes, and the power-law exponent. We recall that the results presented in Section 5.1.2 are for a size distribution $n(s) \propto s^{-3}$ for particles sizes s between $10\,\mu$m and 1 cm. Decreasing the minimum size is found to have no impact in our synthetic maps in the (sub)mm, as particles smaller than $10\,\mu$m have a very small contribution to the thermal emission at both 0.9 mm and 9 mm.

The maximum size assumed for the dust particles has, however, a much stronger impact on the results. To see why this is the case, we display in the lower right panel of Fig.5.4 the dust's spatial distribution at 1323 orbits overlaid on the gas perturbed vortensity, just like in the top-right panel of Fig. 5.2, except that we now show the location of dust particles up to 10 cm in size (instead of 1 cm). Particles larger than about 1.5 cm are not trapped in the vortex at ~ 80 au but shifted radially inwards by about 5 to 10 au at this time in the simulation. This radial shift stems from the interaction between the large dust particles and the inner density wake produced by the outer planet. Since this wake carries negative fluxes of energy and angular momentum, it pushes dust particles inwards each time they cross the wake. The deflection caused by the wake is clearly visible in the lower right panel of Fig.5.4 at $r \sim 80$ au and $\varphi \sim -2.5$ rad for $s \sim 2$ cm particles. It shows that, at the vortex's orbital radius, the radial deflection caused by the planet wake is larger than the radial drift back towards the vortex for dust particles larger than about 1 cm, which have a Stokes number $\gtrsim 0.1$. These particles thus find an equilibrium location interior to the vortex, where they form a nearly axisymmetric ring.

Furthermore, we have explored different values for the maximum dust size set for the radiative transfer calculations, to fit the current data of MWC 758. To illustrate how this parameter impacts our results, in Fig. 5.12 we show a side by side comparison of a model assuming a maximum size for the dust distribution of 2 cm and 1 cm (our best match for MWC 758), on the left and right panels, respectively. The aforementioned large spread of $\gtrsim$ cm-sized dust particles makes significant changes in our results of the synthetic maps if we chose a larger maximum for the dust's size distribution. We observe an increase of the clump's azimuthal extension in the synthetic maps, as a result of the thermal emission of these cm-sized particles. Therefore, this ring of $\gtrsim$ cm-sized dust particles would make the (sub)mm emission near Clump 1 much more extended in the azimuthal direction than predicted in Fig. 5.8 for the same total dust mass, which would be incompatible with the compactness of Clump 1 as currently observed by ALMA and especially the VLA (see Fig. 5.12). This could have interesting implications for dust growth in the MWC 758 disk, as our model suggests inefficient growth beyond cm sizes around the location of Clump 1, which we speculate might

be due to bouncing and/or fragmentation barriers.

Different is the case for the slope of the dust's size distribution which has, overall, a mild impact on the predicted (sub)mm emission for Clump 1 and Clump 2. A shallower dust size distribution (smaller p) increases the peak at a longer wavelength and increments the compactness of the clumps at 0.9 mm as well as at 9 mm. We explore that a different choice of p between -3.5 and -2.5 has a negligible impact on the predictions. To illustrate the effect of the slope of the dust's size distribution, in Fig. 5.14 we display the comparison between our best model (on the right-hand side) and a model with a dust-slope of the size distribution of -2.5 (at the left), for the same maximum limit (1 cm) and dust mass ($\chi = 3 \times 10^{-2}$). In Fig. 5.14 we observe that the impact on the peak fluxes at the position of Clump 1 is almost insignificant (approximately 3%).

6.3.2 Dust's total mass

The total dust mass of the model impacts on the peak fluxes at the position of the Clumps and the level of optical depth. For the dust mass of $2.4 \times 10^{-4}\,\mathrm{M}_\star$ between $\sim$ 40 au and $\sim$ 85 au adopted in Chapter 4, the peak optical depth at 0.9 mm is $\sim$ 25 for Clump 1 and $\sim$ 4 for Clump 2 (see last paragaph of Section 5.1.2). Increasing the total dust mass would result in an even larger optical depth for Clump 1, and thus a more extended emission which would be incompatible with the observed compactness of Clump 1 at 0.9 mm. Decreasing the total dust mass would reduce the peak intensity of Clump 2 faster than for Clump 1 at 0.9 mm, thereby increasing the peak intensity ratio between Clump 1 and Clump 2 at that wavelength, as is shown in Fig. 5.13, where we display a side-by-side comparison of our best model (on the right-hand side) which corresponds to a dust-to-gas mass ratio (χ) of 3×10^{-2} and a model with $\chi = 10^{-2}$. For instance, for a dust mass of $2.4 \times 10^{-5}\,\mathrm{M}_\star$ ($\sim 12 M_\oplus$), we find a peak intensity ratio by a factor 3 to 4, while the observed value is 1.5 ± 0.1. At 9 mm, the emission is only marginally optically thick for Clump 1, and decreasing the dust mass simply decreases the overall flux level uniformly. In particular, decreasing the dust mass would result in an even larger discrepancy between the predicted peak intensity for Clump 1 at 9 mm and that observed with the VLA.

6.3.3 Dust's internal density

The particles internal density adopted throughout this study, $\rho_{int} = 0.1\,\mathrm{g\,cm^{-3}}$, may seem a little surprising as simulations and/or radiative transfer calculations usually model dust as compact grains with an internal density of a few $\mathrm{g\,cm^{-3}}$. Still, our best match with the observed morphology and properties of the disk's thermal emission of MWC 758 is obtained assuming porous dust particles. Figures 5.10 and 5.11 demonstrate the impact of the dust's internal density on the synthetic predictions, in which we display the predictions obtained at 0.9 mm (ALMA) and 9.0 mm (VLA) for the same model and evolutionary stage in the simulations, but the internal density of the dust grains are set to $1\,\mathrm{g\,cm^{-3}}$ (compact) and $\rho_{int} = 0.1\,\mathrm{g\,cm^{-3}}$ (porous), displayed in the left and right panels, respectively. The only difference between the setups of the radiative transfer calculations, besides the dust internal density, is the maximum size set in the dust size distribution (1 cm and 1 mm for porous and compact grains, respectively). The synthetic maps show, overall, similar morphology for porous and compact grains cases, however, significant differences are observed in the predicted peak of emission. The predicted ALMA peak flux at Clump 1 position for the compact case is 13.6 mJy which is in not far from the observed value (and that predicted in the porous case), but for VLA wavelength is 70.6 μJy, which is about ~ 2.4 the observed peak flux in the VLA observation. Moreover, the ratio between the peak of intensities of Clump 1 and Clump 2 does not match the observed value. These discrepancies are the main reasons why we have adopted $\rho_{int} = 0.1\,\mathrm{g\,cm^{-3}}$ throughout this study.

It is necessary to set different maximum dust size for the compact and porous cases in order to obtain similar morphologies of the dust traps in the synthetic maps. This is because the particles dynamics primarily[1] set by the Stokes number, which is set by the product of particles size and internal density (see Eq. 3.8). For example, if we look at Fig. 5.11 it is clear that the azimuthal FWHM of Clump 1 assuming compact grains is larger than in the porous case. This is a result of a different dynamical evolution of the particles in the gas, in which the compact particles, in the range of sizes considered, are more spreadly distributed azimuthally inside the vortex than the porous ones. This result also supports the chose of porous particles for our study, as the azimuthal width of Clump 1 is consistent with the obtained for the porous case (see Section 5.1.2). In addition, for $\rho_{int} = 1\,\mathrm{g\,cm^{-3}}$, particles larger than about 1 mm are shifted interior to the vortex located at $\sim 80\,\mathrm{au}$ because of the inner wake of the outer planet, just like the particles larger than about 1 cm in our simulation with $\rho_{int} = 0.1\,\mathrm{g\,cm^{-3}}$, as shown in Section 6.3.1. Therefore, grain's internal density not only affects the emergent emission in the flux maps but also the dynamical evolution of the dust particles in the gas.

After an exploration of the parameter space in the radiative transfer model, we were unable to find a good agreement between the compact case and the observations. We stress, however, that our results cannot rule out that the dust in the MWC 758 disk could be compact, given the large uncertainties in the dust opacities (at either internal density). It would be interesting to explore the possibility of even smaller internal densities (see e.g. Kataoka et al., 2013).

[1] We write that the particles dynamics is primarily set by the Stokes number because gas self-gravity also affects the dynamics, especially when the Stokes number exceeds about 0.1 (Baruteau and Zhu, 2016).

6.4 On the location and mass of the possible planets in the MWC 758 disk

Reggiani et al. (2017) have recently reported the detection of a point-like source at about 20 au from MWC 758. Assuming this source is a planet candidate, we have investigated under which circumstances it could produce the asymmetric ring at 0.9 mm passing by Clump 2 at ~ 47 au. With our disk model, we find that the mass of the planet candidate should be close to $30\,\mathrm{M_{Jup}}$ so that the pressure maximum located at the outer edge of its gap matches the orbital radius of Clump 2 (see Fig. 5.6). While such a massive companion could account for the large (sub)mm cavity in the disk, it would most likely open a very large gap or even a cavity in the gas which would be devoid of the smallest dust grains. But such a large gap or cavity is not seen in scattered light images of MWC 758, making this scenario less likely. Furthermore, Huélamo et al. (2018) searched for H_α emission and found no detection at the location of the point source reported in Reggiani et al. (2017), which results in an upper mass limit of $5M_{Jup}$ for this planet candidate. If the planet candidate at about ~ 20 au were present in addition to the planet at ~ 33 au that we propose as responsible for Clump 2, then both planets would be close to their 2 : 1 mean-motion resonance and likely carving a common gap in the gas, which, again, lacks observational support.

With a moderately massive inner planet in the (sub)mm cavity, the outer planet is required in our simulations to explain the multiple spiral arms which are observed in polarized scattered light (see Section 5.1.3). By adopting for the outer planet's mass the upper mass limit obtained by Reggiani et al. (2017), we find that the outer planet should be located at about 132 au to produce the dust trap at the orbital distance of Clump 1 (~ 80 au). However, preliminary simulations have shown that a similar dust trap could be achieved by adopting a more massive companion at a larger orbital distance like, for instance, an extreme case studied is a $0.1\,\mathrm{M_\odot}$ substellar companion at ~ 300 au from the central star, as shown in Fig. 5.3. For this case the disk is tidally truncated at ~ 100 au, also triggering the Rossby wave instability at the truncation radius, leading the formation of a vortex at about 80 au. Such substellar companion related to the formation of symmetric spiral arms has been observed in the HD 100453 protoplanetary disk (Wagner et al., 2015; Dong et al., 2016; Benisty et al., 2017). A companion with a mass larger than $\sim 5\,\mathrm{M_{Jup}}$ would also trigger stronger spiral waves, and result in spiral arms with higher contrast in scattered light, and larger pitch angles (see e.g. Fung and Dong, 2015; Dong, 2015b). Nevertheless, such an extreme case is discarded given the near infrared observation limit detections (Benisty et al., 2015; Reggiani et al., 2017). But we can not rule out on small scale a more massive planet at a slightly larger radius. The reason is that the correlation between the planet's mass and radius, with the position of the outer vortex at ~ 80 au is degenerate. For the same reason, we can not discard a lower mass planet (but massive enough to trigger multiple density waves) locate at a smaller radius (but external to the spirals and Clump 1), for example, a planet located at 100 au proposed by Dong et al. (2018); Bae and Zhu (2017).

Despite the fact that the massive outer planet adopted in our scenario has not been detected in the recent Keck L' band observations of Reggiani et al. (2017), the detection limit was computed assuming a hot start evolutionary model. Assuming a cold start model can dramatically increase the mass detection limit for the same contrast (Spiegel and Burrows,

2012). The detection of the outer planet in high-contrast imaging observations could also be hampered by contamination due to extended disk emission, making difficult the identification of a point source (Follette et al., 2017). Finally, if the planet has a circumplanetary disk or envelope, the material surrounding the planet could affect gas accretion on to the planet and consequently the planet's luminosity (Szulágyi et al., 2014), hindering its direct observation. A direct detection will be possible with future high spatial resolution ALMA observations of molecular lines, where the strong impact that a massive planet could have on the observed kinematics of the gas can be identified (Perez et al., 2015; Pérez et al., 2018). Kinematic evidence for a massive planet in the HD 163296 disk based on ^{12}CO ALMA observations has been recently reported in Pinte et al. (2018); Teague et al. (2018).

Based on multi-epoch near-IR observations of the MWC 758 disk, Ren et al. (2018) have estimated the rotation (or pattern) speed of the two most prominent spirals. Assuming that these spirals are the inner wakes of a massive companion, they find, based on the spirals pattern speed, that the companion's best fit orbital distance would be at about 90 au. This is very close to the location of Clump 1 in the (sub)mm images ($\sim$ 80 au), and it seems unlikely that a massive companion at about 90 au could form a dust-trapping vortex at the location of Clump 1. However, we stress that the uncertainty in the estimation of the pattern speed is large, as highlighted in Ren et al. (2018), and that there is actually no constraint on the upper distance of the putative companion. The 3σ lower limit on the pattern speed goes to 0 indeed (that is, no rotation; Ren et al., 2018), which would correspond to a companion at infinite distance. The orbital distance that we assume for the outermost planet in our model (132 au) is therefore entirely consistent with the current measurement of the spirals pattern speed.

6.5 On the origin of the third spiral arm and multiple concentric rings

A proposed mechanism to explain the three-spiral arm structure revealed in near-IR observations of MWC 758 (Reggiani et al., 2017), one plus the two previously observed (Grady et al., 2013; Benisty et al., 2015), corresponds to constructive interferences between planet-driven spiral wave modes (Bae and Zhu, 2018). The formation of multiple spiral arms by one planet depends on the planet mass and disk physical properties. In the case in which an external companion at $\sim$ 100 au excites two of the three spiral arms it should be more massive than two thermal mass (mass at which the planet Hill radius is comparable to the disk scale height). But in the case in which the planet is responsible for the three of the spiral arms it should have a mass lower than three thermal masses, leaving a possible range for the outer planet between 2.7 and 5 M_{Jup} (Bae and Zhu, 2017). This is consistent with the mass of our proposed candidate.

Interestingly, the inner part of the third spiral arm observed by Reggiani et al. (2017, S3) matches about the location of the beginning of the primary spiral arm produced by the inner planet in our simulation, exterior to its orbit. This origin for the third spiral arm is not discarded and could explain the decreasing pitch angle as a function of the radius of

the S3 spiral arm (Bae and Zhu, 2017). Moreover, three-dimensional hydro simulations have shown that the planet-driven spirals interior to the planet have significant vertical motion compared with the spiral exterior to the planet (Zhu et al., 2015). Thus, if S3 is the outer spiral of a planet inside the cavity its pressure scale height should not increase significantly along the arm. While the arms that are driven by the outer massive planet have strong vertical motion, and consequently, larger dust's pressure scale height. This difference in their vertical structure could explain the non-detection of S3 in Y-band. The reason is that Y-band observations traces upper layers of the disk, while L-band observations traces lower disk's regions (Bae and Zhu, 2017; Reggiani et al., 2017). This result is consistent with the idea that large pressure scale height at the spiral arm location is crucial for its observability at short wavelengths (Juhász et al., 2015; Zhu et al., 2015; Dong, 2015a,b). The only case that is discarded is that an inner planet inner to the spiral structure produces all three spirals. Future measurements of the pattern speed of the three spiral arms will tell us if the spirals are produced by one or more planets. Which would be the case if S3 has a lower pattern speed than the two most prominent (S1 and S2). The spiral structure could also be produced by interference between the spiral waves produced by different planets, for example for our model the structure could result as the interaction between the spiral arms of the inner planet exterior to its orbit and spirals that are driven by the outer planet interior to its orbit, however, this interaction could be very complex and further investigation is needed.

The ALMA observations presented in Dong et al. (2018) revealed that MWC 758 has a triple ring structure with an inner ring radially colocated with the inner clump (Clump 2), an outer ring radially colocated with the outer clump (Clump 1) and a less prominent middle ring in between. Despite the fact that the three-ring structure is not present in our results, this structure could still be consistent with a planetary origin and with our model. A proposed origin for the multiple concentric rings is the same beforesaid for the origin of the third spiral arm, i.e. multiple spiral arms produced by a planet (Bae et al., 2017). Each spiral arm has a location where it steepens into a shock, they deposit angular momentum opening a gap in the disk. This is well known for primary arms directly attached to the planet. However, recent high-resolution hydrodynamical simulations have shown that one planet can trigger secondary and tertiary arms that can also open gaps. The gaps produced by secondary/tertiary spiral arms are shallower than the produced by the primary arms, consistent with the previously non-detection of the third ring. A second possible origin for the triple-ring structure of MWC 758, similar to the one previously described, is that the vortex that develops at the planet gap's edges excites density waves (Zhu et al., 2014). The waves produced by the vortex can steepen to shocks leading to the formation of additional sets of rings in the gas density (Bae et al., 2017). Waves produced by the vortices are seen in our simulations however, lower turbulent viscosity might be necessary for these density waves to make a substantial effect in the global structure of the disk. Moreover, higher resolution simulations are needed to resolve the spiral shock at all radius. Thus, no gap associated with under-resolved spiral shocks are formed (Bae et al., 2017; Bae and Zhu, 2017).

Chapter 7

Conclusion

In this work, we have studied a scenario for the origin of asymmetric structures in protoplanetary disks via planet-disk interactions. Specifically, we studied planet-induced dust traps as an explanation for azimuthal concentrations of dust thermal emission. We applied a dedicated study to the MWC 758 protoplanetary disk to unveil if its non-axis symmetric structures could be due the presence of non-detected planets.

We carried out 2D global hydrodynamical simulations including both gas and dust of a self-gravitating circumstellar disk under the influence of two giant planets. The results of our simulations, which were post-processed with 3D radiative transfer calculations, support a scenario where the asymmetries observed in the (sub)mm and near-IR scattered light of the transition disk MWC 758 could be due to the presence of two massive planets molding the global structure of the disk.

In this scenario, our model suggests the presence of a $5\,\mathrm{M_{Jup}}$ planet at 132 au and a $1\,\mathrm{M_{Jup}}$ planet at 33 au. The outer more massive planet triggers several spiral arms, of which two can reasonably account for the brightest spiral or arcs seen in Y-band polarized scattered light. It also forms a vortex at the inner edge of its gap (at ~ 80 au), where the dust its trapped and concentrated, the thermal emission from the dust trap reproduces quite well the compact crescent-shaped structure seen at $\sim 0\farcs52$ in the ALMA and VLA observations (Clump 1), if assuming moderately porous dust particles, with an internal density of $0.1\,\mathrm{g\,cm^{-3}}$, up to a centimetre in size. Because it is less massive the inner planet produces dim spiral arms in scattered light, and it forms a vortex at the outer edge of its gap (at ~ 47 au) which decays on account of the disk's turbulent viscosity. This decay can explain why the asymmetric emission ring seen with ALMA at $\sim 0\farcs32$ (Clump 2) has a weak counterpart in the VLA observations presented in Casassus et al. (2018). This scenario of a decaying vortex has been recently proposed by Fuente et al. (2017) to explain multi-wavelength NOEMA observations of the lopsided emission ring in the AB Aurigae transition disk.

Given our positive results on the reproduction of the observed features for the MWC 758 disk, we confirm that this disk is an excellent target for future dedicated studies of dust trapping via vortices, and the interaction with planets. Our study proposes the outermost giant planet as the link between the grand-design spirals in the NIR and the outermost dust

trap observed in the (sub)mm for this disk. Further studies on the relationship between the morphology of the planet-induced dust traps, and the planet(s) physical properties and orbital parameters could open a window on the indirect detection of companions in transition disks, given the difficulties for the direct detection of forming planets with the current facilities and instruments. Moreover, the information obtained from the study of the effects of planets on its surrounding material could help us to build a better strategy to accomplish its direct detection.

Finally, we point out the striking similarities between the transition disk around MWC 758, HD 135344B (also known as SAO 206462, van der Marel et al., 2016a), and V1247 Orionis (Kraus et al., 2017). Similarly to MWC 758, HD 135344B and V1247 Ori have moderately asymmetric emission ring surrounded by a crescent-shaped structure in ALMA Band 7 continuum observations. Both disks also have at least one spiral arm seen in polarized scattered light (Garufi et al., 2013; Ohta et al., 2016). Therefore, it is tempting to suggest that the asymmetries observed in the disks around HD 135344B and V1247 Ori could also result from the presence of at least two massive planets, and subsequent dust trapping by a pressure maxima, just like in the proposed scenario for the MWC 758 disk presented in this work.

Regarding the dedicated simulations to MWC 758, further physical effects need to be included to explain the full picture of the complex structures observed. We stress the inclusion of more realistic treatment of the temperature of the disk and turbulent transport of angular momentum, the effects of dust evolution (dust growth, fragmentation, and settling), dust feedback and three-dimensional effects. And despite the low mass reported for this disk, we highlight the importance of disk self-gravity in the evolution of the dust traps produced by vortices. High-resolution observations in the (sub)mm could also be crucial to understanding the kinematics of the disk, of which we lack high spectral and spatial resolution information. These observations could possibly reveal the effects of planets and vortices in the gas dynamics of this disk.

Chapter 8

Bibliography

F. C. Adams and F. H. Shu. Infrared spectra of rotating protostars. , 308:836–853, September 1986. doi: 10.1086/164555.

R. D. Alexander and P. J. Armitage. Dust dynamics during protoplanetary disc clearing. , 375:500–512, February 2007. doi: 10.1111/j.1365-2966.2006.11341.x.

S. M. Andrews, D. J. Wilner, C. Espaillat, A. M. Hughes, C. P. Dullemond, M. K. McClure, C. Qi, and J. M. Brown. Resolved Images of Large Cavities in Protoplanetary Transition Disks. , 732:42, May 2011. doi: 10.1088/0004-637X/732/1/42.

P. J. Armitage. Physical processes in protoplanetary disks. *ArXiv e-prints*, September 2015.

S. Ataiee, P. Pinilla, A. Zsom, C. P. Dullemond, C. Dominik, and J. Ghanbari. Asymmetric transition disks: Vorticity or eccentricity? , 553:L3, May 2013. doi: 10.1051/0004-6361/201321125.

S. Ataiee, C. Baruteau, Y. Alibert, and W. Benz. How much does turbulence change the pebble isolation mass for planet formation? *ArXiv e-prints*, April 2018.

H. Avenhaus, S. P. Quanz, M. R. Meyer, S. D. Brittain, J. S. Carr, and J. R. Najita. HD100546 Multi-epoch Scattered Light Observations. , 790:56, July 2014. doi: 10.1088/0004-637X/790/1/56.

H. Avenhaus, S. P. Quanz, H. M. Schmid, C. Dominik, T. Stolker, C. Ginski, J. de Boer, J. Szulágyi, A. Garufi, A. Zurlo, J. Hagelberg, M. Benisty, T. Henning, F. Ménard, M. R. Meyer, A. Baruffolo, A. Bazzon, J. L. Beuzit, A. Costille, K. Dohlen, J. H. Girard, D. Gisler, M. Kasper, D. Mouillet, J. Pragt, R. Roelfsema, B. Salasnich, and J.-F. Sauvage. Exploring Dust around HD 142527 down to 0.025 (4 au) Using SPHERE/ZIMPOL. , 154:33, July 2017. doi: 10.3847/1538-3881/aa7560.

J. Bae and Z. Zhu. Planet-driven spiral arms in protoplanetary disks: II. Implications. *ArXiv e-prints*, November 2017.

J. Bae and Z. Zhu. Planet-driven Spiral Arms in Protoplanetary Disks. I. Formation Mech-

anism. , 859:118, June 2018. doi: 10.3847/1538-4357/aabf8c.

J. Bae, L. Hartmann, and Z. Zhu. Are Protoplanetary Disks Born with Vortices? Rossby Wave Instability Driven by Protostellar Infall. , 805:15, May 2015. doi: 10.1088/0004-637X/805/1/15.

J. Bae, Z. Zhu, and L. Hartmann. Planetary Signatures in the SAO 206462 (HD 135344B) Disk: A Spiral Arm Passing through Vortex? , 819:134, March 2016. doi: 10.3847/0004-637X/819/2/134.

J. Bae, Z. Zhu, and L. Hartmann. On the Formation of Multiple Concentric Rings and Gaps in Protoplanetary Disks. , 850:201, December 2017. doi: 10.3847/1538-4357/aa9705.

P. Barge and J. Sommeria. Did planet formation begin inside persistent gaseous vortices? , 295:L1–L4, March 1995.

C. Baruteau. *Toward predictive scenarios of planetary migration*. PhD thesis, CEA Saclay, Service d'Astrophysique, 91191 Gif/Yvette Cedex, France, 2008.

C. Baruteau and F. Masset. On the Corotation Torque in a Radiatively Inefficient Disk. , 672:1054-1067, January 2008a. doi: 10.1086/523667.

C. Baruteau and F. Masset. Type I Planetary Migration in a Self-Gravitating Disk. , 678:483-497, May 2008b. doi: 10.1086/529487.

C. Baruteau and Z. Zhu. Gas and dust hydrodynamical simulations of massive lopsided transition discs - II. Dust concentration. , 458:3927–3941, June 2016. doi: 10.1093/mnras/stv2527.

C. Baruteau, A. Crida, S.-J. Paardekooper, F. Masset, J. Guilet, B. Bitsch, R. Nelson, W. Kley, and J. Papaloizou. Planet-Disk Interactions and Early Evolution of Planetary Systems. *Protostars and Planets VI*, pages 667–689, 2014. doi: 10.2458/azu_uapress_9780816531240-ch029.

M. Benisty, A. Juhasz, A. Boccaletti, H. Avenhaus, J. Milli, C. Thalmann, C. Dominik, P. Pinilla, E. Buenzli, A. Pohl, J.-L. Beuzit, T. Birnstiel, J. de Boer, M. Bonnefoy, G. Chauvin, V. Christiaens, A. Garufi, C. Grady, T. Henning, N. Huelamo, A. Isella, M. Langlois, F. Ménard, D. Mouillet, J. Olofsson, E. Pantin, C. Pinte, and L. Pueyo. Asymmetric features in the protoplanetary disk MWC 758. , 578:L6, June 2015. doi: 10.1051/0004-6361/201526011.

M. Benisty, T. Stolker, A. Pohl, J. de Boer, G. Lesur, C. Dominik, C. P. Dullemond, M. Langlois, M. Min, K. Wagner, T. Henning, A. Juhasz, P. Pinilla, S. Facchini, D. Apai, R. van Boekel, A. Garufi, C. Ginski, F. Ménard, C. Pinte, S. P. Quanz, A. Zurlo, A. Boccaletti, M. Bonnefoy, J. L. Beuzit, G. Chauvin, M. Cudel, S. Desidera, M. Feldt, C. Fontanive, R. Gratton, M. Kasper, A.-M. Lagrange, H. LeCoroller, D. Mouillet, D. Mesa, E. Sissa, A. Vigan, J. Antichi, T. Buey, T. Fusco, D. Gisler, M. Llored, Y. Magnard, O. Moeller-Nilsson, J. Pragt, R. Roelfsema, J.-F. Sauvage, and F. Wildi. Shadows and spirals in the protoplanetary disk HD 100453. , 597:A42, January 2017. doi:

10.1051/0004-6361/201629798.

J. Blum and G. Wurm. The Growth Mechanisms of Macroscopic Bodies in Protoplanetary Disks. , 46:21–56, September 2008. doi: 10.1146/annurev.astro.46.060407.145152.

Y. Boehler, L. Ricci, E. Weaver, A. Isella, M. Benisty, J. Carpenter, C. Grady, B.-T. Shen, Y.-W. Tang, and L. Perez. The complex morphology of the young disk MWC 758: Spirals and dust clumps around a large cavity. *ArXiv e-prints*, December 2017.

C. F. Bohren and D. R. Huffman. *Absorption and scattering of light by small particles*. 1983.

A. P. Boss. Giant planet formation by gravitational instability. *Science*, 276:1836–1839, 1997. doi: 10.1126/science.276.5320.1836.

F. Brauer, C. P. Dullemond, and T. Henning. Coagulation, fragmentation and radial motion of solid particles in protoplanetary disks. , 480:859–877, March 2008. doi: 10.1051/0004-6361:20077759.

J. M. Brown, G. A. Blake, C. Qi, C. P. Dullemond, and D. J. Wilner. LkHα 330: Evidence for Dust Clearing through Resolved Submillimeter Imaging. , 675, March 2008. doi: 10.1086/533464.

S. Casassus, C. M. Wright, S. Marino, S. T. Maddison, A. Wootten, P. Roman, S. Pérez, P. Pinilla, M. Wyatt, V. Moral, F. Ménard, V. Christiaens, L. Cieza, and G. van der Plas. A Compact Concentration of Large Grains in the HD 142527 Protoplanetary Dust Trap. , 812:126, October 2015. doi: 10.1088/0004-637X/812/2/126.

S. Casassus, S. Marino, W. Lyra, M. Vidal, A. Wootten, C. Baruteau, S. Perez, F. Alarcon, M. Barraza, M. Carcamo, R. Dong, Z. Zhu, L. Ricci, V. Christiaens, and L. Cieza. Cm-wavelength observations of MWC758: resolved dust trapping in a vortex and intra-cavity signal. *ArXiv e-prints*, May 2018.

Simon Casassus, Gerrit van der Plas, Sebastian Perez M, William R. F. Dent, Ed Fomalont, Janis Hagelberg, Antonio Hales, Andrés Jordán, Dimitri Mawet, Francois Ménard, Al Wootten, David Wilner, A. Meredith Hughes, Matthias R. Schreiber, Julien H. Girard, Barbara Ercolano, Hector Canovas, Pablo E. Román, and Vachail Salinas. Flows of gas through a protoplanetary gap. , 493:191–194, January 2013. doi: 10.1038/nature11769.

S. Charnoz, L. Fouchet, J. Aleon, and M. Moreira. Three-dimensional Lagrangian Turbulent Diffusion of Dust Grains in a Protoplanetary Disk: Method and First Applications. , 737: 33, August 2011. doi: 10.1088/0004-637X/737/1/33.

A. Crida, A. Morbidelli, and F. Masset. On the width and shape of gaps in protoplanetary disks. *Icarus*, 181:587–604, April 2006. doi: 10.1016/j.icarus.2005.10.007.

P. S. de Laplace. *Exposition du système du monde*. 1796. doi: 10.3931/e-rara-497.

R. Dong. Spiral arms in scattered light images of protoplanetary disks. In *AAS/Division for Extreme Solar Systems Abstracts*, volume 3 of *AAS/Division for Extreme Solar Systems*

Abstracts, page 300.01, December 2015a.

R. Dong. Spiral arms in scattered light images of protoplanetary disks. In *AAS/Division for Extreme Solar Systems Abstracts*, volume 3 of *AAS/Division for Extreme Solar Systems Abstracts*, page 300.01, December 2015b.

R. Dong and J. Fung. How Bright are Planet-induced Spiral Arms in Scattered Light? , 835: 38, January 2017. doi: 10.3847/1538-4357/835/1/38.

R. Dong, Z. Zhu, R. R. Rafikov, and J. M. Stone. Observational Signatures of Planets in Protoplanetary Disks: Spiral Arms Observed in Scattered Light Imaging Can be Induced by Planets. , 809:L5, August 2015. doi: 10.1088/2041-8205/809/1/L5.

R. Dong, Z. Zhu, J. Fung, R. Rafikov, E. Chiang, and K. Wagner. An M Dwarf Companion and Its Induced Spiral Arms in the HD 100453 Protoplanetary Disk. , 816:L12, January 2016. doi: 10.3847/2041-8205/816/1/L12.

R. Dong, S.-y. Liu, J. Eisner, S. Andrews, J. Fung, Z. Zhu, E. Chiang, J. Hashimoto, H. B. Liu, S. Casassus, T. Esposito, Y. Hasegawa, T. Muto, Y. Pavlyuchenkov, D. Wilner, E. Akiyama, M. Tamura, and J. Wisniewski. The Eccentric Cavity, Triple Rings, Two-Armed Spirals, and Double Clumps of the MWC 758 Disk. *ArXiv e-prints*, May 2018.

B. T. Draine and H. M. Lee. Optical properties of interstellar graphite and silicate grains. , 285:89–108, October 1984. doi: 10.1086/162480.

C. Dullemond, A. Juhasz, A. Pohl, F. Sereshti, T. Shetty, R.and Peters, B. Commercon, and M. Flock, 2015.

C. P. Dullemond, D. Hollenbach, I. Kamp, and P. D'Alessio. Models of the Structure and Evolution of Protoplanetary Disks. *Protostars and Planets V*, pages 555–572, 2007.

A. C. Dunhill, R. D. Alexander, and P. J. Armitage. A limit on eccentricity growth from global 3D simulations of disc-planet interactions. , 428:3072–3082, February 2013. doi: 10.1093/mnras/sts254.

C. Espaillat, J. Muzerolle, J. Najita, S. Andrews, Z. Zhu, N. Calvet, S. Kraus, J. Hashimoto, A. Kraus, and P. D'Alessio. An Observational Perspective of Transitional Disks. *Protostars and Planets VI*, pages 497–520, 2014. doi: 10.2458/azu_uapress_9780816531240-ch022.

J. Faure, S. Fromang, H. Latter, and H. Meheut. Vortex cycles at the inner edges of dead zones in protoplanetary disks. , 573:A132, January 2015. doi: 10.1051/0004-6361/201424162.

M. Flock, J. P. Ruge, N. Dzyurkevich, Th. Henning, H. Klahr, and S. Wolf. Gaps, rings, and non-axisymmetric structures in protoplanetary disks. From simulations to ALMA observations. , 574, February 2015. doi: 10.1051/0004-6361/201424693.

K. B. Follette, J. Rameau, R. Dong, L. Pueyo, L. M. Close, G. Duchêne, J. Fung, C. Leonard, B. Macintosh, J. R. Males, C. Marois, M. A. Millar-Blanchaer, K. M. Morzinski, W. Mullen, M. Perrin, E. Spiro, J. Wang, S. M. Ammons, V. P. Bailey, T. Barman, J. Bulger,

J. Chilcote, T. Cotten, R. J. De Rosa, R. Doyon, M. P. Fitzgerald, S. J. Goodsell, J. R. Graham, A. Z. Greenbaum, P. Hibon, L.-W. Hung, P. Ingraham, P. Kalas, Q. Konopacky, J. E. Larkin, J. Maire, F. Marchis, S. Metchev, E. L. Nielsen, R. Oppenheimer, D. Palmer, J. Patience, L. Poyneer, A. Rajan, F. T. Rantakyrö, D. Savransky, A. C. Schneider, A. Sivaramakrishnan, I. Song, R. Soummer, S. Thomas, D. Vega, J. K. Wallace, K. Ward-Duong, S. Wiktorowicz, and S. Wolff. Complex Spiral Structure in the HD 100546 Transitional Disk as Revealed by GPI and MagAO. , 153:264, June 2017. doi: 10.3847/1538-3881/aa6d85.

S. Fromang and R. P. Nelson. Global MHD simulations of stratified and turbulent protoplanetary discs. II. Dust settling. , 496:597–608, March 2009. doi: 10.1051/0004-6361/200811220.

W. Fu, H. Li, S. Lubow, and S. Li. Long-term Evolution of Planet-induced Vortices in Protoplanetary Disks. , 788:L41, June 2014a. doi: 10.1088/2041-8205/788/2/L41.

W. Fu, H. Li, S. Lubow, S. Li, and E. Liang. Effects of Dust Feedback on Vortices in Protoplanetary Disks. , 795:L39, November 2014b. doi: 10.1088/2041-8205/795/2/L39.

A. Fuente, C. Baruteau, R. Neri, A. Carmona, M. Agúndez, J. R. Goicoechea, R. Bachiller, J. Cernicharo, and O. Berné. Probing the Cold Dust Emission in the AB Aur Disk: A Dust Trap in a Decaying Vortex? , 846:L3, September 2017. doi: 10.3847/2041-8213/aa8558.

Misato Fukagawa, Takashi Tsukagoshi, Munetake Momose, Kazuya Saigo, Nagayoshi Ohashi, Yoshimi Kitamura, Shu-ichiro Inutsuka, Takayuki Muto, Hideko Nomura, Taku Takeuchi, Hiroshi Kobayashi, Tomoyuki Hanawa, Eiji Akiyama, Mitsuhiko Honda, Hideaki Fujiwara, Akimasa Kataoka, Sanemichi Z. Takahashi, and Hiroshi Shibai. Local Enhancement of the Surface Density in the Protoplanetary Ring Surrounding HD 142527. *Publications of the Astronomical Society of Japan*, 65, December 2013. doi: 10.1093/pasj/65.6.L14.

J. Fung and R. Dong. Inferring Planet Mass from Spiral Structures in Protoplanetary Disks. , 815:L21, December 2015. doi: 10.1088/2041-8205/815/2/L21.

Gaia Collaboration. VizieR Online Data Catalog: Gaia DR2 (Gaia Collaboration, 2018). *VizieR Online Data Catalog*, art. I/345, April 2018.

Gaia Collaboration, A. G. A. Brown, A. Vallenari, T. Prusti, J. H. J. de Bruijne, F. Mignard, R. Drimmel, C. Babusiaux, C. A. L. Bailer-Jones, U. Bastian, and et al. Gaia Data Release 1. Summary of the astrometric, photometric, and survey properties. , 595:A2, November 2016. doi: 10.1051/0004-6361/201629512.

Gaia Collaboration, A. G. A. Brown, A. Vallenari, T. Prusti, J. H. J. de Bruijne, C. Babusiaux, and C. A. L. Bailer-Jones. Gaia Data Release 2. Summary of the contents and survey properties. *ArXiv e-prints*, April 2018a.

Gaia Collaboration, A. G. A. Brown, A. Vallenari, T. Prusti, J. H. J. de Bruijne, C. Babusiaux, and C. A. L. Bailer-Jones. Gaia Data Release 2. Summary of the contents and survey properties. *ArXiv e-prints*, April 2018b.

A. Garufi, S. P. Quanz, H. Avenhaus, E. Buenzli, C. Dominik, F. Meru, M. R. Meyer,

P. Pinilla, H. M. Schmid, and S. Wolf. Small vs. large dust grains in transitional disks: do different cavity sizes indicate a planet?. SAO 206462 (HD 135344B) in polarized light with VLT/NACO. , 560:A105, December 2013. doi: 10.1051/0004-6361/201322429.

C. A. Grady, T. Muto, J. Hashimoto, M. Fukagawa, T. Currie, B. Biller, C. Thalmann, M. L. Sitko, R. Russell, J. Wisniewski, R. Dong, J. Kwon, S. Sai, J. Hornbeck, G. Schneider, D. Hines, A. Moro Martín, M. Feldt, T. Henning, J.-U. Pott, M. Bonnefoy, J. Bouwman, S. Lacour, A. Mueller, A. Juhász, A. Crida, G. Chauvin, S. Andrews, D. Wilner, A. Kraus, S. Dahm, T. Robitaille, H. Jang-Condell, L. Abe, E. Akiyama, W. Brandner, T. Brandt, J. Carson, S. Egner, K. B. Follette, M. Goto, O. Guyon, Y. Hayano, M. Hayashi, S. Hayashi, K. Hodapp, M. Ishii, M. Iye, M. Janson, R. Kandori, G. Knapp, T. Kudo, N. Kusakabe, M. Kuzuhara, S. Mayama, M. McElwain, T. Matsuo, S. Miyama, J.-I. Morino, T. Nishimura, T.-S. Pyo, G. Serabyn, H. Suto, R. Suzuki, M. Takami, N. Takato, H. Terada, D. Tomono, E. Turner, M. Watanabe, T. Yamada, H. Takami, T. Usuda, and M. Tamura. Spiral Arms in the Asymmetrically Illuminated Disk of MWC 758 and Constraints on Giant Planets. , 762:48, January 2013. doi: 10.1088/0004-637X/762/1/48.

M. Hammer, K. M. Kratter, and M.-K. Lin. Slowly-growing gap-opening planets trigger weaker vortices. , 466:3533–3543, April 2017. doi: 10.1093/mnras/stw3000.

J. Hashimoto, T. Tsukagoshi, J. M. Brown, R. Dong, T. Muto, Z. Zhu, J. Wisniewski, N. Ohashi, T. kudo, N. Kusakabe, L. Abe, E. Akiyama, W. Brandner, T. Brandt, J. Carson, T. Currie, S. Egner, M. Feldt, C. A. Grady, O. Guyon, Y. Hayano, M. Hayashi, S. Hayashi, T. Henning, K. Hodapp, M. Ishii, M. Iye, M. Janson, R. Kandori, G. Knapp, M. Kuzuhara, J. Kwon, T. Matsuo, M. W. McElwain, S. Mayama, K. Mede, S. Miyama, J. I. Morino, A. Moro-Martin, T. Nishimura, T. S. Pyo, G. Serabyn, T. Suenaga, H. Suto, R. Suzuki, Y. Takahashi, M. Takami, N. Takato, H. Terada, C. Thalmann, D. Tomono, E. L. Turner, M. Watanabe, T. Yamada, H. Takami, T. Usuda, and M. Tamura. The Structure of Pre-transitional Protoplanetary Disks. II. Azimuthal Asymmetries, Different Radial Distributions of Large and Small Dust Grains in PDS 70. , 799, January 2015. doi: 10.1088/0004-637X/799/1/43.

L. G. Henyey and J. L. Greenstein. Diffuse radiation in the Galaxy. , 93:70–83, January 1941. doi: 10.1086/144246.

N. Huélamo, G. Chauvin, H. M. Schmid, S. P. Quanz, E. Whelan, J. Lillo-Box, D. Barrado, B. Montesinos, J. M. Alcalá, M. Benisty, I. de Gregorio-Monsalvo, I. Mendigutía, H. Bouy, B. Merín, J. de Boer, A. Garufi, and E. Pantin. Searching for H_α emitting sources around MWC 758. SPHERE/ZIMPOL high-contrast imaging. , 613:L5, May 2018. doi: 10.1051/0004-6361/201832874.

S. Inaba and P. Barge. Dusty Vortices in Protoplanetary Disks. , 649:415–427, September 2006. doi: 10.1086/506427.

Andrea Isella, Antonella Natta, David Wilner, John M. Carpenter, and Leonardo Testi. Millimeter Imaging of MWC 758: Probing the Disk Structure and Kinematics. , 725:1735–1741, December 2010. doi: 10.1088/0004-637X/725/2/1735.

Andrea Isella, Laura M. Pérez, John M. Carpenter, Luca Ricci, Sean Andrews, and Katherine Rosenfeld. An Azimuthal Asymmetry in the LkHα 330 Disk. , 775, September 2013. doi: 10.1088/0004-637X/775/1/30.

A. Johansen and H. Klahr. Dust Diffusion in Protoplanetary Disks by Magnetorotational Turbulence. , 634:1353–1371, December 2005. doi: 10.1086/497118.

A. Johansen and P. Lacerda. Prograde rotation of protoplanets by accretion of pebbles in a gaseous environment. , 404:475–485, May 2010. doi: 10.1111/j.1365-2966.2010.16309.x.

A. Johansen, J. S. Oishi, M.-M. Mac Low, H. Klahr, T. Henning, and A. Youdin. Rapid planetesimal formation in turbulent circumstellar disks. , 448:1022–1025, August 2007. doi: 10.1038/nature06086.

A. Juhász, M. Benisty, A. Pohl, C. P. Dullemond, C. Dominik, and S.-J. Paardekooper. Spiral arms in scattered light images of protoplanetary discs: are they the signposts of planets? , 451:1147–1157, August 2015. doi: 10.1093/mnras/stv1045.

I. Kant. *Allgemeine Naturgeschichte und Theorie des Himmels*. 1755.

Akimasa Kataoka, Hidekazu Tanaka, Satoshi Okuzumi, and Koji Wada. Fluffy dust forms icy planetesimals by static compression. , 557:L4, September 2013. doi: 10.1051/0004-6361/201322151.

Akimasa Kataoka, Satoshi Okuzumi, Hidekazu Tanaka, and Hideko Nomura. Opacity of fluffy dust aggregates. , 568:A42, August 2014. doi: 10.1051/0004-6361/201323199.

M. Keppler, M. Benisty, A. Müller, T. Henning, R. van Boekel, F. Cantalloube, C. Ginski, R. G. van Holstein, A.-L. Maire, A. Pohl, M. Samland, H. Avenhaus, J.-L. Baudino, A. Boccaletti, J. de Boer, M. Bonnefoy, G. Chauvin, S. Desidera, M. Langlois, C. Lazzoni, G. Marleau, C. Mordasini, N. Pawellek, T. Stolker, A. Vigan, A. Zurlo, T. Birnstiel, W. Brandner, M. Feldt, M. Flock, J. Girard, R. Gratton, J. Hagelberg, A. Isella, M. Janson, A. Juhasz, J. Kemmer, Q. Kral, A.-M. Lagrange, R. Launhardt, A. Matter, F. Ménard, J. Milli, P. Mollière, J. Olofsson, L. Perez, P. Pinilla, C. Pinte, S. P. Quanz, T. Schmidt, S. Udry, Z. Wahhaj, J. P. Williams, E. Buenzli, M. Cudel, C. Dominik, R. Galicher, M. Kasper, J. Lannier, D. Mesa, D. Mouillet, S. Peretti, C. Perrot, G. Salter, E. Sissa, F. Wildi, L. Abe, J. Antichi, J.-C. Augereau, A. Baruffolo, P. Baudoz, A. Bazzon, J.-L. Beuzit, P. Blanchard, S. S. Brems, T. Buey, V. De Caprio, M. Carbillet, M. Carle, E. Cascone, A. Cheetham, R. Claudi, A. Costille, A. Delboulbé, K. Dohlen, D. Fantinel, P. Feautrier, T. Fusco, E. Giro, D. Gisler, L. Gluck, C. Gry, N. Hubin, E. Hugot, M. Jaquet, D. Le Mignant, M. Llored, F. Madec, Y. Magnard, P. Martinez, D. Maurel, M. Meyer, O. Moeller-Nilsson, T. Moulin, L. Mugnier, A. Origne, A. Pavlov, D. Perret, C. Petit, J. Pragt, P. Puget, P. Rabou, J. Ramos, F. Rigal, S. Rochat, R. Roelfsema, G. Rousset, A. Roux, B. Salasnich, J.-F. Sauvage, A. Sevin, C. Soenke, E. Stadler, M. Suarez, M. Turatto, and L. Weber. Discovery of a planetary-mass companion within the gap of the transition disk around PDS 70. *ArXiv e-prints*, June 2018.

H. Klahr and P. Bodenheimer. Formation of Giant Planets by Concurrent Accretion of Solids

and Gas inside an Anticyclonic Vortex. , 639:432–440, March 2006. doi: 10.1086/498928.

H. H. Klahr and P. Bodenheimer. Turbulence in Accretion Disks: Vorticity Generation and Angular Momentum Transport via the Global Baroclinic Instability. , 582:869–892, January 2003. doi: 10.1086/344743.

H. Hubertus Klahr and Thomas Henning. Particle-Trapping Eddies in Protoplanetary Accretion Disks. , 128:213–229, July 1997. doi: 10.1006/icar.1997.5720.

W. Kley and G. Dirksen. Disk eccentricity and embedded planets. , 447:369–377, February 2006. doi: 10.1051/0004-6361:20053914.

W. Kley and R. P. Nelson. Planet-Disk Interaction and Orbital Evolution. , 50:211–249, September 2012. doi: 10.1146/annurev-astro-081811-125523.

Stefan Kraus, Alexander Kreplin, Misato Fukugawa, Takayuki Muto, Michael L. Sitko, Alison K. Young, Matthew R. Bate, Carol Grady, Tim T. Harries, John D. Monnier, Matthew Willson, and John Wisniewski. Dust-trapping vortices and a potentially planet-triggered spiral wake in the pre-transitional disk of v1247 orionis. *The Astrophysical Journal Letters*, 848(1):L11, 2017. URL `http://stacks.iop.org/2041-8205/848/i=1/a=L11`.

M. Lambrechts and A. Johansen. Rapid growth of gas-giant cores by pebble accretion. , 544: A32, August 2012. doi: 10.1051/0004-6361/201219127.

R. Les and M.-K. Lin. Gap formation and stability in non-isothermal protoplanetary discs. , 450:1503–1513, June 2015. doi: 10.1093/mnras/stv712.

A. Li and J. M. Greenberg. A unified model of interstellar dust. , 323:566–584, July 1997.

H. Li, J. M. Finn, R. V. E. Lovelace, and S. A. Colgate. Rossby Wave Instability of Thin Accretion Disks. II. Detailed Linear Theory. , 533:1023–1034, April 2000. doi: 10.1086/308693.

H. Li, S. A. Colgate, B. Wendroff, and R. Liska. Rossby Wave Instability of Thin Accretion Disks. III. Nonlinear Simulations. , 551:874–896, April 2001. doi: 10.1086/320241.

H. Li, S. Li, J. Koller, B. B. Wendroff, R. Liska, C. M. Orban, E. P. T. Liang, and D. N. C. Lin. Potential Vorticity Evolution of a Protoplanetary Disk with an Embedded Protoplanet. , 624:1003–1009, May 2005. doi: 10.1086/429367.

M.-K. Lin. Rossby Wave Instability in Locally Isothermal and Polytropic Disks: Three-dimensional Linear Calculations. , 754:21, July 2012. doi: 10.1088/0004-637X/754/1/21.

M.-K. Lin and J. C. B. Papaloizou. The effect of self-gravity on vortex instabilities in disc-planet interactions. , 415:1426–1444, August 2011. doi: 10.1111/j.1365-2966.2011.18798.x.

R. V. E. Lovelace and R. G. Hohlfeld. Rossby wave instability with self-gravity. , 429: 529–533, February 2013. doi: 10.1093/mnras/sts361.

R. V. E. Lovelace, H. Li, S. A. Colgate, and A. F. Nelson. Rossby Wave Instability of Keplerian Accretion Disks. , 513:805–810, March 1999. doi: 10.1086/306900.

W. Lyra. Convective Overstability in Accretion Disks: Three-dimensional Linear Analysis and Nonlinear Saturation. , 789:77, July 2014. doi: 10.1088/0004-637X/789/1/77.

W. Lyra and H. Klahr. The baroclinic instability in the context of layered accretion. Self-sustained vortices and their magnetic stability in local compressible unstratified models of protoplanetary disks. , 527:A138, March 2011. doi: 10.1051/0004-6361/201015568.

W. Lyra and M.-K. Lin. Steady State Dust Distributions in Disk Vortices: Observational Predictions and Applications to Transitional Disks. , 775:17, September 2013. doi: 10.1088/0004-637X/775/1/17.

W. Lyra, A. Johansen, H. Klahr, and N. Piskunov. Standing on the shoulders of giants. Trojan Earths and vortex trapping in low mass self-gravitating protoplanetary disks of gas and solids. , 493:1125–1139, January 2009a. doi: 10.1051/0004-6361:200810797.

W. Lyra, A. Johansen, A. Zsom, H. Klahr, and N. Piskunov. Planet formation bursts at the borders of the dead zone in 2D numerical simulations of circumstellar disks. , 497:869–888, April 2009b. doi: 10.1051/0004-6361/200811265.

W. Lyra, N. J. Turner, and C. P. McNally. Rossby wave instability does not require sharp resistivity gradients. , 574:A10, February 2015. doi: 10.1051/0004-6361/201424919.

S. Marino, S. Casassus, S. Perez, W. Lyra, P. E. Roman, H. Avenhaus, C. M. Wright, and S. T. Maddison. Compact Dust Concentration in the MWC 758 Protoplanetary Disk. , 813:76, November 2015. doi: 10.1088/0004-637X/813/1/76.

F. Masset. FARGO: A fast eulerian transport algorithm for differentially rotating disks. , 141:165–173, January 2000. doi: 10.1051/aas:2000116.

G. Meeus, B. Montesinos, I. Mendigutía, I. Kamp, W. F. Thi, C. Eiroa, C. A. Grady, G. Mathews, G. Sandell, C. Martin-Zaïdi, S. Brittain, W. R. F. Dent, C. Howard, F. Ménard, C. Pinte, A. Roberge, B. Vandenbussche, and J. P. Williams. Observations of Herbig Ae/Be stars with Herschel/PACS. The atomic and molecular contents of their protoplanetary discs. , 544:A78, August 2012. doi: 10.1051/0004-6361/201219225.

H. Meheut, F. Casse, P. Varniere, and M. Tagger. Rossby wave instability and three-dimensional vortices in accretion disks. , 516, June 2010. doi: 10.1051/0004-6361/201014000.

H. Meheut, R. Keppens, F. Casse, and W. Benz. Formation and long-term evolution of 3D vortices in protoplanetary discs. , 542, June 2012a. doi: 10.1051/0004-6361/201118500.

H. Meheut, Z. Meliani, P. Varniere, and W. Benz. Dust-trapping Rossby vortices in protoplanetary disks. , 545, September 2012b. doi: 10.1051/0004-6361/201219794.

H. Meheut, R. V. E. Lovelace, and D. Lai. How strong are the Rossby vortices? , 430:

1988–1993, April 2013. doi: 10.1093/mnras/stt022.

Heloise Meheut, Cong Yu, and Dong Lai. Rossby wave instability in 3D discs. , 422:2399–2406, May 2012c. doi: 10.1111/j.1365-2966.2012.20789.x.

M. Montesinos and N. Cuello. Planetary-like spirals caused by moving shadows in transition discs. , 475:L35–L39, March 2018. doi: 10.1093/mnrasl/sly001.

M. Montesinos, S. Perez, S. Casassus, S. Marino, J. Cuadra, and V. Christiaens. Spiral Waves Triggered by Shadows in Transition Disks. , 823:L8, May 2016. doi: 10.3847/2041-8205/823/1/L8.

A. Morbidelli and D. Nesvorny. Dynamics of pebbles in the vicinity of a growing planetary embryo: hydro-dynamical simulations. , 546:A18, October 2012. doi: 10.1051/0004-6361/201219824.

Y. Ohta, M. Fukagawa, M. L. Sitko, T. Muto, S. Kraus, C. A. Grady, J. P. Wisniewski, J. R. Swearingen, H. Shibai, T. Sumi, J. Hashimoto, T. Kudo, N. Kusakabe, M. Momose, Y. Okamoto, T. Kotani, M. Takami, T. Currie, C. Thalmann, M. Janson, E. Akiyama, K. B. Follette, S. Mayama, L. Abe, W. Brandner, T. D. Brandt, J. C. Carson, S. E. Egner, M. Feldt, M. Goto, O. Guyon, Y. Hayano, M. Hayashi, S. S. Hayashi, T. Henning, K. W. Hodapp, M. Ishii, M. Iye, R. Kandori, G. R. Knapp, M. Kuzuhara, J. Kwon, T. Matsuo, M. W. McElwain, S. Miyama, J.-I. Morino, A. Moro-Martín, T. Nishimura, T.-S. Pyo, E. Serabyn, T. Suenaga, H. Suto, R. Suzuki, Y. H. Takahashi, H. Takami, N. Takato, H. Terada, D. Tomono, E. L. Turner, T. Usuda, M. Watanabe, T. Yamada, and M. Tamura. Extreme asymmetry in the polarized disk of V1247 Orionis*. , 68:53, August 2016. doi: 10.1093/pasj/psw051.

C. W. Ormel and H. H. Klahr. The effect of gas drag on the growth of protoplanets. Analytical expressions for the accretion of small bodies in laminar disks. , 520:A43, September 2010. doi: 10.1051/0004-6361/201014903.

I. Pascucci and S. Tachibana. *The Clearing of Protoplanetary Disks and of the Protosolar Nebula*, pages 263–298. February 2010.

L. M. Pérez, A. Isella, J. M. Carpenter, and C. J. Chandler. Large-scale Asymmetries in the Transitional Disks of SAO 206462 and SR 21. , 783:L13, March 2014. doi: 10.1088/2041-8205/783/1/L13.

S. Perez, A. Dunhill, S. Casassus, P. Roman, J. Szulágyi, C. Flores, S. Marino, and M. Montesinos. Planet Formation Signposts: Observability of Circumplanetary Disks via Gas Kinematics. , 811:L5, September 2015. doi: 10.1088/2041-8205/811/1/L5.

S. Pérez, S. Casassus, and P. Benítez-Llambay. Observability of planet-disc interactions in CO kinematics. , 480:L12–L17, October 2018. doi: 10.1093/mnrasl/sly109.

P. Pinilla, M. Benisty, and T. Birnstiel. Ring shaped dust accumulation in transition disks. , 545:A81, September 2012. doi: 10.1051/0004-6361/201219315.

P. Pinilla, M. Tazzari, I. Pascucci, A. N. Youdin, A. Garufi, C. F. Manara, L. Testi, G. van der Plas, S. A. Barenfeld, H. Canovas, E. G. Cox, N. P. Hendler, L. M. Pérez, and N. van der Marel. Homogeneous Analysis of the Dust Morphology of Transition Disks Observed with ALMA: Investigating Dust Trapping and the Origin of the Cavities. , 859:32, May 2018. doi: 10.3847/1538-4357/aabf94.

C. Pinte, D. J. Price, F. Ménard, G. Duchêne, W. R. F. Dent, T. Hill, I. de Gregorio-Monsalvo, A. Hales, and D. Mentiplay. Kinematic Evidence for an Embedded Protoplanet in a Circumstellar Disk. , 860:L13, June 2018. doi: 10.3847/2041-8213/aac6dc.

J. B. Pollack, O. Hubickyj, P. Bodenheimer, J. J. Lissauer, M. Podolak, and Y. Greenzweig. Formation of the Giant Planets by Concurrent Accretion of Solids and Gas. , 124:62–85, November 1996. doi: 10.1006/icar.1996.0190.

S. P. Quanz, H. Avenhaus, E. Buenzli, A. Garufi, H. M. Schmid, and S. Wolf. Gaps in the HD 169142 Protoplanetary Disk Revealed by Polarimetric Imaging: Signs of Ongoing Planet Formation? , 766:L2, March 2013. doi: 10.1088/2041-8205/766/1/L2.

N. Raettig, W. Lyra, and H. Klahr. A Parameter Study for Baroclinic Vortex Amplification. , 765:115, March 2013. doi: 10.1088/0004-637X/765/2/115.

R. R. Rafikov. Can Giant Planets Form by Direct Gravitational Instability? , 621:L69–L72, March 2005. doi: 10.1086/428899.

Z. Regály, A. Juhász, Z. Sándor, and C. P. Dullemond. Possible planet-forming regions on submillimetre images. , 419:1701–1712, January 2012. doi: 10.1111/j.1365-2966.2011.19834.x.

Z. Regály, A. Juhász, and D. Nehéz. Interpreting Brightness Asymmetries in Transition Disks: Vortex at Dead Zone or Planet-carved Gap Edges? , 851:89, December 2017. doi: 10.3847/1538-4357/aa9a3f.

M. Reggiani, V. Christiaens, O. Absil, D. Mawet, E. Huby, E. Choquet, C. A. Gomez Gonzalez, G. Ruane, B. Femenia, E. Serabyn, K. Matthews, M. Barraza, B. Carlomagno, D. Defrère, C. Delacroix, S. Habraken, A. Jolivet, M. Karlsson, G. Orban de Xivry, P. Piron, J. Surdej, E. Vargas Catalan, and O. Wertz. Discovery of a point-like source and a third spiral arm in the transition disk around the Herbig Ae star MWC 758. *ArXiv e-prints*, October 2017.

B. Ren, R. Dong, T. M. Esposito, L. Pueyo, J. H. Debes, C. A. Poteet, É. Choquet, M. Benisty, E. Chiang, C. A. Grady, D. C. Hines, G. Schneider, and R. Soummer. A Decade of MWC 758 Disk Images: Where Are the Spiral-arm-driving Planets? , 857:L9, April 2018. doi: 10.3847/2041-8213/aab7f5.

S. Richard, P. Barge, and S. Le Dizès. Structure, stability, and evolution of 3D Rossby vortices in protoplanetary disks. , 559, November 2013. doi: 10.1051/0004-6361/201322175.

J. P. Ruge, M. Flock, S. Wolf, N. Dzyurkevich, S. Fromang, T. Henning, H. Klahr, and H. Meheut. Gaps, rings, and non-axisymmetric structures in protoplanetary disks: Emis-

sion from large grains. , 590:A17, May 2016. doi: 10.1051/0004-6361/201526616.

Z. Sándor, W. Lyra, and C. P. Dullemond. Formation of Planetary Cores at Type I Migration Traps. , 728:L9, February 2011. doi: 10.1088/2041-8205/728/1/L9.

N. I. Shakura and R. A. Sunyaev. Black holes in binary systems. Observational appearance. , 24:337–355, 1973.

A. Sierra, S. Lizano, and P. Barge. Dust Concentration and Emission in Protoplanetary Disks Vortices. , 850:115, December 2017. doi: 10.3847/1538-4357/aa94c1.

J. B. Simon, G. Lesur, M. W. Kunz, and P. J. Armitage. Magnetically driven accretion in protoplanetary discs. , 454:1117–1131, November 2015. doi: 10.1093/mnras/stv2070.

M. F. Skrutskie, D. Dutkevitch, S. E. Strom, S. Edwards, K. M. Strom, and M. A. Shure. A sensitive 10-micron search for emission arising from circumstellar dust associated with solar-type pre-main-sequence stars. , 99:1187–1195, April 1990. doi: 10.1086/115407.

D. S. Spiegel and A. Burrows. Spectral and Photometric Diagnostics of Giant Planet Formation Scenarios. , 745:174, February 2012. doi: 10.1088/0004-637X/745/2/174.

K. M. Strom, S. E. Strom, S. Edwards, S. Cabrit, and M. F. Skrutskie. Circumstellar material associated with solar-type pre-main-sequence stars - A possible constraint on the timescale for planet building. , 97:1451–1470, May 1989. doi: 10.1086/115085.

J. Szulágyi, A. Morbidelli, A. Crida, and F. Masset. Accretion of Jupiter-mass Planets in the Limit of Vanishing Viscosity. , 782:65, February 2014. doi: 10.1088/0004-637X/782/2/65.

Y. Wen Tang, S. Guilloteau, V. Piétu, A. Dutrey, N. Ohashi, and P. T. P. Ho. The circumstellar disk of AB Aurigae: evidence for envelope accretion at late stages of star formation? , 547, November 2012. doi: 10.1051/0004-6361/201219414.

Richard Teague, Jaehan Bae, Edwin A. Bergin, Tilman Birnstiel, and Daniel Foreman-Mackey. A kinematical detection of two embedded jupiter-mass planets in hd 163296. *The Astrophysical Journal Letters*, 860(1):L12, 2018. URL `http://stacks.iop.org/2041-8205/860/i=1/a=L12`.

L. Testi, T. Birnstiel, L. Ricci, S. Andrews, J. Blum, J. Carpenter, C. Dominik, A. Isella, A. Natta, J. P. Williams, and D. J. Wilner. Dust Evolution in Protoplanetary Disks. *Protostars and Planets VI*, pages 339–361, 2014. doi: 10.2458/azu_uapress_9780816531240-ch015.

E. W. Thommes, M. J. Duncan, and H. F. Levison. Oligarchic growth of giant planets. , 161:431–455, February 2003. doi: 10.1016/S0019-1035(02)00043-X.

A. Toomre. On the gravitational stability of a disk of stars. , 139:1217–1238, May 1964. doi: 10.1086/147861.

M. E. van den Ancker, D. de Winter, and H. R. E. Tjin A Djie. HIPPARCOS photometry

of Herbig Ae/Be stars. , 330:145–154, February 1998.

N. van der Marel, E. F. van Dishoeck, S. Bruderer, T. Birnstiel, P. Pinilla, C. P. Dullemond, T. A. van Kempen, M. Schmalzl, J. M. Brown, G. J. Herczeg, G. S. Mathews, and V. Geers. A Major Asymmetric Dust Trap in a Transition Disk. *Science*, 340:1199–1202, June 2013. doi: 10.1126/science.1236770.

N. van der Marel, P. Cazzoletti, P. Pinilla, and A. Garufi. Vortices and Spirals in the HD135344B Transition Disk. , 832:178, December 2016a. doi: 10.3847/0004-637X/832/2/178.

N. van der Marel, E. F. van Dishoeck, S. Bruderer, S. M. Andrews, K. M. Pontoppidan, G. J. Herczeg, T. van Kempen, and A. Miotello. Resolved gas cavities in transitional disks inferred from CO isotopologs with ALMA. , 585:A58, January 2016b. doi: 10.1051/0004-6361/201526988.

F. van Leeuwen. Validation of the new Hipparcos reduction. , 474:653–664, November 2007. doi: 10.1051/0004-6361:20078357.

P. Varnière and M. Tagger. Reviving Dead Zones in accretion disks by Rossby vortices at their boundaries. , 446:L13–L16, February 2006. doi: 10.1051/0004-6361:200500226.

K. Wagner, D. Apai, M. Kasper, and M. Robberto. Discovery of a Two-armed Spiral Structure in the Gapped Disk around Herbig Ae Star HD 100453. , 813:L2, November 2015. doi: 10.1088/2041-8205/813/1/L2.

S. J. Weidenschilling. Aerodynamics of solid bodies in the solar nebula. , 180:57–70, July 1977. doi: 10.1093/mnras/180.1.57.

F. L. Whipple. On certain aerodynamic processes for asteroids and comets. In A. Elvius, editor, *From Plasma to Planet*, page 211, 1972.

P. R. Woodward. Theoretical models of star formation. , 16:555–584, 1978. doi: 10.1146/annurev.aa.16.090178.003011.

C. M. Wright, S. T. Maddison, D. J. Wilner, M. G. Burton, D. Lommen, E. F. van Dishoeck, P. Pinilla, T. L. Bourke, F. Menard, and C. Walsh. Resolving structure of the disc around HD100546 at 7 mm with ATCA. , 453:414–438, October 2015. doi: 10.1093/mnras/stv1619.

A. N. Youdin and J. Goodman. Streaming Instabilities in Protoplanetary Disks. , 620:459–469, February 2005. doi: 10.1086/426895.

A. N. Youdin and Y. Lithwick. Particle stirring in turbulent gas disks: Including orbital oscillations. , 192:588–604, December 2007. doi: 10.1016/j.icarus.2007.07.012.

A. N. Youdin and F. H. Shu. Planetesimal Formation by Gravitational Instability. , 580:494–505, November 2002. doi: 10.1086/343109.

Z. Zhu and C. Baruteau. Gas and dust hydrodynamical simulations of massive lopsided

transition discs - I. Gas distribution. , 458:3918–3926, June 2016. doi: 10.1093/mnras/stw202.

Z. Zhu, J. M. Stone, R. R. Rafikov, and X.-n. Bai. Particle Concentration at Planet-induced Gap Edges and Vortices. I. Inviscid Three-dimensional Hydro Disks. , 785:122, April 2014. doi: 10.1088/0004-637X/785/2/122.

Z. Zhu, R. Dong, J. M. Stone, and R. R. Rafikov. The Structure of Spiral Shocks Excited by Planetary-mass Companions. , 813:88, November 2015. doi: 10.1088/0004-637X/813/2/88.